BACKSCATTERING INTERFEROMETERY

From Modeling and Fabrication to Application

By

Joey C. Latham

Dissertation

Submitted to the Faculty of the

Graduate School of Vanderbilt University

in partial fulfillment of the requirements

for the degree of

DOCTOR OF PHILOSOPHY

in

Chemistry

May, 2007

Nashville, Tennessee

Dr. Darryl J. Bornhop

Dr. Sandra J. Rosenthal

Dr. Brian O. Bachmann

Dr. Hassane Mchaourab

Dr. John P. Wikswo

To my Mom:

Thank you for your guidance, encouragement and love. Thanks for instilling in me the thirst for knowledge while also teaching me the lessons no book could contain. You truly are the greatest woman I will ever know.

To Elizabeth and Evan:

You two are the reasons that I am here and this has been accomplished. One day I hope both of you can read this document, understand it, and improve upon it if you wish. You both have unlimited potential, so reach for the stars.
I love you.

ACKNOWLEDGMENTS

First let me acknowledge the source of funding that made this research possible, the National Eye Institute (NEI). For three years I was a trainee on a grant from the NEI through by Dr. Hassane Mchaourab. I met Hassane my second semester here at Vanderbilt and was able to gain a wealth of knowledge on subjects I knew very little about, further expanding my foundation in science. Unfortunately, I think the most Hassane got out of it was a babysitter. I would also like to personally thank all the members on my committee: Dr. Brian Bachmann, Dr. Sandra Roenthal, Dr. John Wikswo, and my chairman Dr. Darryl Bornhop for their patience, guidance, and breadth of knowledge. It was never easy, but then again nothing ever is easy. Much of this work was made possible thanks to the use of facilities granted to me by Risø National Laboratory in Roskilde, Denmark and the Vanderbilt Institute for Integrative Biosystems Research and Education (VIIBRE). I want to also acknowledge my mentors while in Denmark Dr. Neils B. Larsen and Dr. Peter Andersen. Not only are both men extremely intelligent, but both were very hospitable to this foreigner from the States and always made me welcome to come back.

I am grateful to all of my current and former group members without whom this would not have been as much fun. There are a few in particular I would especially like to thank. Let me start with Tim Goebel, aka analspelunker or the man from Djibouti. The worst thing about leaving Texas Tech was the fact Tim stayed behind. Not only did our group miss his wit and intelligence, but Dima and I missed a good friend. Speaking of Dima, aka shooting baby, the white Russian spouts facts like his homeland does vodka. Dima can answer almost any question you pose, and he is right probably half of the time ☺! But all joking aside, Dima is very knowledgable in just about everything. Throughout the six years I have known him I have learned so much, but more important than that, I gained a tremendous friend. Lastly, I want to say thanks to Henrik, the inventor of Viking sausage. Henrik and I lived together for the better part of 2 years either here in the States or over in Denmark. While in Denmark, he and his family made my stay so enjoyable, made me feel so at home, and really gave me one of the best experiences of my life. Just like Tim and Dima, Henrik is an extremely intelligent person while at the same time being really down

to earth and capable of enjoying life. Henrik has always been such a great friend to me even at times when I probably didn't deserve it, but then again that is what real friends do. I do hope will always stay in touch Henrik and anytime you are in the States again know that you are always welcome where ever I am. (Go Brøndby!)

I also want to acknowledge friends and family who have helped me along this long and winding road. To the guys at Doc's, I miss you everyday. Pate, Marcus, and Willis…. I miss the fun, the golf, and the drinks we all shared. I think personally I would have always been content living in Lubbock. It wasn't the job was that great or that Lubbock is in a great location, it was just because of you guys. But deep down I knew I needed to try and get something more for my kids. I'm just sorry this research wasn't focused on a cure for baldness Pate ☺ I can't wait to come and see you guys again. Now that this is over hopefully I can come this summer.

As for family, I could not have asked for a better set of loud, dysfunctional, and entertaining members because above all my family has always been there for me, has always been affectionate, and has always loved. My family is too large to list individually, to do so might double the size of this document. But I definitely want to thank my sister for always being honest and letting me know I was not as great as everyone else thought I was. She always kept me grounded while at the same time always trying to protect. Meredith, you will always be my big sis….my sissy and I will always love you. And to all my family members, I love you, I miss you, and I miss the good times we always have together.

Like the dedication mentioned I would not be writing this document if not for my mom and my two kids. My mom always put my education first. I remember her getting Meredith and myself an encyclopedia set, books on Roman history, Greek mythology, and some science and math books. Everytime I asked a question she would tell me to go look it up. And I would, and I would read and read. She instilled in me the thirst for knowledge. My mom has also been my greatest defender, if you don't believe me you can ask my old basketball coach to tell the story about Campti, La. While my mom helped to make me intelligent, my kids drove me to use my intelligence. Elizabeth and Evan mean the world to me and I want to be able to give them anything they could ever want. Just like every parent, I want their lives to be easier than mine,

thus this journey to a Ph.D. I know in the end all the struggles will be worth it. I love you guys. I wished we all lived closer to one another and hopefully someday soon we will. Until then know that all of you are always in my mind and I will always love you.

Lastly, I want to thank Sheerin. Sheerin, you are what makes Vanderbilt feel like home. You are my best friend, my harshest critique, and my greatest love. You have helped me to become a better friend, a better scientist, and an all around better person. I love our time together and I am at ease knowing I will be spending the rest of my life with you. I have truly found peace and my life long companion….. my soulmate. I love you baby!

TABLE OF CONTENTS

Page

DEDICATION iii

ACKNOWLEDGMENTS iv

LIST OF TABLES x

LIST OF FIGURES xi

LIST OF ABBREVIATIONS xv

Chapter

I. INTRODUCTION 1

II. BACKGROUND 8

Nanotechnology and Microfluidics 8
Early Inception 8
Fabrication Methods and Materials 11
Applications and μ-TAS 29
Detection Methodologies Used in Nanotechnology 31
Optical Detection 31
Electrochemical Detection 33
Quartz Crystal Microbalance 34
Refractive Index 36
Backscattering Interferometry 39
Experimental Background and Setup 40
Interference Pattern 40
Early Applications 41
References 45

III. MODELING LIGHT PROPAGATION 53

Simulations with Capillary Flow Systems 53
Ray Tracing Model 53
Wave Based Model 55
Comparison of Simulated Fringe Patterns to Experiments 56
Total Internal Reflection 59
Simulations in Polymeric Materials 60
ASAP Optical Modeling 61

Modeling Different Channel Geometries 62
Fringe Analysis and Sensitivity 65
Summary 68
References 70

IV. MICROFLUIDIC SYSTEMS 71

Planar Fabrication 71
Optical Lithography 71
Soft Lithography 74
Fabrication of Semi-Circular Channels 76
Sacrificial Layers and Mask Opening 76
Silicon Etching 78
Electroplating and Injection Molding 79
Fluidics on the Microscale 81
Background 82
Mixing in Microchips 83
Summary 85
References 87

V. SIGNAL INTERPRETATION AND DATA ANALYSIS 89

Manifestation of the Interference Pattern 89
Interrogation of the Interference Pattern 91
Data Analysis 93
Noise Assessment and Error Analysis 99
Summary 106
References 107

VI. APPLICATIONS 109

Surface Bound Experiments 110
Immobilization Chemistry 110
Experimental Setup 111
Protein A-IgG 113
DNA Hybridization 114
Solution Phase Proof of Concept 115
Background 115
Experimental 116
Analysis and Results 118
Calmodulin Studies 120
Background 120
Experimental 124
Results and Analysis 125
sHSP Interaction in Free Solution 131
Background 131

Site-directed Mutagenesis 138
Expression, Purification, and Labeling 139
BI experimental 140
ITC experimental 141
Detection Method Comparison 141
Distinguishing Binding Affinity 146
α-crystallin and Its Role in Cataract 149
Summary 153
References 155

VII. CONCLUSIONS AND PERSPECTIVES 163

LIST OF TABLES

Table Page

3.1 Positional comparison of minima in the simulated and experimental fringe pattern as a function of backscattered angle (Θ°)..... 58

3.2 Comparison of the observed and predicted angle of total internal reflection..... 60

4.1 Procedure for cleaning the Silicon wafer 77

5.1 Comparison of the sensitivity of different interrogation methods used in BI..... 93

6.1. Comparison of K_D values for Calmodulin interactions 129

6.2. Cross-validation of BI results with more standard detection methods. Also shown is the substantial reduction in material needed for BI experiments..... 146

6.3. Analysis of Thermodynamic Data for Variably Destabilized Mutants of T4L..... 149

6.4. Kinetic parameters obtained by global analysis of BI data with a comparison to SPR data. 153

LIST OF FIGURES

Figure *Page*

1.1 A. Signaling pathways of some noted oncogenes and tumor-suppressor genes relevant to cancer in humans as reported by *Hanahan, D. and Weinberg R*. **B.** Molecular interaction map of the tumor-suppressor gene, *p53*, and its protein degradation partner MDM2 as reported by *Kohn, K. and Pommier, P.* 2

2.1. Image of the cell capture device as reported by Prokop *et al.* 9

2.2. Schematic of a reactive ion etch chamber (**A**) and a plasma etch chamber (**B**) 18

2.3. Shown here is a pictorial description of step coverage on a substrate following deposition 21

2.4. Schematic diagram of an electron beam evaporator system 22

2.5. In electroplating, metal cations move to the negatively charged substrate and are reduced forming a solid layer of metal on the substrate 24

2.6. Both hot embossing (**A**) and injection molding (**B**) are two common techniques for the rapid production of micro- and nanostructures in polymeric substrates 27

2.7. Shown here is a representation of the top view (**A**) and side view (**B**) of a quartz crystal microbalance device (QCM) 35

2.8. Diagram of a surface plasmon resonance (SPR) sensor 37

2.9. Representation of backscattering interferometry (BI) with incident light impinging a microchip and a fanned interference pattern produced perpendicular to the direction of the flow cell 39

2.10. Polarimetry signal obtained from the Fourier analysis. Solid dots = experimental data; solid curve = $\cos^2$ fit with R^2 = 0.993 41

2.11. Typical on-chip electropherogram of 5 proteins produced by BI detector 42

3.1. Cross-sectional view of a capillary with rays propagated through the system 53

3.2. Experimental setup of the capillary BI system used to compare the ray and wave based models 57

3.3. Experimental and wave based simulation of interference pattern produced by a capillary 58

3.4. Cross-sectional view of a capillary demonstrating a case of total internal reflection (TIR) 59

3.5. Three flow channel geometries: rectangular, semi-circular, and circular compared by ASAP during optical modeling of BI system 62

3.6. Simulated fringe shift due to changing the RI of the fluid in a rectangular channel (60 µm by 70 µm) by ASAP modeling software 64

3.7. Demonstration of the low frequency (LF), medium frequency (MF), and high frequency (HF) components of the interference pattern produced by a capillary with an ID = 100 µm and an OD = 160 µm 66

3.8. **A.** Low frequency (LF) and middle frequency (MF) components are easily distinguished in the interference pattern produced by rectangular channel geometries. **B.** The magnitude spectrum also demonstrates the presence of two frequencies. Note the absence of any high frequency component 67

4.1. Example of T-topping from overexposure of SU-8 by low UV wavelengths 72

4.2. Generic outline of master production 73

4.3. Procedural schematic of isotropic etch in Si wafer 78

4.4. An image of PDMS poured into the Si wafer (**A**), SEM pictures taken of the Ni shim at different magnifications (**B**), a two annealed Topas polymer injection molded chips forming a circular channel (**C**) and an interference pattern produced from one of the annealed polymer chips (**D**) is shown 81

4.5. Simulated distances different sized molecules diffuse over 30 seconds 83

4.6. Modeled comparison of diffusional mixing with and without a 'squeeze' section 84

4.7. Mixer designs and the chrome mask are shown 85

5.1. Simulations of the multi-pass aspect of light waves in the BI system for circular and semi-circular geometries are shown 89

5.2. Example of a high contrast interference pattern produced by a 70 μm wide and 30 μm tall rectangular channel in the BI system captured with a laser beam analyzer (LBA)..... 90

5.3. Spatial movement of the interference pattern is shown by altering the optical pathlength of light through the system, in this case changing the refractive index of the solution. The shape and periodicity of the intensity profile remain appreciably unchanged by small changes to the optical pathlength 91

5.4. Presented here is the FFT magnitude spectrum of the two fringe profiles displayed in Figure 5.3. The fact that the shape and periodicity of the fringe pattern does not change appreciably with small variations in the optical pathlength is further demonstrated here by the fact both fringe patterns have the same spatial frequency 92

5.5. Kinetic simulations using finite element differencing are shown. Both interactions have the same equilibrium binding parameters and would thus be perceived as identical by steady-state analysis. However, as the kinetic traces exhibit, the two systems are very dissimilar 96

5.6. Expected linear relationship of the observed rate versus the initial concentration of L 99

6.1. Photobiotin is activated upon exposure to UV light promoting insertion into the oxidized PDMS substrate. Avidin binds strongly to the immobilized layer of biotin. The tetrameric nature of avidin signifies that it can simultaneously bind the surface bound biotin as well as any biotinylated target molecule that passes through the channel 110

6.2. Experimental setup for BI molecular interaction assays (*not drawn to scale*) 111

6.3. Immobilized protein A was interrogated five times with a 0.5 mg/mL solution of IgG 113

6.4. Shown is the binding affinity of a complementary DNA strand to an immobilized target over multiple complementary strand. The complementary strand is also compared to a 3bp mismatch and control strands at high concentration. All probe strands were allowed 20 minutes for hybridization 114

6.5. Generic quaternary structure of the symmetric dimer formed by immunoglobulins 116

6.6. Digital picture of the BI experimental setup (A), microscopic image of the photolithographic mask containing the mixer design used (B), and a digital image of a microreactor chip molded in PDMS (C) 117

6.7. Real-time kinetics of P_A interacting with different concentrations of the F_C fragment of IgG (black traces) and a control (red trace) consisting of the F_{AB} fragment of IgG 118

6.8. Kinetic analysis (**A**) of the P_A•IgG interaction yields a linear relationship for the observed rate of reaction over the concentration range of IgG studied. An end point analysis (**B**) of the signal determined at steady-state conditions was analyzed using nonlinear regression techniques built-in to Prism® fitting software. Both analysis techniques of BI data produce K_D values very similar to each other and well within accepted literature values 119

6.9. Structural comparison of the apo- and holo-states of calmodulin. The four calcium (red dots) binding loops are indicated. Apo-calmodulin (pdb = 1CFD) and holo-calmodulin (pdb = 1CLL) were taken from the Protein Data Bank and displayed using the freeware Chimera 121

6.10. Ribbon structure of holo-calmodulin observed after binding to trifluoperazine. Holo-calmodulin (pdb = 1CLL) and the trifluoperazine bound species (pdb = 1CTR) were taken from the Protein Data Bank and displayed using the freeware Chimera 122

6.11. A surface structural comparison of holo-calmodulin to trifluoperazine bound holo-calmodulin better demonstrates the compaction seen upon ligand binding 122

6.12. Kinetic traces (black) of the association of calmodulin with a small ion (A), a small molecule inhibitor (B), a small peptide (C), and a large protein (D) as detected in real-time by BI. Control experiments (red traces) produced no appreciable signal 125

6.13. The observed rates calculated by nonlinear regression of the association curves of calmodulin interacting with calcium (A), trifluoperazine dihydrochloride (B), MLCK (C), and calcineurin (D) plotted as a function of ligand concentration 126

6.14. Steady-state analyses of the molecular interaction between calmodulin and calcium (A), trifluoperazine dihydrochloride (B), MLCK (C), and calcineurin (D). The parameter a describes the asymptotic region of the association curve and is found by iterative nonlinear regression of said curve. Red traces indicate the 95% confidence limit 128

6.15. Variable quaternary structures of notable sHsp courtesy of Haslbeck, *et.al* 135

6.16. Amino acid sequence of selected sHsp underscoring the disordered, hydrophobic N-terminal region and the more conserved α-crystallin domain. Taken from Kim, K.K. *et.al* 136

6.17. The dynamic system of sHsp•T4L is shown including: T4L transition from native state to unfolded protein, dissociation of the sHsp multimer into multiple oligomers, and the bi-modal nature of binding 142

6.18. The molecular interaction of αB-D3•T4L-L99A was monitored by BI with kinetic traces displayed in **A**. The association curves were fit to a double exponential (red lines in A) with the observed rates plotted as a function of L99A concentration (**B**). Analysis of the steady-state data (blue triangles in **C**) allows for the determination of K_D. The linear rise in starting values of the kinetic traces, as shown by the orange rectangles in **C** and **D**, was attributed to the response of BI to increased concentrations of free L99A as verified by a calibration curve with the same slope in **D** 143

6.19. Isothermal titration calorimetry (ITC) was used to separately evaluate the αB-D3•T4L-L99A. Heat evolved after each injection (10 μL L99A) was detected (**A**) for 25 injections. The area under the curve was extracted and plotted against the molar ratio to determine thermodynamic data (**B**) 144

6.20. αB-D3 binding multiple concentrations of T4L-D70N was monitored by BI with kinetic traces displayed in **A**. The association curves were fit to a single (blue) and double (red) exponential with the residuals for [T4L-D70N] = 90 μM displayed in **B**. The double exponential was statistically superior at fitting the kinetic data. Interference patterns recorded by BI are shown for both T4L mutants in **C**. The overlap in the fringe patterns of the mutants demonstrates BI is insensitive to inherent differences in their stabilities. A zoomed in region of the T4L mutants interference patterns are shown and compared to a pattern from a buffer solution indicating the sensitivity of the instrument to changes in refractive index. Analysis of the steady-state data (**D**) clearly shows the magnitude of binding as detected by BI for αB-D3•T4L-L99A is significantly greater than seen with αB-D3•T4L-D70N. As a control, αB-D3 was assayed against multiple concentrations of WT-T4L, exhibiting no binding across the concentration range 147

6.21. Interaction of αA-R49C-crystallin with multiple concentrations of βB1-crystallin at physiologically relevant conditions as detected by BI 151

7.1. Modeled positional shift for various solutions of glycerol in a rectangular channel 164

7.2. Measured fringe shifts by BI for added affinity layers with changes compared to modeled data 165

7.3. Semi-circular channel etched in Silicon with laser ablation being used to open the nitride mask for wet etching 165

LIST OF ABBREVIATIONS

BI = Backscattering Interferometry

Bio-NEMS = Bio-NanoElectroMechanical Systems

CCD = Charge Coupled Device

CE = Capillary Electrophoresis

CNC = Computer Numerical Control

CVD = Chemical Vapor Deposition

DARPA = Defense Advanced Research Projects Agency

DC = Direct Current

DOD = Department of Defense

DRIE = Deep Reactive Ion Etch

EBL = Electron Beam (e-beam) Lithography

EOF = Electroosmotic Flow

EU = European Union

FDTD = Finite-Difference Time Domain

FE = Field Emission

FET = Field Effect Transistor

FFT = Fast Fourier Transform

GC = Gas Chromatography

HPLC = High Performance Liquid Chromatography

Hsp = Heat shock protein

IR = Infrared

IC = Integrated Circuit

K_D = Equilibrium Dissociation Constant

LASIK = Laser-Assisted in Situ Keratomileusis

LIGA = Lithographie Galvanoformung Abformung

LIF = Laser Induced Fluorescence

MLCK = Myosin Light Chain Kinase

MPC = Monolayer-Protected Cluster

NIH = National Institutes of Health

NNI = National Nanotechnology Initiative

NSF = National Science Foundation

NW = Nanowire

OCT = Optical Coherence Tomography

PDMS = Polydimethylsiloxane

QCM = Quartz Crystal Microbalance

QD = Quantum Dots

R&D = Research and Development

RF = Radio Frequency

RI = Refractive Index

RIE = Reactive Ion Etch

RIU = Refractive Index Units

SAM = Self-Assembled Monolayer

sHsp = small Heat Shock Protein

SPR = Surface Plasmon Resonance

T4L = T4 Lysozyme

T_g = Glass Transistion Temperature

TIR = Total Internal Reflection

UV = Ultraviolet

Vis = Visible

XRL = X-ray Lithography

μ-TAS = micro-Total Analysis Systems

CHAPTER I

INTRODUCTION

Integration of nanoscale science into biological and medicinal applications has risen over the past decade with current funding policies reflecting this movement to 'bio'-nanotechnology.[1] While its initial use was primarily restricted to miniaturized separation techniques, nanoscale science has found multiple inroads to the scientific landscape. Whether used in artificial muscles[2], gene therapy[3], drug development[4] and administration[5, 6], point-of-care detection[7], diagnostic imaging[8, 9] or therapeutic evaluation, science performed at the nanoscale is a powerful tool with far reaching potential. Molecular interactions and investigations into their kinetic and thermodynamic behavior have been at the forefront of bio-nanotechnology. It is here our primary focus lies with the characterization and development of a sensing modality capable of studying solution phase, label-free molecular interactions in a nanoscale format with high sensitivity (attomoles) and over a large dynamic range.

Life itself is governed by molecular interactions, therefore insight into these interactions offer knowledge about processes such as replication, catalysis, and mutation. In fact, molecular interactions help to regulate cell signaling, molecular recognition and transport, synthesis, and even cell death. The knowledge garnered from the study of molecular interactions help scientists better explain systems in their entirety, a reductionist approach termed systems biology. Variations in the concentrations or structures of molecules, that occur either naturally or in response to stimuli, are commonly monitored to provide insight into more complex biological processes. Yet the vast cadre of molecules that can be involved in a process can be overwhelming. Furthermore, many of the substituents are in low abundance requiring highly sensitive approaches to monitor physiologically relevant conditions.

Arguably, nowhere is this more prevalent than disease related research and therapeutics. For instance, in 2004, the United States spent an estimated 14.4 billion dollars on cancer

research and affiliated drug development. Yet the clinical success rate of oncology drugs is merely 5% with failure determined late in the drug discovery process, further exacerbating costs.[10] In fact, over the last fifty years, mortality rates for cancer-related diseases have remained relatively stagnant. While in the same time period, deaths related to heart disease have been reduced by a factor of two.[7] The classical drug discovery process has been hindered by long development times. Processes such as biomarker recognition, drug synthesis, pharmacokinetic studies, pharmacodynamics, and therapeutic evaluation drain resources and can take several years for completion. These problems are intensified by the shear magnitude of

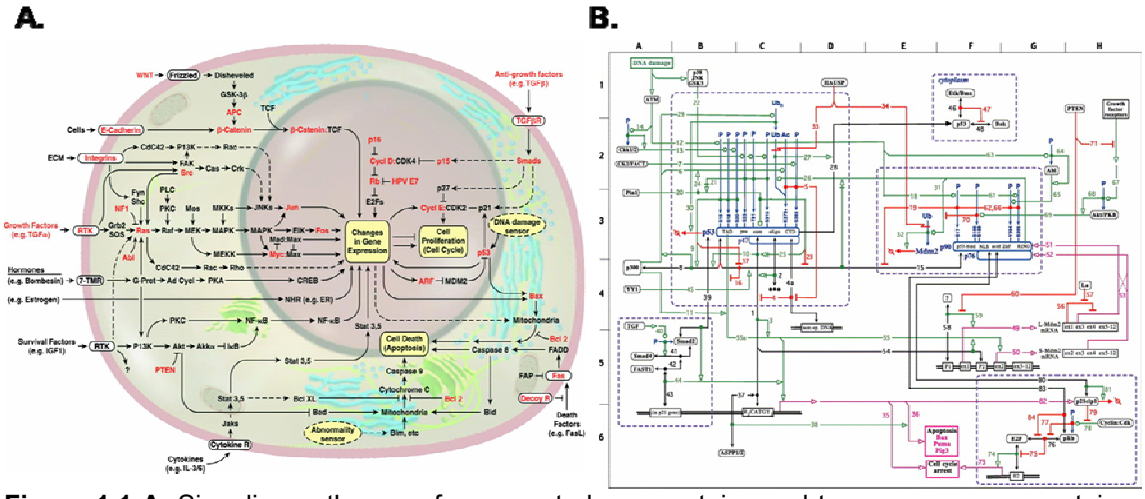

Figure 1.1 A. Signaling pathways of some noted oncoproteins and tumor-suppressor proteins relevant to cancer in humans as reported by *Hanahan, D. and Weinberg R*. **B.** Molecular interaction map of the tumor-suppressor protein, p53, and its protein degradation partner MDM2 as reported by *Kohn, K. and Pommier, P*.

potential biomarkers and drug candidates with each possibly affected by an infinite combination of conditions and interactions. Figure 1.1 gives some insight into this diversity showing some noted signaling pathways relevant to human cancers (Figure 1.1A)[11] and the molecular interaction map of one such protein (Figure 1.1B)[12]. Improvements in the monitoring of drug interactions on a molecular level must be met in order to ease attrition rates for drug discovery while simultaneously reducing the time and money spent during the process.

In order to accurately characterize molecular interactions, determinations should be performed *without* modifying the molecules of interest.[13, 14] Furthermore, to have the capability to fully evaluate the molecular diversity that exists not only in disease research and drug

development, but all of nature, it would be most advantageous to make these determinations with nanoscale devices configured for high throughput.[15-18] The inherent small size of working with miniaturized devices allow for molecular interactions to be studied with limited amounts of material, at drastically reduced costs, and much faster analysis times.

However, traditional tools available to quantify molecular interactions are often volume or sensitivity limited, both impediments to performing systems biology analyses in nanoscale devices.[19, 20] Other common detection modalities require some modification of the analyte. Laser-induced fluorescence (LIF)[21, 22] for instance, is a highly sensitive detection method amendable to analyzing molecular interactions on the nanoscale.[23] Yet LIF studies often require functionalization of the molecule with a signaling moiety since most do not auto-fluoresce. This chemical modification can inhibit analyte production, alter its native structure, and affect interaction parameters.

Investigators have developed methodologies capable of label-free detection for use specifically with miniaturized devices including: electrochemical sensors[24-26] (most notably nano-electrodes[27-29]), resonators[30-32], and novel refractive index (RI) sensors[33-35] such as Surface Plasmon Resonance (SPR)[36, 37]. While each of these techniques offers their own unique advantages (*see section 2.2*), all are still plagued with the need for surface immobilization of a target molecule which present persistent problems (*see section 2.3*).

The ability to perform solution phase molecular interactions in a miniaturized, label-free format would eliminate many of the problems associated with molecular immobilization and modification, facilitating a more accurate assessment of interaction assays in small volumes and at physiologically relevant conditions. Label-free investigations are of particular importance to big pharma where traditional techniques (e.g. fluorescent assays) require larger amounts of precious sample. Even worse, fluorescent tags are roughly the same size and molecular weight as common drug compounds. Thus fluorescent labeling essentially doubles the mass and dimensions of the native molecule altering kinetics and potentially disrupting binding site recognition.

Presented here is a method which offers such utility. Termed throughout as backscattering interferometry (BI), the system is an ultra-sensitive and universal technique with the ability to circumvent the use of immobilization chemistries and perform molecular interactions in a label-free and fully integrated nanoscale format**.** Developed in 1995[38], BI utilizes a simple optical train to probe picoliter volumes in miniaturized devices. Extremely simple and inexpensive to implement, the technique has been adopted by a number of research groups (RISØ National Laboratory in Denmark[39, 40], Microgravity Research Group at NASA's Glenn Research Center, and others[41-43]). Investigations into the light propagation through BI as well as miniaturized design and fabrication of devices amendable to BI will be discussed. Furthermore, physiologically relevant applications will also be discussed with a primary focus on the techniques ability to study solution phase, label-free molecular interactions at high sensitivity (attomoles) and over a large dynamic range.

(1) NNI, N. N. I., www.nano.gov.

(2) Samatham, R.; Park, I. S.; Kim, K. J.; Nam, J. D.; Whisman, N.; Adams, J. *Smart Materials & Structures* **2006**, *15*, N152-N156.

(3) Iwasaki, Y.; Ueda, M.; Yamada, T.; Kondo, A.; Seno, M.; Tanizawa, K.; Kuroda, S.; Sakamoto, M.; Kitajima, M. *Cancer Gene Therapy* **2007**, *14*, 74-81.

(4) Collins, I.; Workman, P. *Nature Chemical Biology* **2006**, *2*, 689-700.

(5) Brigger, I.; Dubernet, C.; Couvreur, P. *Advanced Drug Delivery Reviews* **2002**, *54*, 631-651.

(6) Hughes, G. A. *Dm Disease-a-Month* **2005**, *51*, 342-361.

(7) Soper, S. A.; Brown, K.; Ellington, A.; Frazier, B.; Garcia-Manero, G.; Gau, V.; Gutman, S. I.; Hayes, D. F.; Korte, B.; Landers, J. L.; Larson, D.; Ligler, F.; Majumdar, A.; Mascini, M.; Nolte, D.; Rosenzweig, Z.; Wang, J.; Wilson, D. *Biosensors & Bioelectronics* **2006**, *21*, 1932-1942.

(8) Manning, H. C.; Goebel, T.; Thompson, R. C.; Price, R. R.; Lee, H.; Bornhop, D. J. *Bioconjugate Chemistry* **2004**, *15*, 1488-1495.

(9) Bornhop, D. J.; Contag, C. H.; Licha, K.; Murphy, C. J. *Journal of Biomedical Optics* **2001**, *6*, 106-110.

(10) Kola, I.; Landis, J. *Nat Rev Drug Discov* **2004**, *3*, 711-715.

(11) Hanahan, D.; Weinberg, R. A. *Cell* **2000**, *100*, 57-70.

(12) Kohn, K. W.; Pommier, Y. *Biochem Biophys Res Commun* **2005**, *331*, 816-827.

(13) Cooper, M. A. *Analytical and Bioanalytical Chemistry* **2003**, *377*, 834-842.

(14) Torres, F. E.; Kuhnt, P.; De Bruyker, D.; Bell, A. G.; Wolkin, M. V.; Peeters, E.; Williamson, J. R.; Anderson, G. B.; Schmitz, G. P.; Recht, M. I.; Schweizer, S.; Scott, L. G.; Ho, J. H.; Elrod, S. A.; Schultz, P. G.; Lerner, R. A.; Bruce, R. H. *Proceedings of the National Academy of Sciences of the United States of America* **2004**, *101*, 9517-9522.

(15) Ferrari, M. *Nat Rev Cancer* **2005**, *5*, 161-171.

(16) Hansen, C.; Quake, S. R. *Current Opinion in Structural Biology* **2003**, *13*, 538-544.

(17) Heath, J. R.; Phelps, M. E.; Hood, L. *Mol Imaging Biol* **2003**, *5*, 312-325.

(18) Sia, S. K.; Whitesides, G. M. *Electrophoresis* **2003**, *24*, 3563-3576.

(19) Liang, Z. H.; Chiem, N.; Ocvirk, G.; Tang, T.; Fluri, K.; Harrison, D. J. *Analytical Chemistry* **1996**, *68*, 1040-1046.

(20) Verpoorte, E.; Manz, A.; Ludi, H.; Bruno, A. E.; Maystre, F.; Krattiger, B.; Widmer, H. M.; Vanderschoot, B. H.; Derooij, N. F. *Sensors and Actuators B-Chemical* **1992**, *6*, 66-70.

(21) Barnes, M. D.; Whitten, W. B.; Ramsey, J. M. *Analytical Chemistry* **1995**, *67*, A418-A423.

(22) Haab, B. B.; Mathies, R. A. *Analytical Chemistry* **1999**, *71*, 5137-5145.

(23) Fister, J. C.; Jacobson, S. C.; Davis, L. M.; Ramsey, J. M. *Analytical Chemistry* **1998**, *70*, 431-437.

(24) Cai, X. X.; Klauke, N.; Glidle, A.; Cobbold, P.; Smith, G. L.; Cooper, J. M. *Analytical Chemistry* **2002**, *74*, 908-914.

(25) Li, M. W.; Spence, D. M.; Martin, R. S. *Electroanalysis* **2005**, *17*, 1171-1180.

(26) Wegner, G. J.; Lee, N. J.; Marriott, G.; Corn, R. M. *Analytical Chemistry* **2003**, *75*, 4740-4746.

(27) Cui, Y.; Wei, Q. Q.; Park, H. K.; Lieber, C. M. *Science* **2001**, *293*, 1289-1292.

(28) Hahm, J.; Lieber, C. M. *Nano Letters* **2004**, *4*, 51-54.

(29) Yotter, R. A.; Lee, L. A.; Wilson, D. M. *Ieee Sensors Journal* **2004**, *4*, 395-411.

(30) Gerdon, A.; Wright, D.; D., C. In *Nanotechnologies for the Life Sciences*; Kumar, C., Ed.; WILEY, 2006; Vol. 3, pp 109-144.

(31) Gerdon, A. E.; Wright, D. W.; Cliffel, D. E. *Angewandte Chemie-International Edition* **2006**, *45*, 594-598.

(32) Janshoff, A.; Galla, H. J.; Steinem, C. *Angewandte Chemie-International Edition* **2000**, *39*, 4004-4032.

(33) Lin, V. S. Y.; Motesharei, K.; Dancil, K. P. S.; Sailor, M. J.; Ghadiri, M. R. *Science* **1997**, *278*, 840-843.

(34) Prieto, F.; Sepulveda, B.; Calle, A.; Llobera, A.; Dominguez, C.; Abad, A.; Montoya, A.; Lechuga, L. M. *Nanotechnology* **2003**, *14*, 907-912.

(35) Prieto, F.; Sepulveda, B.; Calle, A.; Llobera, A.; Dominguez, C.; Lechuga, L. M. *Sensors and Actuators B-Chemical* **2003**, *92*, 151-158.

(36) Besenicar, M.; Macek, P.; Lakey, J. H.; Anderuh, G. *Chemistry and Physics of Lipids* **2006**, *141*, 169-178.

(37) Boozer, C.; Kim, G.; Cong, S. X.; Guan, H. W.; Londergan, T. *Current Opinion in Biotechnology* **2006**, *17*, 400-405.

(38) BORNHOP, D. *APPLIED OPTICS* **1995**, *34*, 3234-3239.

(39) Sorensen, H.; Larsen, N.; Latham, J.; Bornhop, D.; Andersen, P. *APPLIED PHYSICS LETTERS* **2006**, *89*, -.

(40) Sorensen, H.; Pranov, H.; Larsen, N.; Bornhop, D.; Andersen, P. *ANALYTICAL CHEMISTRY* **2003**, *75*, 1946-1953.

(41) El Ghandoor, H.; Hegazi, E.; Nasser, I.; Behery, G. M. *Optics and Laser Technology* **2003**, *35*, 361-367.

(42) Qi, S. W.; Yang, X. Q.; Zhang, C. P.; Zhang, L. S.; Wang, X. Y.; Xu, T.; Tian, J. G.; Zhang, G. Y. *Applied Optics* **2004**, *43*, 530-536.

(43) StClaire, J.; Hayes, M. *ANALYTICAL CHEMISTRY* **2000**, *72*, 4726-4730.

CHAPTER II

BACKGROUND

2.1 Nanotechnology and Microfluidics in Science

2.1.1 *Early Inception*

Does size really matter? Trends in current scientific research would suggest it does and based on those trends, **smaller** is better. Eagerness to champion particles, devices, and applications as "smaller" is pervasive throughout the literature of many scientific fields. Furthermore, the subtext is generally seen as a major improvement over previous studies and thus of high impact. Two fields in particular have helped to galvanize the movement to miniaturization: *nanotechnology* and *microfluidics*.

Nanotechnology, as defined by the National Nanotechnology Initiative (NNI)[1], is the ability to work at the atomic, molecular, and supramolecular levels (on a scale of ~1 – 100nm) in order to understand, create and use materials, structures, devices and systems with fundamentally new properties and functions resulting from their small structure. Bulky and yet restrictive, alternative definitions have been introduced into the literature. Jianrong *et.al* explains nanotechnology as involving the study, manipulation, creation and use of materials, devices and systems typically with dimensions smaller than 100nm.[2] Ferrari describes nanotechnology more broadly as a multidisciplined field covering devices and techniques from engineering, biology, physics, and chemistry.[3] Yet even more expansive, Whitesides remarks that the zeal for nano should be balanced with micro-techniques, describing a 'right' size for nanotechnology based on the question posed. Whitesides correctly points out sizes of structures can range from nanometers to millimeters for chemical and biological applications in nanoscience, even within a single device.[4] For instance, a cell capture device as used by Prokop *et.al*[5] (Figure 2.1) can be composed of thousands of traps spanning several millimeters. Structures fabricated for the

individual traps are on the order of microns. While electrodes deposited for analyte detection or molecules used to passivate the surface can be in the nanometer regime. Even biomolecules of interest in the cell capture device can span orders of magnitude in size. Individually trapped mammalian cells are roughly 10 – 20μm in diameter, yet most of the frequently observed analytes secreted by said cells are in the low nanometer range. Still, it is the integration of engineering and the physical sciences with biology and medicine on a 'small' scale that gives nanotechnology enormous potential and future groundbreaking opportunities.

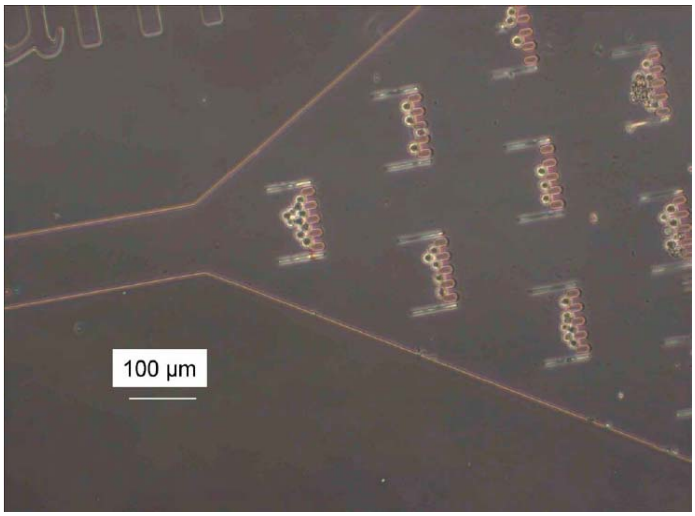

Figure 2.1. Image of the cell capture device as reported by Prokop *et al.*

However narrow or broadly one chooses to define nanotechnology, evidence of its emergence as a dynamic field can be seen in scientific research budgets over the past decade. In 1997, the United States (US) government spent $116 million dollars in nanotechnology research and development (R&D). By 2002, two federal agencies each, the National Science Foundation (NSF) and the Department of Defense (DOD), had invested nearly twice that amount in R&D for nanotechnology. Total R&D funding in nanotech by the US government was $989 million dollars in 2003, representing an 88.3% increase in spending over the 7-year span. Similar trends in research budgets can be seen across the world. The European Union's (EU) increase in nanotech spending over the same 7-year period was ~79%. Japan, second only to the US in nanotech funding, budgeted ~$810 million dollars for the 2003 fiscal year. Worldwide, more than $9.5 billion dollars was spent on nanotech R&D in 2005 with the US representing 27% of that investment. And by 2008, global demand for devices, tools, and materials on the nanoscale will surpass $28 billion dollars. *(All monetary figures were reported by the NNI at www.nano.gov.)*

Long-term growth and advancement in nanotechnology has also been acknowledged by the US as a priority. The NSF has founded an integrated system of user facilities at 13 university sites to support research in nanoscale science, engineering, and technology. Termed the National Nanotechnology Infrastructure Network (NNIN), this system was founded by the NSF in 2004 and is led by Cornell University. In addition, NASA, NIH, NSF, and DOD help to fund centers of excellence across the US. These centers are setup to provide support and the opportunity for multidisciplined research with emphasis on collaboration across scientific fields, academic institutions, and industrial and governmental laboratories. There are currently over 50 such centers spread across the US.

The second field key to the immergence of miniaturization is microfluidics. Defined as the science and technology involved with the manipulation or processing of small volumes (10^{-9} to 10^{-18} liters) using channels of tens to hundreds of microns in size, knowledge of microfluidics is a fundamental necessity for any micro- or nanotech device.[6] The field of microfluidics is thought to have emerged as a congruence of four parental subjects: microelectronics, biodefense, molecular biology, and molecular analysis. Many of the techniques employed in microelectronics were successfully transferred (*see 2.1.2*) to the microfluidics industry via micro- and nanotechnology. The threat of biological and chemical agents in the post cold war era led to the development of the Defense Advanced Research Projects Agency (DARPA). A sub-agency of the DOD, DARPA has looked to microfluidics for potential early warning systems in biodefense, providing funding and spurring fledgling microfluidic research. The explosion of molecular biology in the 1980's and 90's due to genomics (and subsequently proteomics) saw an increased need for microanalysis techniques. Furthermore, limited sample sizes required high sensitivity in small volumes. Given the scope of the projects in genomics, the ability to perform analyses in a high throughput manner also became a major consideration. Thus the explosion in molecular biology in the late 20^{th} century, unlike any previous event, led to a direct need for microfluidic devices. Molecular analysis, particularly separation science, was key to the development of microfluidics. Chromatography and electrophoresis strived to drastically reduce sample consumption and increase separation efficiency. Microfluidic designs accomplished both and allowed for the

massive parallelization of separations. The small surface area involved with microfluidics improved heat transfer, a further benefit to electrophoretic separation.

Nanotechnology and microfluidics are commonly intertwined as in nanobiotechnology[1] or bio-nanoelectromechanical systems (bio-NEMS).[7] Microfluidic systems are themselves fabricated using micro- and nanotechnologies.[8] Conversely many applications of bio-nanotechnology require the manipulation of analytes (cells, fluids, etc.) as well as knowledge of transport phenomena unique to microfluidics. Both fields involve a multidisciplined approach with aspects of chemistry, physics, engineering, and biology incorporated with physiologically, biologically, and medically relevant applications. The widespread integration allows for the study of numerous systems and processes. Additionally, the inherent small size of working with microfluidics and nanotechnology allow for these studies to be performed with minute amounts of material, at drastically reduced costs, and much faster analysis times. Coupled with the potential of the two fields, it is easy to comprehend their meteoric rise.

2.1.2 *Fabrication Methods and Materials*

The overall classification of fabrication methods used in micro- and nanodevices can be described as two distinct processing subclasses: *top-down* and *bottom-up.*[9] Top-down processing involves the removal/addition of material from/to a substrate producing a chosen design – the 'master'. Top-down processing, also called dry nanotechnology, relies primarily on the physical sciences and has been developed primarily by physicists, electrical and mechanical engineers. Bottom-up processing is based on the synthesis or fusion of particles (atoms, molecules, viruses, etc.) piece by piece to assemble a larger structure. Often called wet nanotechnology, bottom-up processing has been used and refined by chemists, molecular biologists, and genetic engineers, but rarely for improvement in manufacturing.[10] Instead, these sciences build molecules over a wide range of sizes (from nanometer to micron) with subnanometer resolution (chemical bond lengths) that have important biological relevance. Low molecular weight structures can be synthesized for use as drugs or contrast agents in the battle against and early detection of diseased states.[11-13] Drugs themselves are generally small organic

molecules designed and synthesized by chemists. Biodegradable nanoparticles can be made with a therapeutic agent housed within. These nanoparticles can accumulate at target sites releasing the drug compound over sustained periods of time as a function of the nanoparticle's biodegradability.[14] Nanoparticles can also be used in gene therapy with there small size enabling DNA delivery inside a cell.[15] Liposomes and micelles can be used similarly in targeted delivery with drugs partitioned to their inner core reducing alteration or metabolism of the therapeutic agent and thereby minimizing any reduction in potency.[16] Small molecules, quantum dots (QD), and dendrimers offer both *in-vivo* and *in-vitro* diagnostic capabilities as well as drug delivery.[17] These entities possess targeted delivery and can either enhance contrast or summarily provide recognition of the targeted area by means of numerous imaging modalities.[18] The larger size of QD's and multi-generation dendrimers reduces their function to membrane bound recognition with cytoplasmic targeting and incursion through the blood brain barrier limited.[19] However, QD's and dendrimers do offer multifunctionality with the ability to present different drugs and multiple targeting and signaling moieties. Toxicity and clearance of all types of nanoparticles are still a concern with 'stealth' technologies enabling avoidance of non-self immune response being studied.[20, 21] The biocompatibility of nanotech devices and materials is also a topic of concern. Bottom-up processing has begun to outgrow its focused use in only biological and/or health related fields. Recent interest has grown in photovoltaics[22], white-light emission[23], structural enhancement, nanoscale transistors and motors, and artificial muscles[24]. While wet nanotechnology is outside the scope of this article, a very small insight into a burgeoning and impressive field can be gained in the papers above.

The electronics industry, particularly semiconductor processing (mostly Silicon, Si), rely heavily on top-down processing. As mentioned earlier (*see 2.1.1*), nanotechnology and thus microfluidics owe much of their early success to the top-down processing techniques developed and readily employed in microelectronics. Top-down processing is most frequently used to fabricate a 'master' structure from which replicates are made, although at times, end products are initially produced. Technologies used for master replication will be discussed later.

Top-down processing of devices in small-scale systems can be either subtractive or additive in nature. Subtractive processes remove material from the bulk substrate. This is accomplished in a variety of manners including: micromachining, lithography, photoablation, and etching. Micromachining of substrates is generally carried out using computer numerical control (CNC) of a mill, lathe, or drill. The use of a CNC machine drastically improves quality over manually driven machines with reduction in errors and increased precision, while the inherent automation increases production. Although not substrate specific, micromachining is limited in feature size by the stepper motor and tool used, with resolution in the single micron regime for an ~$5000 instrument. Heating of the substrate can be a problem in micromachining with either a vaporized mist or inert gas needed as coolants to reduce the temperature on the substrate and machine tool. While automation does increase overall production, micromachining is still a serial process.

Lithography can be used to either 'write' directly into a substrate creating the desired master structure or to 'write' designs onto (or in conjunction with) a mask for use in batch master production. Currently, this distinction and the nomenclature prefix of lithography are based upon the radiation source employed. Electron beam (e-beam) lithography (EBL) can be used for both directly writing patterns on surfaces or mask generation. Although expensive (most systems are >$2M USD), EBL is the most wide spread lithography technique used for fabrication of lateral structures below the resolution limit of photolithography (< 200 nm).

Derived from early scanning electron microscopes, generic EBL systems consist of: an electron source, a column of electron optics (i.e. lenses, apertures, knife edges) that shape and focus the electron beam, a mechanical stage that positions the wafer under the electron beam, and a computer for instrumentation control. Most general use EBL systems operate with thermionic emitters as electron sources, tungsten filament and lanthanum hexaboride (LaB_6) the most popular. LaB_6 guns are brighter than tungsten, 10^6:10^5 A/cm^2•sr respectively, and have a longer lifetime. The work function of a LaB_6 emitter is low compared to that of a tungsten filament allowing for more electrons to be emitted at the same temperature. Although thermionic emitters offer fine lateral resolution (10-50 nm) and are inexpensive, they have short lifetimes, large

energy spreads, and relatively low brightness. Field emission (FE) electron guns offer a technically superior alternative over thermionic emitters. With cathode tips generally machined to less than a 100 nm radius, FE guns drastically reduce source size (from ~50 μm to ~5 nm).[25] This decreases the amount of demagnification needed and coupled with their low energy spread allow FE sources enhanced operation at low accelerating voltages. FE electron sources are very robust, with exceptional lifetimes, and have become the typical type of emitter for most applications.

The electron beam produced in EBL systems has a wavelength on the order of picometers, thus this technique is not governed by the Rayleigh limit of resolution. Spherical and chromatic aberrations as well as coulombic interactions are limiting factors in final beam diameter with spot sizes at the substrate surface routinely on the single digit nanometer scale for FE sources. However, in practicality, the final structure size in the mask or substrate is dependant upon the electron interaction volume and can be significantly larger than the reported beam spot size. Beam energy, substrate flatness/tilt, and the substrate itself all influence the interaction volume. Backscattered and secondary electrons off axis from the incident beam also reduce lateral resolution (termed 'proximity effect'). The proximity effect can dominate resolution for low atomic number substrates, especially when using resist material. Also, the accuracy of the mechanical stage for repetitive raster scans in direct write EBL systems can affect lateral resolution although vector scanning techniques or stencils can alternatively be used with no reliance on stage movement. Still high-resolution fabrication of nanometer structures with EBL is commonly achieved with optimized system parameters and properly chosen resists and substrates. Unfortunately, EBL is a serial process. And while allowing for sub nanometer structure fabrication, throughput is extremely slow. This coupled with the cost of EBL systems renders their applicability primarily to mask fabrication or device research and prototyping.

Unlike the serial processing of EBL systems, x-ray lithography (XRL) is a batch processing technique. Used in conjunction with a mask and resist covered substrate, XRL produces the master structure in a single exposure on the order of seconds. The most popular x-ray source used is a synchrotron as typically employed in the LIGA (**Li**thographie

Galvanoformung **A**bformung) process. In a synchrotron, electrons are injected into a storage ring capable of supporting multiple exposure tools. The small wavelength of the x-rays (single Å), like e-beam, indicates the resolution limit is independent of diffraction effects. However, the lack of x-ray optics and the non-uniformity of x-ray sources lead to blurring effects that limit lateral resolution. Still XRL routinely produces structures in the 50-100 nm range for 1:1 proximity exposures. Improved resolution and demagnification have been achieved by taking into account bias and exposing at a near-field 'sweet spot'.[26] The major limitation of XRL is the manufacturing and durability of the masks used. Few materials with appropriate mechanical properties allow high percentage transmission of x-rays. Typically, thin film, low atomic number masks are used in XRL leading to potential pattern distortion due to mechanical stress, thermal expansion, etc. The use of x-rays and electrons in non-optical lithography can also cause undesired radiative damage to resist and substrate layers.

Optical or photolithography is the most widely used of the lithographic techniques. Like XRL, photolithography is a batch processing technique used in combination with a mask and resist coated substrate. Optical lithography uses ultraviolet (UV) or visible light sources during the exposure process with i-line sources (365 nm) the most common. The longer wavelengths employed in photolithography cause lateral structural resolution to be diffraction limited. The diffraction effects can be lessened by contact printing which reduces the gap between the photomask and the substrate to almost zero. The resolution of most general use cleanroom mask aligners is on the order of the light source's wavelength, thus 365-500 nm. Photolithographic systems can be some 50x less expensive than XRL and EBL setups with far less expensive radiation sources and optics as well as lower operational costs. It is of some significance to note that high resolution photomasks used in both XRL and optical lithography still must be fabricated using EBL. The step-by-step process and resists used in photolithography will be discussed in detail later (*see 4.1*).

Photoablation is another subtractive technique used in top-down processing. Material is removed from the substrate by an intense light source altering the surface on a mesoscopic length scale.[27] Photoablation occurs when electronic or vibrational modes in the substrate are

excited by absorption of light. Photochemical and photothermal processes are initiated by the absorbed energy causing ejection of a gaseous plume of vaporized/sublimed substrate. Ablation is a threshold process heavily dependent upon the substrate material, wavelength of light used, fluence and duration. Light absorption is substrate specific and the wavelength of light chosen is based on the maximum absorption for each material. UV wavelengths are absorbed strongly by organic materials. Therefore most commercial polymers are ablated with UV light sources by means of a photochemical pathway resulting in minimal heating of the polymer substrate. Longer wavelengths in the infrared (IR) or near-infrared regime are generally used to ablate metals, typically by a photothermal process. Lasers are the light source of choice in photoablation with CO_2 and Nd:YAG lasers servicing the IR wavelengths and excimer lasers for the UV region. The use of fast-pulsed lasers has become prevalent in ablation processing due to the significant advantages of optics at critical intensity. Short laser pulses localize the energy distribution to the substrate, so much so that ablated structures are no longer diffraction limited and the fluence threshold flattens.[28] Lasers pulsed at rates less than 5 picoseconds make ablation a deterministic process with reproducibility of 99%.[29] Ultra short-pulsed lasers also minimize thermal effects to surrounding areas. This is made apparent by their use in medical procedures involving tissue, particularly the common corrective eye procedure LASIK (**L**aser-**A**ssisted in **Si**tu **K**eratomileusis). Fast-pulsed lasers even allow for ablation of materials normally transparent to the laser's wavelength due to absorption of focused, high peak intensities. Laser ablation can be used to process structures in sizes ranging from 20 nm to 10's of microns.[30, 31] Though typically a serial process, photoablation can be used with a mask for batch production. Recently, a properly focused femtosecond laser was used to ablate structures embedded into a glass substrate allowing for the direct writing of 3-D structures.[32, 33] However, surface debris and structural homogeneity are concerns for topical and embedded laser ablated structures.

The last subtractive technique in top-down processing discussed is etching. Etching is the most widely used process for the removal of material from a substrate. Etches can be divided into wet (liquid phase) or dry (plasma and gas phase) methods.[34] Wet etches attack the substrate in a purely chemical manner and can be highly selective to the material. Wet etches

also tend to be isotropic in nature, meaning they remove material from a substrate at equal rates in all directions. However, the combination of some wet etchant chemistries can be used to remove material from substrates in an anisotropic manner. Anisotropy describes directionality of the etch in the lateral and vertical dimensions by the equation: $A = 1 - R_L/R_V$ where R_L and R_V refer to the lateral and vertical etch rates respectively.[35] A process whose etch in the vertical dimension is much faster than the lateral (A is essentially equal to one) is said to be perfectly anisotropic. Wet etching processes are generally pot processes with little mixing and/or sonication. These stagnant mixtures do not replenish chemicals and can have etch rates that vary depending upon: temperature, etch duration, evaporation, mixing, formation of gases (i.e. bubbles), structural or film stress, and contamination. Common chemicals used as wet etchants include weak and strong acids, alkali hydroxides, peroxides, hydrazine, amine gallates, and metal nitrates.[36] Different combinations and ratios can be used to etch a multitude of materials at different rates and with varying degrees of anisotropy. Metalloids (particularly Silicon, Germanium, and Arsenic), transition metals (Gold, Chromium, Molybdenum, and Titanium), alloys, silicas, and resists are all materials commonly wet etched. The variable wet etch rates for different substrates is frequently exploited by depositing protective masks onto areas where no substrate removal is desired. For example, potassium hydroxide (KOH) is frequently used to anisotropically etch Si at a rate of 1.4 μm/min. Silicon dioxide (SiO_2) or silicon nitride (Si_3N_4) can be deposited in selected regions as a protective mask for Si during KOH etching since the etch rate for SiO_2 is 1.4 nm/min and 0 nm/min for Si_3N_4.[37] The techniques used for the deposition of thin films and a description of the isotropic etch of Si are discussed later in some detail (*see further this section and 4.2.1 respectively)*.

Dry etching processes rely on more physical damage to the substrate, although a combination of physical and chemical attack may be used in some techniques. Dry etch rates are generally less dependent upon the substrate material. They also tend to be highly anisotropic, with etch rates contingent upon an axis/crystal plane. Dry etching processes also use a continuous supply of fresh etchants, reducing contamination and etch rate variability. However, many of the gases/plasmas used in dry etches are either hazardous or produce hazardous

byproducts resulting in the need for very expensive neutralization, ventilation, and detection systems. Ion milling, high-pressure plasma etching, and reactive ion etching (RIE) are all dry etch techniques.

Ion milling is a purely mechanical dry etch process. Running at low pressures (10^{-3} –10^{-5} Torr), ion milling uses noble gases to erode material from the substrate with no chemical reactions taking place. The ion beam is accelerated toward the wafer by a strong vertical electrical field. Directionality is maintained by the chamber's low pressure, minimizing atomic collisions. Ion milling is applicable to almost any substrate with etch rates varying by no more than a factor of two across the different materials used. However, since material etched from the target is non-volatile, re-deposition can be a problem in ion milling creating a heterogeneous surface. While widely applicable, since the erosion rate does not vary much from material to material the ability to use protective masks is reduced. Furthermore, mask erosion can lead to the transfer of any tapers or abnormalities to the target as well as cause trenching effects. Small ion sources and slow etch rates render ion milling a serial process incapable of high throughput.

High pressure plasma and RIE are similar dry etching techniques (Fig. 2.2). Feed gases are introduced into a chamber and ionized. The ionized species are directed to the wafer surface reacting with exposed substrate. The newly formed product is desorbed from the surface (i.e. etched) and transported by the carrier gas out of the target chamber. However, RIE instruments not only remove substrate by surface reactions but also by ion bombardment, a result of their differing instrumental design. High pressure plasma etching chambers have symmetric, parallel plate electrodes through which gas is fed. The wafer is on a grounded electrode while the top electrode is powered by a radio frequency (RF). The oscillating electric field accelerates free electrons in the chamber. Inelastic

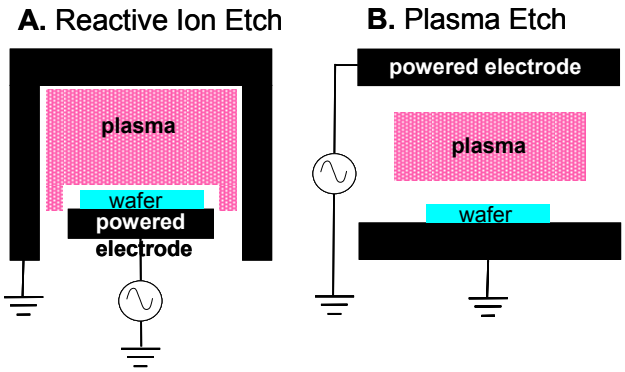

Figure 2.2. Schematic of a reactive ion etch chamber (**A**) and a plasma etch chamber (**B**).

collisions between the free electrons and the feed gas form ions with additional electrons (secondary) post-impact helping to sustain the plasma. A high voltage arc will flash between the two electrodes creating a 'glow discharge'. The high pressure used contracts the plasma away from the walls and focuses it in the middle of the chamber. Electrons in the plasma strike the surface of each electrode with every alternating RF cycle giving them a net negative charge. This creates a potential difference between the electrodes and the plasma characterized by a central glow in the chamber region and sheath regions near the electrodes. The DC voltage drop accelerates positive ions in the plasma toward both electrodes and thus the wafer. Since high pressure plasma etchers have symmetric electrodes with the same surface area the potential difference between each electrode and the plasma is equal. Thus, the equivalent voltage drops coupled to the contraction of plasma due to the high pressures results in a mere migration of ions to the substrate surface where low kinetic energies offer little physical etching. Furthermore, this more diffusive process offers less anisotropy.

The instrumental design of reactive ion etchers differ in two aspects that profoundly enhance performance.[36] First, the RF power supply is connected to the lower electrode housing the wafer. Second, the upper electrode is connected to the walls of the chamber, greatly increasing the effective surface area. Increasing the surface area of the upper electrode maximizes the voltage difference between the lower electrode and the plasma.[38, 39] Ions in the plasma are then accelerated toward the lower electrode, bombarding the wafer with a greatly increased kinetic energy. Since RIE chambers are under vacuum, the plasma remains in close proximity/contact to the walls unlike high pressure plasma etching. This reduces the vertical distance of the sheath region. The short distance together with high ion bombardment energies gives excellent anisotropic etches.

Deep reactive ion etch (DRIE) is a highly anisotropic form of dry etching very similar to RIE. Two techniques can be used to achieve DRIE: cryogenic and pulsed. In cryogenic DRIE, the wafer housing is cooled with liquid nitrogen and helium gas flow. The decreased temperature greatly slows the isotropic etching by diffused reactants, leaving only the vertical ion bombardment as an etchant. In fact reactant gases condense on the sidewalls protecting them

from lateral etching. In pulsed DRIE, processing is alternated between etching and protective polymer deposition. After the initial etch with the reactive gas chosen for the particular substrate has proceeded for a few seconds, the chamber is flushed with argon and a fluorocarbon gas (generally C_4F_8). All exposed surfaces are then coated with a teflon-like polymer. Etching is again initiated by introduction of the reactive gas. The vertical ion bombardment will quickly remove the fluorinated polymer from the horizontal surface. Substrate removal in this plane will again proceed while lateral etching of the sidewalls is negated. The process is repeated until the desired depth is reached.

Reactive ion etching can be a purely anisotropic process. The technique is a favorite in nanoscale fabrication for its precision and reproducibility. Large planar or hexagonal chambers allow for batch processing of wafers, increasing throughput. Care must be taken with dopants used in the substrate though as they can drastically alter etch rates. The high ion energies delivered in RIE are also a concern as they can cause chemical contamination and substrate damage. The feed gases and their byproducts must also be monitored (expensive) during RIE as they are potentially harmful to people and the environment.

Additive processes in top-down manufacturing are used primarily to deposit thin films on substrate surfaces to act as protective masks or sacrificial layers as mentioned above. Common techniques in additive processing include: sputtering, evaporation, chemical vapor deposition (CVD), electroplating, and spin coating. The instrumental design used for sputtering is very similar to that employed by parallel plate plasma etching (*see Figure 2.2A*). A carrier gas is fed into a chamber with two parallel plates under a small vacuum. A voltage is applied to these plates resulting in ionization of the carrier gas and subsequently a glow discharge. Ions in the plasma are accelerated toward the cathode holding the target material, unlike RIE which houses the wafer at the cathode. Clusters of atoms are then ejected from the target material and deposit on the wafer surface. The low vacuum of the chamber and the increased interaction volume of high molecular weight targets yields sputter paths with widely varying angular trajectories. The elevated energies of atoms ejected from the target improve these particles mobility at the wafer surface. Both of these two factors greatly enhance step coverage of the wafer when sputtering

(Figure 2.3). Step coverage refers to the ability of a deposition technique to cover surface topology. Excellent step coverage entails equal film thickness over vertical and horizontal walls of the wafer, as in sputtering. Sputtering can be used to deposit a variety of materials onto selected substrates, with extensive use in the deposition of metals and alloys.

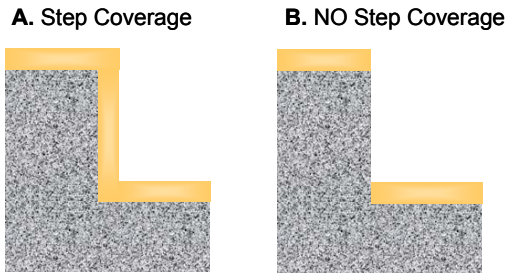

Figure 2.3. Shown here is a pictorial description of step coverage on a substrate following deposition.

Evaporation is another common technique used in the deposition of thin films on substrate surfaces. In evaporation, a crucible containing the target material (charge) to be deposited on the wafers is heated within a high vacuum chamber. The elevated temperature of the charge causes a viscous flow just above (~10 cm) the crucible creating a virtual point source, emanating radially outward. Deposition rates at each wafer will thus vary depending on the distance and angle from the crucible. In order to achieve uniform film coverage, wafers are aligned as on the surface of a sphere and held in place by a hemispherical cage called a planetary. Film growth is monitored across the planetary by quartz crystal microbalances (QCM, *see 2.2.3*) and can fed back to the crucible temperature to maintain constant deposition rates or fed to a shutter system to control overall film thickness.

The crucible is elevated to temperatures essential to achieve evaporation of the specific charge by means of resistive, inductive, or electron beam heating. A coil of wires, wrapped around the crucible, is heated in resistive systems. Here, the filament wire must be elevated to and maintain the same critical temperature as the target to achieve evaporation. This however can create contaminants from the release of gases by the filament wire. Resistive heating is also inadequate at depositing refractory metals as filament wires are unable to achieve the elevated temperatures required by these metals for evaporation.

Inductive heating systems use a boron nitride crucible to house the charge material. Metal coils are wrapped around the crucible. A RF power source is fed through the coils creating eddy currents in the target and thus elevating the temperature. The coils can be water cooled to

temperatures below 100°C, thus eliminating the contaminants created in resistive systems. However, contamination of the charge material by the boron-nitride crucible can occur at elevated temperature.

Alternatively, target material in the crucible can be evaporated by means of electron beams. Fundamentally working in much the same way as EBL systems, e-beam evaporators use focused, high energy electron beams to remove material from the target. But unlike EBL where the target will be the eventual product used, e-beam evaporators are interested in the material removed from the charge for deposition onto wafer elsewhere in the chamber. As seen in Figure 2.4, the electron gun is housed under the crucible and the electron beam is directed toward the charge by a large magnetic field. This arrangement reduces possible contamination of the wafers from electron gun material, especially when thermionic emitters are used. The electron beam can be easily rastered over the target, evaporating small areas and effectively maintaining a nominal temperature across the entire charge. The design of the e-beam evaporators is also well suited for the housing of multiple targets with the ability to switch between the charge evaporated easily achieved. Care must be taken when using e-beam evaporators for any substrate material that may be sensitive to radiation.

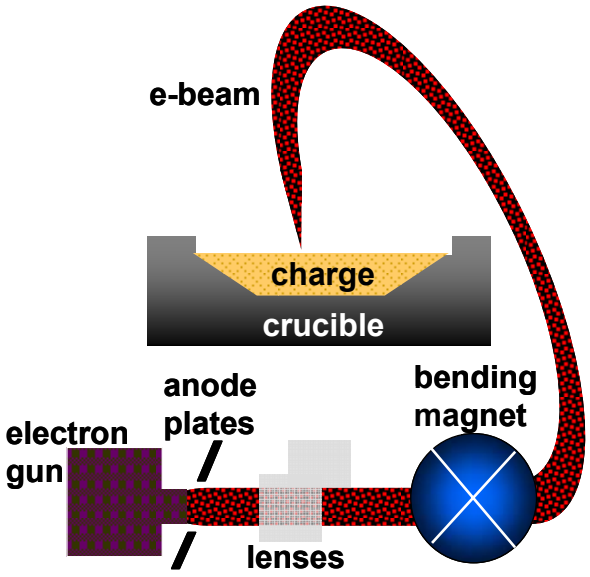

Figure 2.4. Schematic diagram of an electron beam evaporator system.

The biggest problem with the performance of evaporation for depositing thin films is poor to nonexistent step coverage. The low pressure in the chamber causes evaporated material from the charge to travel in straight lines. Film coverage becomes discontinuous on vertical sidewalls. At times a problem, this characteristic of evaporation can also be exploited and used as a future

advantage. Poor step coverage can allow for lift-off procedures to be employed as an alternative to etching steps.

While most metal films are deposited by evaporation or sputtering, rarely are they used for insulating or semiconductor films. Instead a process called chemical vapor deposition (CVD) is used. CVD starts with the introduction of precursor gases into a reaction chamber where the wafer is housed. Products from the reactions migrate to the surface of the wafer where surface reactions pull solids from the gaseous mixture. Gaseous byproducts are desorped from the surface and transported out of the chamber. The gases chosen, their flow rates, and the chemical reactions produced are all process dependant and can vary by the reactor used[40]. CVD can be performed at atmospheric pressure (APCVD), low pressure (LPCVD), or plasma enhanced (PECVD). The earliest process, APCVD is now seldom used say for the deposition of SiO_2 as it is plagued by unwanted particle formation. LPCVD is commonly used in silicon fabrication for the deposition of polysilicon and silicon nitride. LPCVD offers excellent uniformity (< 2% variation) and high throughput. PECVD is used for deposition processes that require low substrate temperatures as in the case of SiO_2 on aluminum or Si_3N_4 onto GaAs.

Sputtering, evaporation and CVD are generally used for the deposition of thin films ranging from 10's to 100's on nanometers in thickness. On occasion however, thick layers of metals and/or alloys are desired for structural stability and use in high throughput replication processes such as injection molding or hot embossing (*see further*). The most common technique used for the deposition of thick layers (≤ 1 cm) is electroplating or electrodeposition (Figure 2.5). The substrate to be plated is connected to the negative lead of a power supply and acts as the cathode. The substrate must be conductive to allow electron transport. Substrates possessing little to no conductivity are typically coated with a thin film of highly conductive metal by means of one of the three techniques mentioned above. The positive lead is connected to a counter electrode (anode) that can be either inert (e.g. Pt) or the metal to be plated. Both electrodes are immersed in an electrolytic solution, hence completing the circuit. The electrolytic solution contains salts of the electroplating metal, highly ionic compounds to aid in electron flow, and acids for buffering capacity. When current is supplied, electrons will flow from the cathode to

the anode. The negative potential at the cathode will attract the metal cations in solution. Once at the substrate the metal cation will be reduced by free electrons at the cathode, falling out of solution and depositing onto the substrate. If a metal source is used as the counter electrode, electron flow through the solution to the anode will oxidize the metal, dissolving it into solution and thus replenishing the electrolytic solution with metal cations. Direct current can be used to power the circuit although a RF power supply is more common. RF power with a known duty cycle coupled with agitation of the solution help to maintain electrode efficiency and homogenize the solution improving the reproducibility and consistency of metal deposition rates. In general, deposition rates are on the order of 10's of microns per hour and are highly dependant upon the current density and electrode efficiencies. A wide range of electrolytic solutions are used based on the metal to be plated with variations in component species and concentrations also playing a role in deposition rates. Furthermore, electrolytic solutions are instrumental in the stress levels of the new metal layer. A wide range of metals are frequently electroplated including: Ni, Cu, Pt, Au, Ag, and Pd with Ni being the most widely used for chip fabrication. Electroforming is a variation of electroplating where a releasing agent is applied to the substrate allowing for the future removal of the metal imprint from the substrate master without any damage to the substrate. These metal imprints are generally used for microchip production that requires stress limits intolerable for the native substrate material. More recently, electroplating has been accomplished without the use of electrodes or external power supplies. Termed electroless plating, this technique relies on

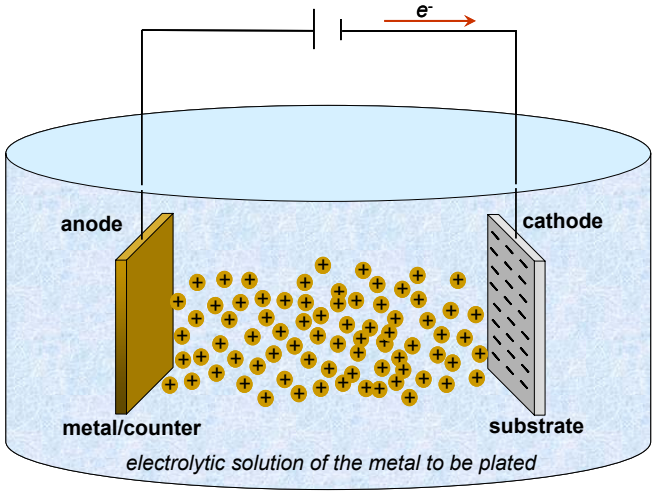

Figure 2.5. In electroplating, metal cations move to the negatively charged substrate and are reduced forming a solid layer of metal on the substrate.

chemical reducing agents where the temperature of the electrolytic solution approaches spontaneous precipitation of the metal cation. The substrate is generally pre-treated to initiate reduction of the metal. Unlike normal electroplating, substituents of the solution are added sequentially. Electroless plating also has very little control over metal deposition rates unlike typical electroplating where the current density can be varied to broadly manage deposition rates.

Spin coating has become one of the most popular additive techniques employed in the processing of research driven or prototypical chip designs. Coupled with photoresist chemistries, the low cost, low operational overhead, and ease of use have made spin coating layers onto substrate material a staple in microfluidics and nanotechnology. In short, spin coating involves application of a photoresist onto a wafer. The wafer is spun for a matter of seconds to evenly distribute the photoresist over the wafer. The spin speed and viscosity of the photoresist determine the thickness of the deposited layer with general applications producing single digit to a few hundred microns tall layers. Spin coated wafers are used in conjunction with photolithography to produce a network of structures across the wafer surface. Exposure from a particular wavelength through a mask typically generated from EBL systems will cause the photoresist material to either initiate decomposition (positive resist) or a crosslinking (negative resist) reaction in areas irradiated. The areas that are decomposed or not crosslinked will be later solubilized in a solvent system and removed from the wafer. The deposited resists can then be used to define etch regions on the wafer, provide sacrificial layers as in lift-off procedures, or be used in cast molding applications where the deposited design is imprinted onto a polymer and latter used as a microchip. A detailed description of spin coating employing a popular negative photoresist (SU-8) and its use in optical and soft lithography is given later (*see 4.1.1*).

Initially, the most common substrate used in the fabrication and development of nanotech devices was Si. Silicon's use was a direct correlation to nanotechnology owing much of its early progress to techniques employed in the IC or semiconductor processing industries. This well documented knowledge of Si microfabrication allowed researchers to develop highly complex fluidic networks for small volume handling with high precision and reproducibility. However, its continued use as the primary material in the composition of nanotech devices would be hindered

by silicon's lack of optical transparency and its brittle nature. The former disadvantage would eventually be overcome by sealing the silicon wafer with a glass cover-plate allowing for optical interrogation of the fluid contained within the channels. However the latter inconvenience is unavoidable and coupled with the high cost of Si wafers and elements of their fabrication process the practicality of nanotech devices made of silicon was drastically reduced.

Glass and glass-like compounds (quartz, fused silica, etc.) quickly replaced native silicon as the leading material used in microchip fabrication. Established surface modifications and well developed processing techniques for glass eased the transition. Glass yielded a much more durable substrate for nanotech devices. The inherent optical and electrical properties of glass were also an advantage over Si devices especially taking into account the expanding employment of lasers/light systems and electric components with microfluidic platforms. The use of fused silica, the amorphous form of silica (SiO_2), added the optical property of ultraviolet (UV) transmission. Thus fused silica became a more attractive and superior substrate material than that of traditional glass. Further manufacturing steps would be added to allow transmission of infrared (IR) wavelengths through fused silica as well. Although many microchips are still made from glass or a related form, fabrication of glass chips is expensive with devices costing upwards of $300 for a single chip. Nanotech devices made of glass are typically fabricated in serial processes reducing throughput. Glass chips are also fabricated using wet etching techniques leaving the final structures with less precision and reproducibility than those made from silicon. A further drawback of using either Si, glass or glass-like materials as microchip substrates is the need for troublesome bonding techniques. Anodic, fusion, and thermal bonding all require high temperatures (300 - 1500°C) often with surface treatments (HF, piranha, etc.) and high pressures.

The use of polymers (plastics) has exploded onto the nanotech scene, filling the void left by the inadequacies of silicon and glass and at times seemingly supplanting their use altogether as the primary material for nanotech devices. Polymers are wonderful substrate materials for nanotech devices since their manufacturing can be tailored to suit different needs. Plastics can be transparent or opaque, conductive or insulating, soft or hard, magnetic, and even piezoelectric

depending on the type of polymer chosen and any additives incorporated into the synthesis. Even surface properties can be easily altered with various chemistries used to either promote (or reduce) adhesion, adsorption, hydrophilicity, and reactivity. Polymeric nanodevices are durable and long lasting, while the low cost of raw materials creates the feasibility for them to be employed as a single use/disposable device. Yet, without doubt, the greatest advantage of using polymers in nanotech fabrication is throughput.

Polymers, specifically thermoplastics, have opened the avenue to high throughput processing techniques such as hot embossing and injection molding. Once a master has been created (by fabrication processes described earlier) hundreds to thousands of devices can be made with little effort in one day. Hot embossing and injection molding fabricate devices in a similar variothermal process. In hot embossing systems a thermoplastic film or substrate is inserted into the molding chamber where the master tool has been mounted on the opposite wall (see Figure 2.6A). Both the master and the polymer are heated to slightly above the glass transition temperature (T_g). The master is then mechanically pressed into the thermoplastic with

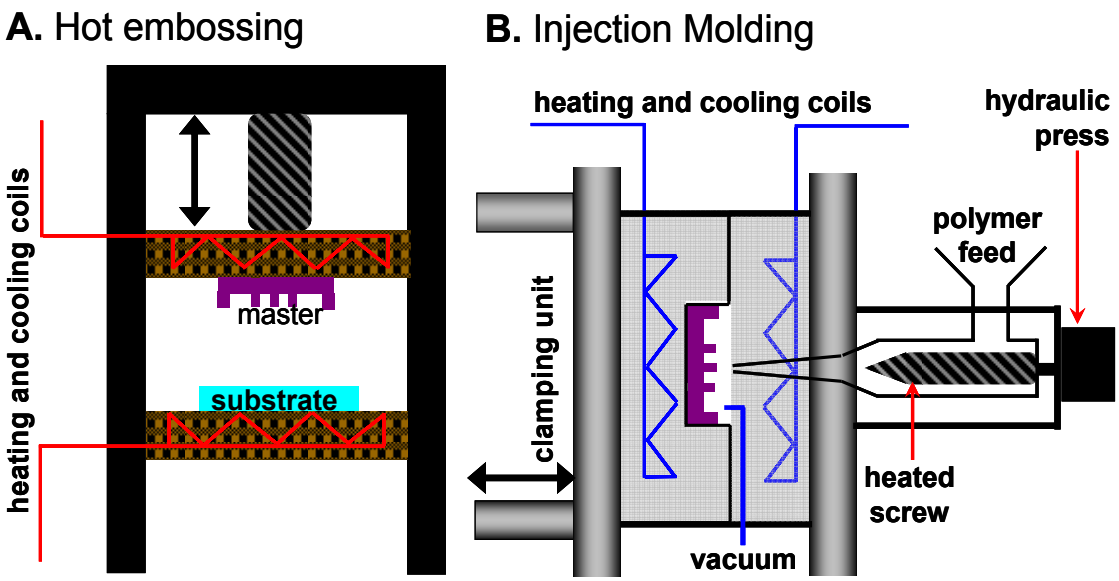

Figure 2.6. Both hot embossing (**A**) and injection molding (**B**) are two common techniques for the rapid production of micro- and nanostructures in polymeric substrates.

a large force (kN) transferring the structural architecture to the polymer. The chamber is then cooled, the master is removed from the plastic, and the newly fabricated polymer device is ejected. In injection molding systems (see Figure 2.6B) the master tool is securely mounted in the mold cavity. This cavity is then closed, evacuated and heated above T_g. Raw polymer (normally in a pellet or granular form) is fed into a chamber adjacent to the mold cavity. The granules are heated above T_g and mixed generally with a heated screw. The viscous polymer is injected into the cavity forming in and around relief structure of the master. The thermoplastic is then cooled below its glass transition temperature thus solidifying. Finally the cavity is opened, the polymer is demolded from the master tool and ejected from the cavity. There are certain trade-offs for using either technique. Hot embossing has a longer cycle time (ca. 5 min.) and thus lower throughput to range of a few hundred devices a day. Comparatively, injection molding systems allow for high levels of automation reducing cycle times to the order of seconds. The high throughput of injection molding is its greatest advantage with ability to produce thousands of thermoplastic devices a day. Stress on the master tool and the final polymer device however are reduced in hot embossing by shorter polymer flow and smaller temperature cycles with the latter also reducing device shrinkage. This allows for small structures with high aspects to be produced by hot embossing with higher precision.

Yet even newer materials have been sought in the fabrication of nanotech devices. Focused research has been given to devices that are used with cells and tissue samples where biocompatibility can be an issue. To this end, researchers have begun to develop new fabrication techniques employing biomaterials with hydogels[41, 42], gelatin crosslinked enzymes[43], and biodegradable polymers[44] among the most notable. Attempts at creating stronger and more resistant devices have also come to the forefront with the development of a solvent resistant, photocurable material termed ‘liquid Teflon’ showing excellent promise.[45]

Still, a highly cost effective material was introduced in the late 1990’s that today has become a workhorse in microfluidic and nanotech research and development. Poly(dimethylsiloxane), commonly known as PDMS, is an elastomer (i.e. elastic polymer) consisting of a Si-O backbone and CH_3 side chains. Known for its low modulus, PDMS

fabrication in soft lithography techniques allows for the rapid prototyping of diverse and intricate structures. As PDMS was the material used for fabrication of most devices used in this paper, its properties and soft lithography itself are discussed later in detail (*see 4.1*).

2.1.3 *Applications and μ-TAS*

The integration of microfluidics and nanotechnology has led to an immense number of applications in a wide range of scientific fields. As stated earlier, the first real push to miniaturize applications came from separation scientists. In 1979 Terry *et.al*[46] reduced a complete gas chromatographic (GC) instrument onto a 5 cm diameter silicon wafer separating nitrogen, pentane, and hexane in under 5 seconds. Scientists knew that a reduction in the size of the separation channel would not only decrease retention times of analytes in the columns but also increase efficiency. Hence, since Terry *et.al*[46] led the way with their on-chip GC and influx of separation designs have been implemented in the nanotech field. On-chip electrophoresis is the most widely used technique.[47, 48] Integrated injectors along with electroosmotic flow (EOF) can produce well defined, short sample plugs that traverse the channel with little diffusion and thus increase separation efficiency. These systems can be used for the rapid separation of complex mixtures, be it DNA, amino acids, proteins, etc., in very small volumes (ca. nL). Because of the applied voltages to small channels, Joule heating is a concern in on-chip electrophoresis and must be a consideration in experimental design. Although less frequently used, μ-HPLC (high performance liquid chromatography) is another separation technique that has found acceptance in nanotechnology. Widely applicable, stationary columns packed in the microfluidic network can be designed to adsorb and retain almost any analyte.[49] The general drawbacks of μ-HPLC are the added design requirements for pumps to control fluid flow and frits or weirs for column packing. Diffusive spreading of the injected plug is also of concern since most μ-HPLC systems are pressure driven.

As mentioned earlier, one of the most prominent applications is drug delivery. Microfluidic devices can also be used during the drug development process in a high throughput screening format testing receptor affinities and drug toxicities. Small molecule libraries can also

be founded using microchips for the possible use as markers of specific diseased states. Nanotech devices also have great potential use in point-of-care detection. Here small volumes of biological samples can be processed in a clinical facility for the monitoring of specific markers of diseased states, diagnostic recognition, or prognostic pathways.

Cell studies have also become a hot topic in nanotechnology. Cell sorting in microfluidic channels allows for the manipulation and interrogation of single cells, a reductionist approach to the study of biology. Single cell analyses can be performed for cell activation, protein expression, intra- or intercellular signaling as well as the monitoring of toxins in biodefense. Cell motility is also studied with particular interest being given to chemotaxis, haptotaxis, and any cell signaling pathways that may be responsible or influence movement. Measurement of the forces associated with cell to cell adhesion is extremely important as recent results have shown that a loss of this adhesion can be a cause for metastasis.[50] Bioreactors are also being developed on-chip with the capability of culturing cells, tissue, etc.

Other applications have less biological relevance but are none the less important to scientific discovery. Both serial and parallel chemical syntheses have been performed in microchips drastically reducing the amount of reagents needed and thus the cost of exploratory or combinatorial chemistry. Excellent results have been published by Anderson *et.al*[51] to screen multiple chemical and environmental conditions in a nanodevice to greatly improve the crystallization of proteins. Microchips have been used to sample soil, water, and gas for environmental monitoring.

The achievement of performing an entire experiment on-chip, termed micro total analysis systems (μ-TAS), is credited to Widmer and Manz[52] (even though Terry achieved this first in 1979). Their notion was simple: miniaturize all processes required for a complete analysis and perform them in a microfluidic device. These labs-on-a-chip sample solutions, transport fluids, derivatize the sample, separate species, react or stimulate the analyte, detect signals or responses, and finally collect waste. Not simply an application, μ-TAS are a technology/field where many different applications may be applied. Among other benefits, μ-TAS allow for complete automation of processes, voiding operator error and decreasing analysis time. For a

more comprehensive look at the recent growth of μ-TAS in scientific fields, readers are urged to look here.[53, 54]

Applications involving bioassays in a microfluidic format are a primary focus of the research conducted in this dissertation. Determination of affinity and thermodynamic stability by means of equilibrium binding constants and analysis of reaction kinetics are among the most important measurements in biological systems including the study of macromolecule-ligand binding, protein-protein interaction or enzymatic transformations. The most common detection schemes used to study these interactions on-chip are presented below. Current limitations are discussed and a possible alternative is presented.

2.2 Detection Methodologies used in Nanotechnology

Two of the most common problems to plague nanotech devices are fluidic interfacing with the macro world and applicable analyte detection methods. Complications in fluidic manipulation arose in part from the coupling of microchips to classical bench-top instruments with large sample volumes and undesirable flow rates. Incorporation of miniaturized techniques into nanotech devices for sample pretreatment or manipulation, as in μ-TAS systems, has reduced the need for macro world interfaces and thus some of the problems for fluidic manipulation.[53-56] Advances in fabrication techniques have also been of great benefit to microchips with the advent of pumps and valves contained within the actual device increasing the operational control over fluidic manipulation.[57] Although fluidic interfacing and manipulation is still of extreme importance, this paper focuses more on the limitations of current detection methods used in nanotechnology and a possible solution.

2.2.1 *Optical Detection*

Optical detections systems are prevalent in nanotech devices. The lack of a truly physical interaction with the sample, the broad range of available sources with physical dimensions on par with microchips, ease of focusing and path guidance as well as no need for a

direct interface to the chip make optical systems practical detectors for use in nanotech devices. Most approaches for μscale detection have been based on "conventional" optical measurements, primarily absorption or fluorescence. However, absorbance is governed by Beer's Law limiting its use in chip-scale techniques because of its inherent pathlength sensitivity.[58, 59] The small channel dimensions in microchips (ca. 20 - 100μM) exacerbate the signal-to-noise (S/N) limitation for absorbance determinations generally relegating its use to that of a colorimetric detector.[60] Various researchers have tried to overcome the pathlength dependence of absorbance by manipulating the optical train through microfluidic devices or by longitudinal beam introduction parallel to the channel geometry. Mogensen *et.al*[61] created a U-bend in the fluidic network with waveguides positioned on each end of the elbow for illumination and detection. The detection channel was thus extended to a length of 1 mm and even then their reported detection limits for acetaminophen was 19.8μM. Salimi-Moosavi *et.al*[62] were able to circumvent dramatically altering the fluidic network by depositing aluminum mirrors on opposite sides of the flow cell. Illumination perpendicular to the channel was reflected multiple times increasing the optical path and consequently improving the sensitivity compared to single-pass systems by a factor of ten.

The most widely used optical system in microfluidic devices is fluorescence, specifically laser-induced fluorescence. The unique properties of lasers such as high spatial coherence, monochromaticity, and high photon flux, help to offer superb sensitivity (as few as 10^5 molecules) and selectivity in biochemical analyses.[63, 64] In fact, recent developments in ultra-high sensitivity LIF have allowed single molecule detection to be performed 'on-chip'.[65] While fluorescence is an inherently sensitive detection method, the optics required can be expensive with many researchers simply incorporating the microfluidic devices onto the stage of a pre-existing fluorescent microscope. This in turn limits the versatility and prohibits the portability of the nanotech device. Even more troublesome is the need to chemically modify (derivatize) most analytes of interest. Derivatization can perturb the native state of the molecule, possibly affecting structure and reactivity. Chemical modification at some sites can in fact greatly reduce or at times completely inhibit the expression of proteins. Furthermore, some molecules lack the substructures needed for derivatization to even occur. In this case, directed mutagenesis must

be undertaken to provide the needed substructures, altering the analyte's native state even prior to fluorescent derivatization. Thus fluorescent measurements may provide slightly altered or even erroneous values during kinetic and thermodynamic assays. Preliminary data shown here further suggests that derivatization may substantially affect these measurements, giving erroneous binding constant values.

2.2.2 *Electrochemical Detection*

Electrochemical detection is a less expensive alternative to optical systems without much loss in sensitivity. Fabrication steps often used to manufacture the microchip are also processes capable of depositing metals (or in this case planar electrodes). Therefore electrode deposition and integration into the final structure can be accomplished by 1-2 more fabrication steps, much simpler than integrative optics. Initially, most electrochemical detectors used electrodes in a direct contact, end-column arrangement for on-chip electrophoresis. An even more ideal scenario for electrochemical detection came about with the reductionist approach to monitoring single cells in a microfluidic format. Electrodes can be easily fabricated on the same size scale as that of single cells. This miniaturization also increases electrode sensitivity by reducing the effective volume, increasing the surface area to volume ratio. Furthermore, electrodes are well suited for monitoring cellular metabolic activity as they are commonly employed as pH, concentration, O_2, and various cation/anion sensors. Electrochemical detection has found widespread acceptance in single cell analysis including the detection of catecholamines from PC 12 cells[66], lactate production by heart cells[67], and biopotentials produced by a single cardiac myocyte[68].

Recently, solid state field effect transistors (FET) have shown promise for the electrochemical detection of biochemical assays.[69] Boron-doped silicon nanowires (NW) were used as pH dependant conductance sensors to monitor surface changes real-time. Through chemical modification and functionalization of the SiNW, picomolar concentrations of streptavidin were detected as well as the determination of equilibrium dissociation constants for anti-

biotin/biotin and calmodulin/Ca^{2+} systems.[70] Lieber *et.al*[71] also reported PNA-DNA hybridization using surface modified SiNW's immobilized with DNA.

Though extremely sensitive and widely applicable, potential pitfalls do exist with the use of electrochemical detection. The use of high voltages increases Joule heating in microfluidic devices and can shift redox potentials for analytes.[72] While fabrication of electrodes incorporated into nanotech devices may be straight forward, the potential for fouling is always a concern and can limit the lifetime of the device. Electrochemical detection in single cell analyses may have detrimental effects on the cell itself by consumption of O_2 or local pH changes during oxidation/reduction process. Lastly, immobilization procedures can degrade and typically lack homogeneity resulting in electrode-to-electrode and chip-to-chip variability or results.

2.2.3 *Quartz Crystal Microbalance*

The quartz crystal microbalance (QCM) is an acoustic wave sensor highly sensitive to minute changes in mass at the crystal surface.[73, 74] QCM is comprised of a quartz disc with a small diameter (ca. 0.5 – 1mm) sandwiched between two smaller electrodes (Fig. 2.7). QCM is dependant upon a converse-piezoelectric effect where an applied voltage induces a strain on the crystal. An electric field produced by an alternating current source applied across the two electrodes couples to oscillations in the quartz. The quartz will begin to resonant at a fundamental frequency. Changes in this frequency was shown to have a linear response to mass deposited on the crystal surface by Sauerbrey.[75] The mass sensitivity of the sensor is proportional to the square of the resonant frequency (f_0^2) of the crystal. The resonance frequency in turn is inversely proportional to twice the thickness of the crystal. Therefore the thinner the quartz crystal the more sensitive the device.

As stated earlier (*see 2.1.2*), QCM is often used to monitor the deposition of thin films in evaporation processes. While extremely well suited for detection of small mass changes under vacuum or in a gaseous environment, QCM has been recently shown to work well in a liquid surrounding particularly in biochemical assays. Since the electrodes used in QCM devices are typically gold, they can be functionalized with biomolecules of interest frequently with self-

assembled monolayers (SAM's)[76-79] although other methods may be used.[80-83] Any binding to the immobilized particles adds mass to the electrode/quartz and is detected by a change in frequency. QCM devices setup in this manner have been used to quantify proteins in urine samples[84], study cell structure and attachment[85], as well as to screen for drug response[86]. The coupling of QCM with nanoparticles, particularly monolayer-protected clusters (MPC), has shown great promise in epitope mapping and immunoassays. The 3-D structure of MPC's allow for peptide epitopes to be immobilized while keeping secondary structure.[87] The ability to account for the local conformation is a great advantage and can be essential for antibody recognition.

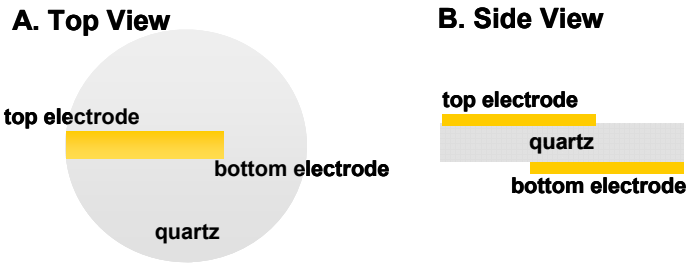

Figure 2.7. Shown here is a representation of the top view (**A**) and side view (**B**) of a quartz crystal microbalance device (QCM).

QCM is a highly sensitive technique for the detection of bioassays. There are however limitations that must be taken into account. The density and viscosity of the liquid used affects the crystal frequency. Therefore tedious calibration curves of solutions that will not adsorb onto the electrode surface must be performed to decouple mass loading from liquid loading. QCM devices also rely on immobilization chemistries that can be expensive and deteriorate over time. The immobilization of a molecule can also alter binding data and may not accurately represent the natural physiological environment. QCM also relies on an evanescent wave that decreases in amplitude as it moves further away from the electrode surface and into the liquid media. A 5MHz quartz crystal has a calculated penetration depth of 250nm with some experimental observations showing no decrease in sensitivity at depths of 400nm.[88] Still, combined with the need for immobilization chemistries, the effective detection volume is limited with overall sensitivity diminishing the further one moves away from the electrode surface.

2.2.4 *Refractive Index Detection*

Refractive index (RI) is a universally applicable, non-invasive, non-destructive and highly sensitive technique capable of label-free detection. RI detection is most commonly used in conjunction with HPLC for the measurement of eluates from separation columns. The optical properties of various materials (e.g. lenses, prisms, etc.) including flatness and dispersion are also typically measured with refractive index techniques. However, the recent implementation of RI detectors into nanoscale devices demonstrates potential for their greater use in the study of label-free interactions in a noninvasive and nondestructive manner.

Porous Silicon

Sailor and co-workers have shown a porous silicon detector (PSi) can be used to study reversible protein–protein binding interactions and DNA hybridization reactions[89-91] by changes in RI. In PSI, the porous Si is illuminated with a broadband source from the top producing a fringe pattern. A shift in wavelength is manifested by local changes in the refractive index near the porous Si surface and can be detected by interrogation of the fringe pattern. The technique has been demonstrated to detect changes in the mass of immobilized protein and DNA far above the sensor's surface[90, 91] with good performance and reasonable detection limits. Diffusion rates for larger molecules where no active mixing is employed is a major limitation of PSi with reaction times on the order of 100 minutes for IgG. Long sensor surface preparation times (ca. 7 hours) are also problematic, restricting the primary use of this sensor to static measurements. It is noteworthy that the PSi sensor has not been used effectively for rapid analyses or in flowing streams.[90]

Surface Plasmon Resonance

Another RI sensing technique, Surface Plasmon Resonance (SPR), is the most widely employed detection method in microarrays for the study of label-free interactions on immobilized substrates.[92, 93] SPR relies on the excitation of surface plasmons (i.e. oscillation of free electrons) at the interface between a metallic layer and a dielectric media where. In a typical SPR setup (Figure 2.8), p-polarized light impinges upon the metal layer at an angle greater than the critical angle.[94] The spectrum of reflected light from the metal surface exhibits a strong attenuation in

intensity at a resonance angle. This minimum is due to the coupling of the incident light with the surface plasmons. Here the energy is absorbed by the surface plasmons and is not reflected. Excitation and then oscillations of the electrons create a restricted electromagnetic field that propagates into the dielectric media. This evanescent wave decays exponentially as it moves away from the metal/fluid interface, limiting SPR detection. The angle of minimum intensity in the reflected spectrum is dependant upon the local refractive index near the metal/fluid interface. Thus SPR can detect any change to the metal surface whether that be desired immobilization or binding as well as unwanted non-specific adsorption.

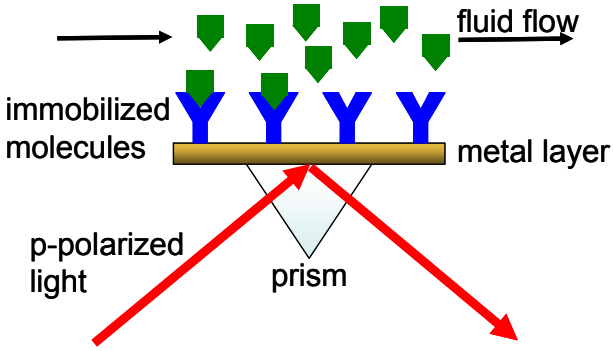

Figure 2.8. Diagram of a surface plasmon resonance (SPR) sensor.

Gold is the most prominent metal used in SPR systems, and just as in QCM, molecules of interest are immobilized onto the gold surface. However, the elaborate surface chemistry used to immobilize targets on SPR surfaces has been shown to lose as much as 20% of binding capacity over a 24 hour period.[95] The immobilized molecules are interrogated by a solution passing over the gold surface. A change in the local RI at the metallic interface occurs in adsorption or reactions take place. SPR detects this change as either an attenuation of reflected light (fixed incident angle) or a change in resonance position as a function of incident angle. Several techniques have been developed to increase the signal-to-noise ratio of SPR. For instance, addition of metallic or colloidal particles to the analyte solution[96, 97] have been used but such techniques are undesirable when a truly non-invasive analysis is required. SPR has been implemented in an array format[98-100] and as a portable device[101], significantly improving its practical utility. A dual wavelength SPR sensor has also been employed to increase the overall detection limit of the technique to 4.5×10^{-6} RIU (refractive index units).[102] PDMS has also recently been used to prepare microarrays for sample introduction into the SPR[103, 104] device,

however complete integration and multitasking is limited. Yet for all the improvements, SPR still requires elaborate surface chemistry[105], metal deposition onto substrates (problematic for plastics), and high quality optics for surface illumination [98, 106, 107].

Interferometry

The robust and copious use of interferometry can be found scattered throughout the scientific community. Optical coherence tomography (OCT) relies on interferometry to monitor vascular pathology and noninvasive biopsy. The use of interferometry in astronomical telescopes has helped produce the highest resolved images ever in space exploration. The simple nature of monitoring the interference of coherent waves is widely applicable to a variety of techniques.

More recently interferometric systems have been used as label-free detectors in microfluidic devices. Interferometry has been successful at detecting DNA hybridization of a 58 nucleotide base strand to an immobilized 28 base strand with a 300 pM detection limit.[108] Another configuration allowed for the determination of diffusion coefficients and flow injection analysis over a dynamic range of 106 – 22800 Da. Other interferometric setups have been employed for the analysis of pollutants as well as protein interactions.[109-112] However the use of these interferometric techniques in molecular interactions was performed using surface immobilized analytes with sensitivity again limited as a function of distance from the surface. The sensitivity of these methods is also limited by their single pass nature. Furthermore, integration of waveguides into the microchip was generally needed increasing fabrication times and reducing device throughput.

Only the most common sensing techniques used in microfluidics and nanotechnology are presented above. Many other detection methodologies exist for use in nanotech devices although most are niche techniques. For a review of some of these other techniques readers are encouraged to look elsewhere[2, 69, 113-116].

2.3 Backscattering Interferometry

Molecular interactions are central to understanding basic cellular function and for evaluating therapeutics.[117] However, as seen above, the tools available to quantify these interactions *without* modifying the analyte is severely limited. The detection methods mentioned previously (*see 2.2*) require either the surface immobilization of a specific biomolecule or the attachment of a signaling moiety, both of which can influence molecular interactions. Investigations of molecular interactions are ideally performed in a label-free format as stated previously (*see 2.2.1*). It is also desirable to eliminate the need for the surface chemistry normally used in binding assays. Immobilization of biomolecules present persistent problems including: altered kinetics due to surface bound targets, reduced surface activity (and thus reactivity) over time, increased costs, increased non-specific binding, and difficulty in quantification of the immobilized species. The ability to perform pure liquid–phase molecular binding analyses in a μ-TAS format would eliminate many of the problems that arise from the surface chemistry, while facilitating small volume samples to be studied. Investigations presented here demonstrate molecular interactions can be studied in the absence of these perturbations, at high sensitivity, in picoliter volumes and in free-solution using backscattering interferometer (BI).

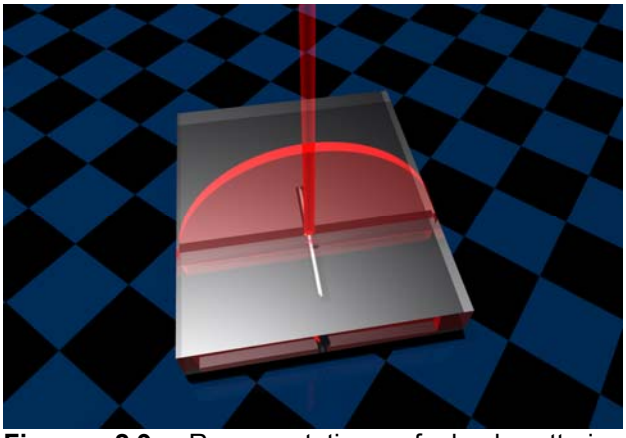

Figure 2.9. Representation of backscattering interferometry (BI) with incident light impinging a microchip and a fanned interference pattern produced perpendicular to the direction of the flow cell.

2.3.1 *Experimental Background and Setup*

Unlike other detection methods reviewed previously, BI can be used to monitor label-free molecular interactions in very small volumes by either a bulk or surface sensing mode. BI relies on the interference of light waves detected in a backscattered direction from a microfluidic flow cell (e.g. capillaries, glass or polymeric flow chips, etc.) to monitor changes in refractive index. Incident light waves experience reflection, refraction, and diffraction during propagation through the microchip. Both the surface and fluid within the microchannel are interrogated several times by numerous passes of light. This multi-pass aspect of BI greatly increases sensitivity to changes in the optical pathlength incurred by any variations to the media or channel structure.

Since BI is a RI detector, the system is universally applicable (*see 2.3.3*). This interferometric sensor is also non-destructive and noninvasive. BI is well suited for microscale detection and is amendable to almost any transparent substrate. The low cost of the instrument is a plus as is its capability to function in a high-throughput manner. And as opposed to other optical sensing systems, BI employs a simple optical train (Figure 2.9). Numerous embodiments of the system have been used but all with the same basic components: a coherent light source, a small flow cell, and a phototransducer. Coherent light is directed onto the flow cell containing the solution to be analyzed. Interaction of the light with a fluid filled flow cell produces a high contrast interference pattern fanning orthogonally from the direction of the flow cell. A part of this interference pattern is detected by a phototransducer in the backscattered direction for analysis. It is of extreme importance to note that the entire optics of the interferometer is the microchip itself. Thus any changes or alterations to the flow cell/microchip will play a critical role in the performance of the BI system.

2.3.2 *Interference Pattern*

The interference fringes produced are highly sensitive to and shift spatially with changes in the optical pathlength/RI. This phenomenon has been studied and verified by simulations of the light propagation through the BI system using multiple modeling techniques.[118-123] The resolution between constructive interference and destructive interference is very high with a

contrast ratio of 0.999 demonstrating high finesse interference. The high resolution is critical to BI's superior sensitivity considering detection is based upon spatial shifts of the interference fringes.

2.3.3 *Early Applications*

In early embodiments of BI, a capillary was used as the flow cell. With inner capillary diameters ranging from 100 – 360 μm coupled to unconditioned laser spot sizes, detection volumes in these embodiments were on the order of nanoliters. The capillary system was generally used for miniaturizing separation sciences. Chromatography and electrophoresis strive to drastically reduce sample consumption and increase separation efficiency. BI has been used towards this purpose separating small alkali cations[124], dyes[125], carbohydrates[125], and analyzing caffeine in drinks[121] by capillary electrophoresis with femtomole mass detection limits. The capillary embodiment was also used for μ-HPLC[126] separations, flow injection analysis[118], and micro-degree (°C) thermometry[118]. It was also shown that BI could be used in conjunction with a capillary as a polarimeter (Figure 2.10), capable of quantifying micro-degrees of optical rotation for low concentrations (μM) of racemers in nanoliter volumes.[121, 127-130] Swinney *et.al*[120] further demonstrated the functionality of the BI polarimeter, monitoring the enzymatic conversion of β–hydroxybutyrate (an indicator of ketoacidosis) to acetoacetate by β–hydroxybutyrate dehyrdogenase (BHD).

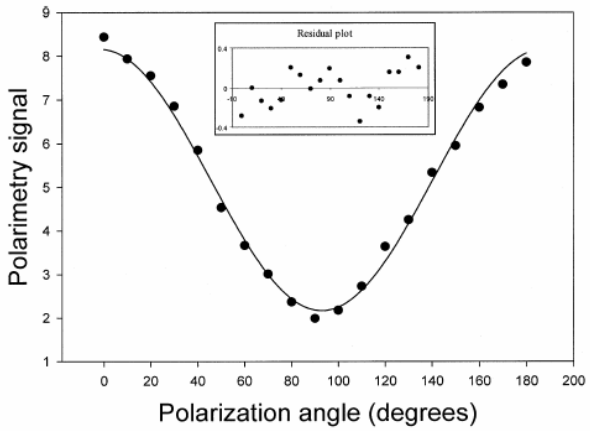

Figure 2.10. Polarimetry signal obtained from the Fourier analysis. Solid dots = experimental data; solid curve = $\cos^2$ fit with R^2 = 0.993.

While easy to use and producing exceptionally high resolution fringes, capillaries offer little versatility in design, reducing effectiveness and potential in various applications. Capillaries

are also limited in size, geometry, and become brittle over time. The transfer of microelectronic fabrication techniques to the physical sciences and engineering programs created the ability to produce microchips capable of advanced fluidic networks effectively replacing capillaries[8]. Microchips allow for the vast integration of fluids and processes, high parallelization, reduction in size, and the potential for total systems analysis (i.e. μ-TAS or lab-on-a-chip).[52, 53] The inherent small size of working with microchips allow for studies to be performed with minute amounts of material, at drastically reduced costs, and in much faster analysis times.

Fluidic networks etched in fused silica were the first microchips used in combination with BI. The use of the fused silica chips immediately reduced detection volumes to the picoliter regime. Many of the applications previously accomplished with capillaries were again performed in the fused silica microchips. Among these, the most notable was electrophoretic separation. Wang *et.al*[131] used a pinched injection to introduce five un-derivatized proteins, ranging in size from 9 kDa to 66 kDa, into a separation channel. The mixture was separated and detected label-free with excellent resolution (139,400 N/m for calmodulin to 660,000 N/m for BSA) in fewer than 150sec (Fig. 2.11). Injected concentration detection limits for egg albumin ranging from 38 nM (peak area) to 150 nM (peak height) corresponding to a mass detection limit of just 11 attomoles (0.52 pg). In comparison, the detection limit for the on-chip electrophoretic separation of five proteins employing post column labeling and detection by laser-induced fluorescence was reported to be less than ~30 amol (0.5 pg) for injected amounts of α-lactalbumin.[132] It is noteworthy that these results were obtained without low-pass signal filtering or any active temperature control, a worst-case situation for on-chip CE with RI detection.

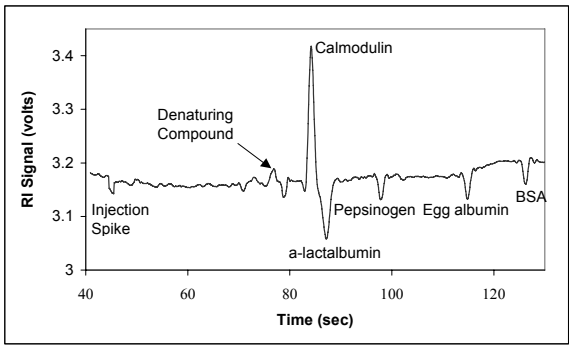

Figure 2.11. Typical on-chip electropherogram of 5 proteins produced by BI detector.

Another important realization of BI in fused silica chips was the noninvasive measurement of flow rates. Since many of the current applications for microchips involve separation sciences this area is of extreme importance. As described by the Van Deemter equation, small changes in the flow rate play a crucial role in separation efficiency. To this end BI was used to quantify small flow rate changes in microfluidic chips. Markov *et.al*[133] used an infrared laser with a mechanical shutter to heat a section of a flowing volume in a fused silica chip. The resulting change in RI induced by the heated plug was detected by BI downstream in a time-dependent manner. Fluid velocity was quantified as changes in the phase difference between the shutter signal and the BI signal in the Fourier domain. The experiments were performed with flow rates in the range of 50 – 100 nL/min with 3σ detection limits determined to be 0.127 nL/s. At the time reported, this was the lowest noninvasive, nonobstructive flow measurements ever performed on-chip in such small volumes (300 pL).

While offering increased functionality with the same sensitivity as capillaries, the use of fused silica microchips suffer from difficult fabrication and annealing techniques. Furthermore, these time consuming production steps are generally serial processes reducing throughput and driving up costs. To combat the soaring costs and low yields associated with fabricated microchips in semiconductor/silica materials, a push was made to produce microchips in polymer and elasotmeric substrates.[134] Polymers offer a wide range of chemical, optical, and electrical properties that can be fabricated in a high throughput formats such as injection molding or hot embossing.[135, 136] As polymers provided the much needed improvement for quick, cost effective production of finalized microchip designs, the advent of soft lithography did the same for prototypical design and research.[137, 138] In particular, the use of poly(dimethysiloxane), PDMS, in combination with conventional photolithography and cast molding allow researchers to design new fluidic networks and fabricate the prototype microchip in one day at very low costs.[139, 140] PDMS is an optically transparent elastomer capable of surface modification. PDMS is also gas permeable making microchips fabricated in the material amendable to cell assays.

BI was previously used with microchips fabricated in PDMS for biomolecular assays in a surface bound format. Initial attempts at using PDMS chips focused on immobilizing proteins

onto channel surfaces in the fluidic network. Once immobilized, various concentrations of ligand were introduced into the channel serially and allowed to react. Binding was monitored by BI for each successive concentration of ligand. Early work by Markov *et.al*[141] experimented with using multiple layers (lysine/glutaraldehyde/streptavidin/ethanolamine) to immobilize molecules onto the PDMS surface. This was accomplished with high sensitivity, as biotin and IgG were both detected at femtomole mass limits.

The three primary foci presented here help to further these previous findings while investigating the theory and methodology of the BI system. It is of extreme importance to note that the entire optics of the interferometer is the microchip itself. Thus any changes or alterations to the media/flow cell/microchip will play a critical role in the performance of the BI system. It is this fact that has guided the modeling of light propagation through various chip designs (*Chapter III*). Simulations of the light propagation through BI give insight into the inner workings of the technique and allows for possible optimization of system parameters. Chip design/fabrication *(Chapter IV)*, guided by the findings from simulations, increase the versatility and overall potential of the BI system. Lastly, physiologically relevant applications examine the efficacy of this sensing technique for studying molecular interactions *(Chapter V)*. Advances from previous studies will be discussed and an overall evaluation of BI to perform these experiments without the need for fluorescent or radioactive labels, in picoliter volumes, at high sensitivity (attomoles) and in a fully integrated microfluidic format will be given.

(1) Roco, M. C. *Current Opinion in Biotechnology* **2003**, *14*, 337-346.

(2) Jianrong, C.; Yuqing, M.; Nongyue, H.; Xiaohua, W.; Sijiao, L. *Biotechnol Adv* **2004**, *22*, 505-518.

(3) Ferrari, M. *Nat Rev Cancer* **2005**, *5*, 161-171.

(4) Whitesides, G. M. *Nat Biotechnol* **2003**, *21*, 1161-1165.

(5) Prokop, A.; Prokop, Z.; Schaffer, D.; Kozlov, E.; Wikswo, J.; Cliffel, D.; Baudenbacher, F. *Biomed Microdevices* **2004**, *6*, 325-339.

(6) Whitesides, G. M. *Nature* **2006**, *442*, 368-373.

(7) Wikswo, J. P.; Prokop, A.; Baudenbacher, F.; Cliffel, D.; Csukas, B.; Velkovsky, M. *IEE Proc Nanobiotechnol* **2006**, *153*, 81-101.

(8) Verpoorte, E.; De Rooij, N. F. *Proceedings of the Ieee* **2003**, *91*, 930-953.

(9) LaVan, D. A.; McGuire, T.; Langer, R. *Nat Biotechnol* **2003**, *21*, 1184-1191.

(10) Madou, M. *Anal Bioanal Chem* **2006**, *384*, 4-6.

(11) Bornhop, D. J.; Contag, C. H.; Licha, K.; Murphy, C. J. *Journal of Biomedical Optics* **2001**, *6*, 106-110.

(12) Manning, H. C.; Goebel, T.; Thompson, R. C.; Price, R. R.; Lee, H.; Bornhop, D. J. *Bioconjugate Chemistry* **2004**, *15*, 1488-1495.

(13) Collins, I.; Workman, P. *Nature Chemical Biology* **2006**, *2*, 689-700.

(14) Brigger, I.; Dubernet, C.; Couvreur, P. *Advanced Drug Delivery Reviews* **2002**, *54*, 631-651.

(15) Iwasaki, Y.; Ueda, M.; Yamada, T.; Kondo, A.; Seno, M.; Tanizawa, K.; Kuroda, S.; Sakamoto, M.; Kitajima, M. *Cancer Gene Therapy* **2007**, *14*, 74-81.

(16) Hughes, G. A. *Dm Disease-a-Month* **2005**, *51*, 342-361.

(17) Sahoo, S. K.; Labhasetwar, V. *Drug Discovery Today* **2003**, *8*, 1112-1120.

(18) Warnement, M. R.; Faley, S. L.; Wikswo, J. P.; Rosenthal, S. J. *Ieee Transactions on Nanobioscience* **2006**, *5*, 268-272.

(19) Euliss, L. E.; DuPont, J. A.; Gratton, S.; DeSimone, J. *Chemical Society Reviews* **2006**, *35*, 1095-1104.

(20) Moghimi, S. M.; Hunter, A. C.; Murray, J. C. *Pharmacological Reviews* **2001**, *53*, 283-318.

(21) Gref, R.; Minamitake, Y.; Peracchia, M. T.; Trubetskoy, V.; Torchilin, V.; Langer, R. *Science* **1994**, *263*, 1600-1603.

(22) Kar, S.; Chaudhuri, S. *Synthesis and Reactivity in Inorganic Metal-Organic and Nano-Metal Chemistry* **2006**, *36*, 289-312.

(23) Bowers, M. J.; McBride, J. R.; Rosenthal, S. J. *Journal of the American Chemical Society* **2005**, *127*, 15378-15379.

(24) Samatham, R.; Park, I. S.; Kim, K. J.; Nam, J. D.; Whisman, N.; Adams, J. *Smart Materials & Structures* **2006**, *15*, N152-N156.

(25) Goldstein, J.; Newbury, D.; Joy, D.; Lyman, C.; Echlin, P.; Lifshin, E.; Sawyer, L.; Michael, J. *Scanning Electron Microscopy and X-ray Microanalysis*, Third ed.; Kluwer Academic/Plenum Publishers: New York, 2003.

(26) Vladimirsky, Y.; Bourdillon, A.; Vladimirsky, O.; Jiang, W.; Leonard, Q. *Journal of Physics D-Applied Physics* **1999**, *32*, L114-L118.

(27) *Experimental Methods in the Physical Sciences*; Academic Press: San Diego, CA, 1998.

(28) Joglekar, A. P.; Liu, H.; Spooner, G. J.; Meyhofer, E.; Mourou, G.; Hunt, A. J. *Applied Physics B-Lasers and Optics* **2003**, *77*, 25-30.

(29) Joglekar, A. P.; Liu, H. H.; Meyhofer, E.; Mourou, G.; Hunt, A. J. *Proceedings of the National Academy of Sciences of the United States of America* **2004**, *101*, 5856-5861.

(30) Malek, C. G. K. *Analytical and Bioanalytical Chemistry* **2006**, *385*, 1351-1361.

(31) Malek, C. G. K. *Analytical and Bioanalytical Chemistry* **2006**, *385*, 1362-1369.

(32) Sugioka, K.; Cheng, Y.; Midorikawa, K. *Journal of Photopolymer Science and Technology* **2004**, *17*, 397-402.

(33) Sugioka, K.; Masuda, M.; Hongo, T.; Cheng, Y.; Shihoyama, K.; Midorikawa, K. *Applied Physics a-Materials Science & Processing* **2004**, *79*, 815-817.

(34) Williams, K.; Muller, R. *Journal of Microelectromechanical Systems* **1996**, *5*, 256-269.

(35) Campbell, S. *The Science and Engineering of Microelectronic Fabrication*; Oxford University Press: New York, 1996.

(36) Kovacs, G. *Micromachined Transducers SOURCEBOOK*; McGraw-Hill: New York, 1998.

(37) Williams, K.; Gupta, K.; Wasilik, M. *Journal of Microelectromechanical Systems* **2003**, *12*, 761-778.

(38) Koenig, H. R.; Maissel, L. I. *Ibm Journal of Research and Development* **1970**, *14*, 168-&.

(39) Horwitz, C. M. *Journal of Vacuum Science & Technology a-Vacuum Surfaces and Films* **1983**, *1*, 60-68.

(40) Sherman, A. *Chemical Vapor Deposition for Microelectronics: Principles, Technology, and Applications*; Noyes: Park Ridge, NJ, 1987.

(41) Cabodi, M.; Choi, N. W.; Gleghorn, J. P.; Lee, C. S. D.; Bonassar, L. J.; Stroock, A. D. *Journal of the American Chemical Society* **2005**, *127*, 13788-13789.

(42) Burdick, J. A.; Khademhosseini, A.; Langer, R. *Langmuir* **2004**, *20*, 5153-5156.

(43) Paguirigan, A.; Beebe, D. J. *Lab on a Chip* **2006**, *6*, 407-413.

(44) King, K.; Wang, C.; Kaazempur-Mofrad, M.; Vacanti, J.; Borenstein, J. *Advanced Materials* **2004**, *16*, 2007-2012.

(45) Rolland, J. P.; Van Dam, R. M.; Schorzman, D. A.; Quake, S. R.; DeSimone, J. M. *Journal of the American Chemical Society* **2004**, *126*, 2322-2323.

(46) Terry, S.; Jerman, J.; Angell, J. *IEEE Transactions on Electron Devices* **1979**, *26*, 1880-1886.

(47) Vrouwe, E. X.; Luttge, R.; Vermes, I.; van den Berg, A. *Clinical Chemistry* **2007**, *53*, 117-123.

(48) Gong, X. Y.; Hauser, P. C. *Electrophoresis* **2006**, *27*, 4375-4382.

(49) Reichmuth, D. S.; Shepodd, T. J.; Kirby, B. J. *Analytical Chemistry* **2005**, *77*, 2997-3000.

(50) Kleiner, S.; Faisal, A.; Nagamine, Y. *Febs Journal* **2007**, *274*, 227-240.

(51) Anderson, M. J.; Hansen, C. L.; Quake, S. R. *Proceedings of the National Academy of Sciences of the United States of America* **2006**, *103*, 16746-16751.

(52) Manz, A.; Graber, N.; Widmer, H. M. *Sensors and Actuators B-Chemical* **1990**, *1*, 244-248.

(53) Dittrich, P. S.; Tachikawa, K.; Manz, A. *Analytical Chemistry* **2006**, *78*, 3887-3907.

(54) Dittrich, P. S.; Manz, A. *Nature Reviews Drug Discovery* **2006**, *5*, 210-218.

(55) Woias, P. *Sensors and Actuators B-Chemical* **2005**, *105*, 28-38.

(56) Reichmuth, D. S.; Shepodd, T. J.; Kirby, B. J. *Analytical Chemistry* **2004**, *76*, 5063-5068.

(57) Thorsen, T.; Maerkl, S. J.; Quake, S. R. *Science* **2002**, *298*, 580-584.

(58) Verpoorte, E.; Manz, A.; Ludi, H.; Bruno, A. E.; Maystre, F.; Krattiger, B.; Widmer, H. M.; Vanderschoot, B. H.; Derooij, N. F. *Sensors and Actuators B-Chemical* **1992**, *6*, 66-70.

(59) Liang, Z. H.; Chiem, N.; Ocvirk, G.; Tang, T.; Fluri, K.; Harrison, D. J. *Analytical Chemistry* **1996**, *68*, 1040-1046.

(60) Srinivasan, V.; Pamula, V. K.; Fair, R. B. *Analytica Chimica Acta* **2004**, *507*, 145-150.

(61) Mogensen, K. B.; Eriksson, F.; Gustafsson, O.; Nikolajsen, R. P. H.; Kutter, J. P. *Electrophoresis* **2004**, *25*, 3788-3795.

(62) Salimi-Moosavi, H.; Jiang, Y. T.; Lester, L.; McKinnon, G.; Harrison, D. J. *Electrophoresis* **2000**, *21*, 1291-1299.

(63) Haab, B. B.; Mathies, R. A. *Analytical Chemistry* **1999**, *71*, 5137-5145.

(64) Barnes, M. D.; Whitten, W. B.; Ramsey, J. M. *Analytical Chemistry* **1995**, *67*, A418-A423.

(65) Fister, J. C.; Jacobson, S. C.; Davis, L. M.; Ramsey, J. M. *Analytical Chemistry* **1998**, *70*, 431-437.

(66) Li, M. W.; Spence, D. M.; Martin, R. S. *Electroanalysis* **2005**, *17*, 1171-1180.

(67) Cai, X. X.; Klauke, N.; Glidle, A.; Cobbold, P.; Smith, G. L.; Cooper, J. M. *Analytical Chemistry* **2002**, *74*, 908-914.

(68) Werdich, A. A.; Lima, E. A.; Ivanov, B.; Ges, I.; Anderson, M. E.; Wikswo, J. P.; Baudenbacher, F. J. *Lab on a Chip* **2004**, *4*, 357-362.

(69) Yotter, R. A.; Wilson, D. M. *Ieee Sensors Journal* **2004**, *4*, 412-429.

(70) Cui, Y.; Wei, Q. Q.; Park, H. K.; Lieber, C. M. *Science* **2001**, *293*, 1289-1292.

(71) Hahm, J.; Lieber, C. M. *Nano Letters* **2004**, *4*, 51-54.

(72) Petersen, N. J.; Nikolajsen, R. P. H.; Mogensen, K. B.; Kutter, J. P. *Electrophoresis* **2004**, *25*, 253-269.

(73) Gerdon, A.; Wright, D.; D., C. In *Nanotechnologies for the Life Sciences*; Kumar, C., Ed.; WILEY, 2006; Vol. 3, pp 109-144.

(74) Janshoff, A.; Galla, H. J.; Steinem, C. *Angewandte Chemie-International Edition* **2000**, *39*, 4004-4032.

(75) Sauerbrey, G. *Zeitschrift für Physik* **1959**, *155*, 206-222.

(76) Bain, C. D.; Troughton, E. B.; Tao, Y. T.; Evall, J.; Whitesides, G. M.; Nuzzo, R. G. *Journal of the American Chemical Society* **1989**, *111*, 321-335.

(77) Bain, C. D.; Evall, J.; Whitesides, G. M. *Journal of the American Chemical Society* **1989**, *111*, 7155-7164.

(78) Bain, C. D.; Biebuyck, H. A.; Whitesides, G. M. *Langmuir* **1989**, *5*, 723-727.

(79) Zhang, Y.; Telyatnikov, V.; Sathe, M.; Zeng, X. Q.; Wang, P. G. *Journal of the American Chemical Society* **2003**, *125*, 9292-9293.

(80) Templeton, A. C.; Cliffel, D. E.; Murray, R. W. *Journal of the American Chemical Society* **1999**, *121*, 7081-7089.

(81) Hicks, J. F.; Seok-Shon, Y.; Murray, R. W. *Langmuir* **2002**, *18*, 2288-2294.

(82) Katz, E.; Delacey, A. L.; Fierro, J. L. G.; Palacios, J. M.; Fernandez, V. M. *Journal of Electroanalytical Chemistry* **1993**, *358*, 247-259.

(83) Davis, K. A.; Leary, T. R. *Analytical Chemistry* **1989**, *61*, 1227-1230.

(84) Luo, Y.; Fu, W. *Clinical Chemistry* **2006**, *52*, 2273-2280.

(85) Marx, K. A.; Zhou, T. A.; Montrone, A.; Schulze, H.; Braunhut, S. J. *Biosensors & Bioelectronics* **2001**, *16*, 773-782.

(86) Braunhut, S. J.; McIntosh, D.; Vorotnikova, E.; Zhou, T.; Marx, K. A. *Assay and Drug Development Technologies* **2005**, *3*, 77-88.

(87) Gerdon, A. E.; Wright, D. W.; Cliffel, D. E. *Angewandte Chemie-International Edition* **2006**, *45*, 594-598.

(88) Rickert, J.; Brecht, A.; Gopel, W. *Biosensors & Bioelectronics* **1997**, *12*, 567-575.

(89) Doan, V. V.; Sailor, M. J. *Science* **1992**, *256*, 1791-1792.

(90) Dancil, K.-P. S.; Greiner, D. P.; Sailor, M. J. *Journal of the American Chemical Society* **1999**, *121*, 7925-7930.

(91) Lin, V. S. Y.; Motesharei, K.; Dancil, K. P. S.; Sailor, M. J.; Ghadiri, M. R. *Science* **1997**, *278*, 840-843.

(92) Besenicar, M.; Macek, P.; Lakey, J. H.; Anderuh, G. *Chemistry and Physics of Lipids* **2006**, *141*, 169-178.

(93) Boozer, C.; Kim, G.; Cong, S. X.; Guan, H. W.; Londergan, T. *Current Opinion in Biotechnology* **2006**, *17*, 400-405.

(94) Kurihara, K.; Suzuki, K. *Analytical Chemistry* **2002**, *74*, 696-701.

(95) Rich, R. L.; Day, Y. S. N.; Morton, T. A.; Myszka, D. G. *Analytical Biochemistry* **2001**, *296*, 197-207.

(96) Lyon, L. A.; Musick, M. D.; Natan, M. J. *Analytical Chemistry* **1998**, *70*, 5177-5183.

(97) Haes, A. J.; Van Duyne, R. P. *Journal of the American Chemical Society* **2002**, *124*, 10596-10604.

(98) Lee, H. J.; Goodrich, T. T.; Corn, R. M. *Analytical Chemistry* **2001**, *73*, 5525-5531.

(99) Corn, R. M.; Lee, H. J.; Goodrich, T. T. *Abstracts of Papers of the American Chemical Society* **2004**, *227*, U114-U114.

(100) Goodrich, T. T.; Lee, H. J.; Corn, R. M. *Analytical Chemistry* **2004**, *76*, 6173-6178.

(101) Naimushin, A. N.; Spinelli, C. B.; Soelberg, S. D.; Mann, T.; Stevens, R. C.; Chinowsky, T.; Kauffman, P.; Yee, S.; Furlong, C. E. *Sensors and Actuators B-Chemical* **2005**, *104*, 237-248.

(102) Boecker, D.; Zybin, A.; Horvatic, V.; Grunwald, C.; Niemax, K. *Analytical Chemistry* **2006**, *79*, 702-709.

(103) Wegner, G. J.; Lee, N. J.; Marriott, G.; Corn, R. M. *Analytical Chemistry* **2003**, *75*, 4740-4746.

(104) Smith, E. A.; Thomas, W. D.; Kiessling, L. L.; Corn, R. M. *Journal of the American Chemical Society* **2003**, *125*, 6140-6148.

(105) Brockman, J. M.; Frutos, A. G.; Corn, R. M. *Journal of the American Chemical Society* **1999**, *121*, 8044-8051.

(106) Nelson, B. P.; Grimsrud, T. E.; Liles, M. R.; Goodman, R. M.; Corn, R. M. *Analytical Chemistry* **2001**, *73*, 1-7.

(107) Jordan, C. E.; Frutos, A. G.; Thiel, A. J.; Corn, R. M. *Analytical Chemistry* **1997**, *69*, 4939-4947.

(108) Sepulveda, B.; del Rio, J.; Moreno, M.; Blanco, F.; Mayora, K.; Dominguez, C.; Lechuga, L. *JOURNAL OF OPTICS A-PURE AND APPLIED OPTICS* **2006**, *8*, S561-S566.

(109) Drapp, B.; Piehler, J.; Brecht, A.; Gauglitz, G.; Luff, B. J.; Wilkinson, J. S.; Ingenhoff, J. *Sensors and Actuators B-Chemical* **1997**, *39*, 277-282.

(110) Prieto, F.; Sepulveda, B.; Calle, A.; Llobera, A.; Dominguez, C.; Abad, A.; Montoya, A.; Lechuga, L. M. *Nanotechnology* **2003**, *14*, 907-912.

(111) Brosinger, F.; Freimuth, H.; Lacher, M.; Ehrfeld, W.; Gedig, E.; Katerkamp, A.; Spener, F.; Cammann, K. *Sensors and Actuators B-Chemical* **1997**, *44*, 350-355.

(112) Prieto, F.; Sepulveda, B.; Calle, A.; Llobera, A.; Dominguez, C.; Lechuga, L. M. *Sensors and Actuators B-Chemical* **2003**, *92*, 151-158.

(113) Yotter, R. A.; Lee, L. A.; Wilson, D. M. *Ieee Sensors Journal* **2004**, *4*, 395-411.

(114) Yu, D. H.; Blankert, B.; Vire, J. C.; Kauffmann, J. M. *Analytical Letters* **2005**, *38*, 1687-1701.

(115) Yi, C. Q.; Zhang, Q.; Li, C. W.; Yang, J.; Zhao, J. L.; Yang, M. S. *Analytical and Bioanalytical Chemistry* **2006**, *384*, 1259-1268.

(116) Soper, S. A.; Brown, K.; Ellington, A.; Frazier, B.; Garcia-Manero, G.; Gau, V.; Gutman, S. I.; Hayes, D. F.; Korte, B.; Landers, J. L.; Larson, D.; Ligler, F.; Majumdar, A.; Mascini, M.; Nolte, D.; Rosenzweig, Z.; Wang, J.; Wilson, D. *Biosensors & Bioelectronics* **2006**, *21*, 1932-1942.

(117) Markov, D.; Swinney, K.; Bornhop, D. *JOURNAL OF THE AMERICAN CHEMICAL SOCIETY* **2004**, *126*, 16659-16664.

(118) Tarigan, H. J.; Neill, P.; Kenmore, C. K.; Bornhop, D. J. *Analytical Chemistry* **1996**, *68*, 1762-1770.

(119) Swinney, K.; Markov, D.; Bornhop, D. J. *Analytical Chemistry* **2000**, *72*, 2690-2695.

(120) Swinney, K.; Markov, D.; Bornhop, D. J. *Review of Scientific Instruments* **2000**, *71*, 2684-2692.

(121) Swinney, K.; Markov, D.; Hankins, J.; Bornhop, D. J. *Analytica Chimica Acta* **1999**, *400*, 265-280.

(122) Sorensen, H. S.; Larsen, N. B.; Latham, J. C.; Bornhop, D. J.; Andersen, P. E. *Applied Physics Letters* **2006**, *89*, -.

(123) Sorensen, H. S.; Pranov, H.; Larsen, N. B.; Bornhop, D. J.; Andersen, P. E. *Analytical Chemistry* **2003**, *75*, 1946-1953.

(124) Swinney, K.; Pennington, J.; Bornhop, D. J. *Microchemical Journal* **1999**, *62*, 154-163.

(125) Swinney, K.; Pennington, J.; Bornhop, D. J. *Analyst* **1999**, *124*, 221-225.

(126) Kenmore, C. K.; Erskine, S. R.; Bornhop, D. J. *Journal of Chromatography A* **1997**, *762*, 219-225.

(127) Swinney, K.; Nodorft, J.; Bornhop, D. J. *Analyst* **2001**, *126*, 673-675.

(128) Swinney, K.; Nodorft, J.; Bornhop, D. J. *Applied Spectroscopy* **2002**, *56*, 134-138.

(129) Markov, D. A.; Swinney, K.; Norville, K.; Lu, D.; Bornhop, D. J. *Electrophoresis* **2002**, *23*, 809-812.

(130) Bornhop, D. J.; Hankins, J. *Analytical Chemistry* **1996**, *68*, 1677-1684.

(131) Wang, Z. L.; Swinney, K.; Bornhop, D. J. *Electrophoresis* **2003**, *24*, 865-873.

(132) Liu, Y. J.; Foote, R. S.; Jacobson, S. C.; Ramsey, R. S.; Ramsey, J. M. *Analytical Chemistry* **2000**, *72*, 4608-4613.

(133) Markov, D. A.; Dotson, S.; Wood, S.; Bornhop, D. J. *Electrophoresis* **2004**, *25*, 3805-3809.

(134) Becker, H.; Locascio, L. E. *Talanta* **2002**, *56*, 267-287.

(135) Becker, H.; Gartner, C. *Electrophoresis* **2000**, *21*, 12-26.

(136) Heckele, M.; Schomburg, W. K. *Journal of Micromechanics and Microengineering* **2004**, *14*, R1-R14.

(137) Xia, Y. N.; McClelland, J. J.; Gupta, R.; Qin, D.; Zhao, X. M.; Sohn, L. L.; Celotta, R. J.; Whitesides, G. M. *Advanced Materials* **1997**, *9*, 147-149.

(138) Zhao, X. M.; Xia, Y. N.; Whitesides, G. M. *Journal of Materials Chemistry* **1997**, *7*, 1069-1074.

(139) Duffy, D. C.; McDonald, J. C.; Schueller, O. J. A.; Whitesides, G. M. *Analytical Chemistry* **1998**, *70*, 4974-4984.

(140) McDonald, J. C.; Duffy, D. C.; Anderson, J. R.; Chiu, D. T.; Wu, H. K.; Schueller, O. J. A.; Whitesides, G. M. *Electrophoresis* **2000**, *21*, 27-40.

(141) Markov, D. A.; Swinney, K.; Bornhop, D. J. *Journal of the American Chemical Society* **2004**, *126*, 16659-16664.

CHAPTER III

Modeling Light Propagation

3.1 Simulations with Capillary Flow Systems

In the earliest embodiments of backscattering interferometry, a capillary was used as the flow cell. Some experiments using BI, although rare, are stilled carried out to this day in fused silica capillaries owing to the high finesse interference. Yet at the onset of this work, only two papers had embarked on effectively describing the light propagation through a capillary as used in the BI technique.[1, 2] A more thorough investigation of the capillary flow system is presented here with a description by two different models. Both the accuracy of the simulated fringe patterns and the prediction of total internal reflection by each model are compared to experimental results.

3.1.1 *Ray Tracing Model*

Ray tracing offers an expeditious, yet partial approach to simulating the propagation of light through an optical system. Based on geometric optics, the path of light rays can be followed through optical interfaces and different media. While it would appear tedious to calculate the direction and angle of thousands of rays after multiple interfaces, the use of

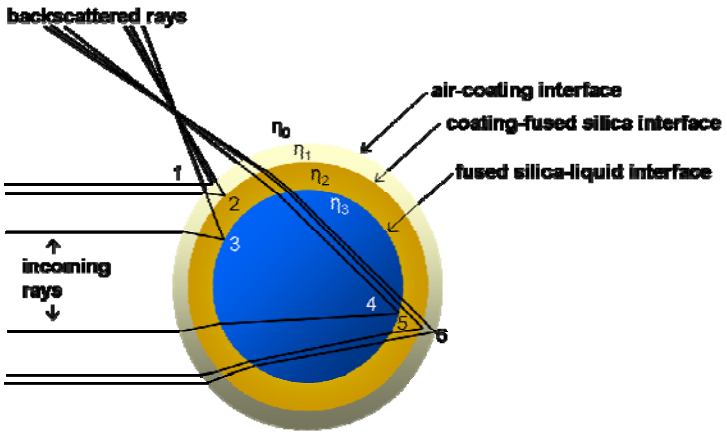

Figure 3.1. Cross-sectional view of a capillary with rays propagated through the system.

transfer matrices and high speed algorithms renders the actual calculation times nominal. Systems similar to BI have been modeled previously using ray tracing approaches. An optical fiber has been modeled previously by ray tracing to determine the ratio between the inner and outer core diameters.[3] A ray tracing approach has also been used to simulate the light propagation through the capillary embodiment of the BI system.[4] However Tarigan *et.al*[4] only monitored light in a 0 - 3° direct backscattered range.

The ray tracing routine used here to simulate the light propagation through a capillary flow system employs a 6-beam model described earlier.[1] Unlike the earlier study by Tarigan, this model includes all angles up to side scattering (i.e. 0 - 90°). For each of the six beams, typically 1000 rays are traced (Figure 3.1). Each ray carries along position, angle, intensity, and phase. Snell's law (Eqn. 1) gives a determination of the angle by the simple equation

$$n_1 \sin\Theta_1 = n_2 \sin\Theta_2 , \qquad \text{Eqn. 1}$$

where n_1 and n_2 are the refractive indices of the media and Θ_1 and Θ_2 are the angle of light propagation through each media relative to the normal axis. *Fresnel equations* are used to determine the intensity of each ray by calculating the reflection and transmission at each optical interface. Interference between rays is calculated by

$$I_{ij} = 2\sqrt{I_i I_j}\cos(\rho_i - \rho_j) , \qquad \text{Eqn. 2}$$

where I represents the intensity and ρ is the phase of rays *i* and *j*. Changes in phase of 180° occur at angles greater than the critical angle

$$\Theta_C = \arcsin(n_2 / n_1) . \qquad \text{Eqn. 3}$$

Incident light impinging upon a new media at angles greater than or equal to Θ_C does not refract into the new media, becoming trapped in the incident media. This process is called total internal reflection (TIR) and is seen to be extremely important in the determination of the absolute refractive of a fluid within a flow cell (*see 3.1.4*). The ray tracing model assumes a circular geometry for the capillary and the light emitted from the laser source is in the form of plane waves. The detection of interference is done so in the far field.

3.1.2 *Wave Based Model*

Systems with circular geometries have also been modeled by partial solutions to Maxwell's equations governing light propagation.[5] The theoretical movement of light through two concentric circles was modeled earlier by Kerker and Matijevic using a solution to Maxwell's equations.[6] These results were later confirmed experimentally by Watkins.[7] In Watkins experiment however, glass fibers with thick claddings were used exhibiting limited similarity to any flow channel routinely used in BI. This model was later extended to fibers with thin claddings by Marcuse and Presby.[8] They observed an abrupt change in the intensity of the backscattered interference pattern. They failed to realize this change was highly sensitive to the refractive index of the media within the fiber. Kerker and Matijevic's initial model was further developed here to describe light simulations in BI through three concentric circles (i.e. coated fused silica capillary containing fluid) and later four circles (addition of an affinity layer within the capillary).

In general terms, the energy distribution E_{tot} of the fringe pattern generated by a circular channel can be expressed as follows

$$E_{tot} = \sqrt{|E_{TE}|^2 + |E_{TM}|^2}, \qquad \text{Eqn. 4}$$

where E_{TE} and E_{TM} represent the polarization states of the total electrical field. The electric field of these polarization states can be determined from the following equations

$$E_{TM} = e^{i\cdot\frac{3}{4}\pi}\cdot\sqrt{\frac{2}{\pi\cdot k\cdot r}}\cdot e^{i\cdot k\cdot r}\cdot T1(\Theta) \qquad E_{TE} = e^{i\cdot\frac{3}{4}\pi}\cdot\sqrt{\frac{2}{\pi\cdot k\cdot r}}\cdot e^{i\cdot k\cdot r}\cdot T2(\Theta) \qquad \text{Eqn. 5}$$

T1 and T2 are the channel geometry dependent scattering coefficients that are expressed in terms of scattering angle Θ

$$T1(\Theta) = b_0 + 2\cdot\sum_{n=1}^{\infty} b_n\cos(n\cdot\Theta) \qquad T2(\Theta) = a_0 + 2\cdot\sum_{n=1}^{\infty} a_n\cos(n\cdot\Theta), \qquad \text{Eqn. 6}$$

where $\Theta = 0°$ corresponds to the forward scatter and $\Theta = 180°$ corresponds to direct backscatter. The scattering coefficients a_0, b_0 in Eqn. 6 are calculated via an array of equations dependant upon the number of interfaces and composed primarily of Bessel and Hankel functions along with their derivatives as described elsewhere[9]. As the radius of the cylinder increases, a greater

number of Bessel and Hankel functions are needed to describe the scattering event. Calculation times become exceedingly long and begin to minimize the effectiveness of such a modeling technique.

To this end a valid stop criterion was established and the developed algorithm output was compared to the Bohren-Huffman model[9] (a single interface model). The input to the model is the size-parameter[6] α_j and n_j, with j indicating the media indices. The model calculates the value for the Bessel function and derivative ($J_m(n_j \alpha_j)$, $J'_m(n_j \alpha_j)$) and the Hankel function and derivative ($H_m(n_j \alpha_j)$ and $H'_m(n_j \alpha_j)$) from $m = 1$ towards infinity. When the Bessel function, J, and its derivative, J', reache a value in the range of 10^{-16} to 10^{-19} the function outputs the corresponding value of m. For the Hankel function, H, the range is 10^{16} to 10^{19}. These ranges are determined by the fact that the solution converges, i.e., increasing the summation does not change the result. The stop criterion reported by the earlier method was based exclusively on empirical trials.[9] There is a difference in the value of m_{stop} between the two methods. For a cylinder radius of 1 μm the calculated E-field intensity difference (ΔI) is on the order of $\Delta I/I = 10^{-8}$ corresponding to a 34% difference in m_{stop}. Since larger radii demand a higher value of m_{stop} for the computation to converge, concentric cylinders cannot have the same m_{stop}. Each individual combination of size parameter and RI result in a given value for the five functions, $J_m(n_j \alpha_j)$, $J'_m(n_j \alpha_j)$, $H_m(n_j \alpha_j)$ and $H'_m(n_j \alpha_j)$, m^i_{stop}. The smallest value is stored for each combination to ensure a usable value. Afterwards all of the individual values are compared and the largest value m^{max}_{stop} is chosen. This ensures complete description of the largest feature, while the smaller features use the values up until their individual value of m^i_{stop} is reached.

3.1.3 *Comparison of Simulated Interference Patterns to Experiments*

Experiments using the capillary embodiment of the BI system were employed to compare the accuracy of the interference patterns produced by the ray tracing and wave based models. The experimental setup used for these investigations is shown in Figure 3.2. An unconditioned HeNe laser (632.8 nm) was directed toward a capillary by a mirror angled at ~45°. The capillary was held in place by a custom made stage with built-in temperature control. This stage was

mounted onto 2 translation stages to provide x-y movement. The fused silica capillary (Polymicro Technologies) used during the experiment had a 100 μm inner diameter (ID), a 150 μm outer diameter (OD) and a 12.5 μm polyimide coating. The capillary was filled with distilled water (DI) for the entire experiment. A beam splitter was positioned directly above the capillary while still slightly below the mirror. This allowed the backscattered portion of the fringe pattern to be directed just behind the stage while also helping to attenuate the scattered intensity. A linear CCD array (Ames Photonics) was positioned to capture the fringe pattern behind the stage. The CCD array contained 3000 elements 7 μm by 7 μm each. The CCD array was mounted and attached to a guide rail, allowing translation perpendicular to the beam splitter. All parts were bolted onto an optical breadboard. The interference pattern produced by this capillary system was acquired by the CCD array.

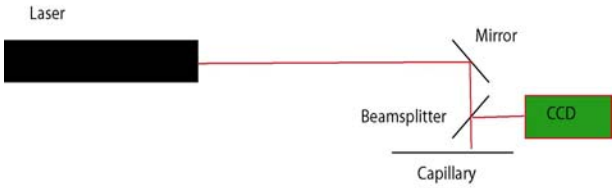

Figure 3.2. Experimental setup of the capillary BI system used to compare the ray and wave based models.

Parameters from the experiment such as ID, OD, coating thickness, distance from laser to capillary, as well as the distance from the capillary to the CCD array were input to the models. Since the capillary was filled with distilled water, the refractive index for the inner cylinder was set at 1.33. The middle cylinder, fused silica, had its RI set to 1.45. And the polymer coating of the capillary was set to 1.72. Simulations of light propagation through this specific system were performed by each model and then displayed using MATLAB software. The experimental fringe pattern produced by this capillary setup and acquired by the linear CCD array is displayed as the solid black line in Figure 3.3. The simulated fringe pattern created by the wave model is also shown in Figure 3.3, represented by a dashed line. The wave model was low pass filtered and offset for visual clarity. From a qualitative standpoint the wave model simulation exhibits excellent agreement with experimental results. The ray tracing model however demonstrated very poor correlation to the experiment near the centroid (0°) with better conformity at angles

greater than 6° (data not shown). In fact, where the experiment and wave model show an attenuated centroid, the ray tracing model predicts over five times more intensity at 0° backscatter implying a maximum should be found at this location (i.e. constructive interference).

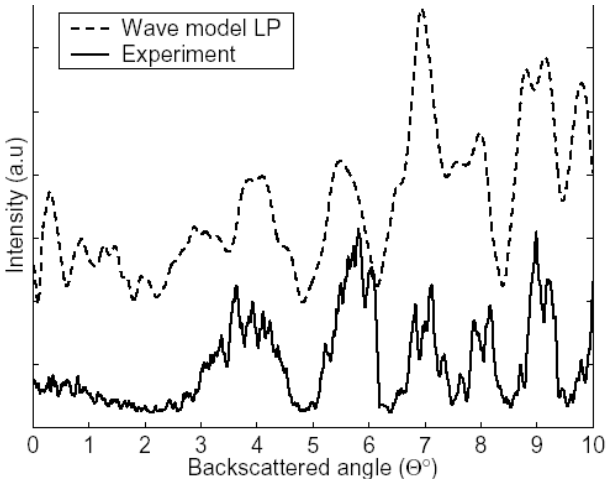

Figure 3.3. Experimental and wave based simulation of interference pattern produced by a capillary.

More quantitatively, fringe counting was used to better measure the accuracy by which each model represents the interference pattern produced experimentally. Here the backscattered angle at every position where a minimum (i.e. destructive interference or relatively no intensity) occurs is documented and compared. These results are given in Table 3.1. As can be seen from the table, the observed angles where minima are located in the experimental interference pattern match perfectly with those produced by simulations employing the wave model falling well within the uncertainty. The ray tracing approach is ill-suited to describe the fringe pattern near direct backscatter with no minima simulated within three and half degrees from the centroid. However, as one moves further away from the centroid, the ray tracing model improves considerably.

Table 3.1. Positional comparison of minima in the simulated and experimental fringe pattern as a function of backscattered angle (Θ°).

	Minima Position (Θ)					
Experiment	2.2 ± 0.4	4.8 ± 0.4	6.4 ± 0.4	7.5 ± 0.4	8.6 ± 0.4	9.7± 0.4
Wave Model	2.2	4.8	6.2	7.4	8.4	9.5
Ray Tracing	NA	3.6	6.5	NA	8.1	9.6

3.1.4 *Total Internal Reflection*

As mentioned previously, Marcuse and Presby[8] observed abrupt changes in the intensity of the backscattered interference pattern when studying fibers with thin claddings. Sørensen *et.al*[1] determined the abrupt attenuation in scattered intensity was highly sensitive to the refractive index of the media within the cylinder. The mechanism behind this phenomenon was total internal reflection within the capillary wall (Figure 3.4). Through this observation, absolute refractive index determinations were realized utilizing backscattering interferometry in a capillary embodiment. Therefore precise modeling for the occurrence of an abrupt reduction in backscattered intensity would permit optimization of BI system parameters when calculating the absolute refractive indices of analytes in the capillary.

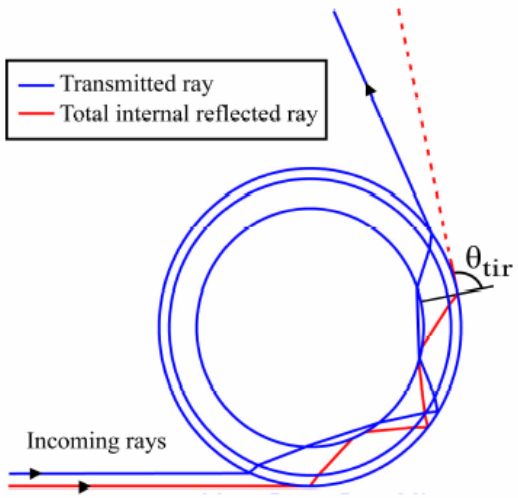

Figure 3.4. Cross-sectional view of a capillary demonstrating a case of total internal reflection (TIR)[1].

The same experimental setup described in *section 3.1.3* was employed again here. The only change made was the use of a larger capillary for ease of injecting more viscous fluids. A capillary with a 542 μm ID and 673 μm OD was used for TIR investigations. The interference pattern was recorded for three different fluids injected into the capillary sequentially. The fluids were chosen for ease of attainment and their different refractive indices. Distilled water (η = 1.33) was the first liquid introduced into the capillary. Following a small equilibration period, the interference pattern produced with water in the capillary was imaged. After the water was removed, ethanol (η = 1.359) was continuously passed through the capillary (ca. milliliters) before the applied pressure was removed. Again a small equilibration period was observed to allow temperature stability and the interference pattern was again recorded. The same process was

repeated once more for ethylene glycol (η = 1.429). The angle at which the intensity abruptly changes for each fluid in the capillary was calculated from the recorded interference patterns.

Simulations of the light scattered by the capillary using both modeling approaches were performed for each fluid. Modeled changes in TIR associated with changing the RI in the core of the capillary were compared to the abrupt decrease in fringe intensity observed experimentally for each individual fluid and displayed in Table 3.2. As the refractive index of the fluid in the capillary approached η = 1.45 (RI of fused silica) a decrease in the angle where intensity attenuation occurred was observed experimentally. Both the ray tracing model and the wave based model simulated this trend. In fact, the closer the RI of the fluid came to that of fused silica the better the ray tracing model began to predict the angle of attenuation. As the refractive index of the fluid approaches 1.45, the simulation becomes much more simplified, where three cylinders are effectively reduced to two. The wave model again showed markedly improved correlation with experimental observations when compared to the ray tracing model.

Table 3.2. Comparison of the observed and predicted angle of total internal reflection.

	Refractive Index, η, (fluid)		
	1.333 (water)	*1.359 (ethanol)*	*1.429 (ethylene glycol)*
Experiment	**44°**	**35°**	**25°**
Wave Model	**43°**	**42°**	**29°**
Ray Tracing	**79°**	**53°**	**36°**

3.2 Simulations in Polymeric Materials

The wave based model proved to be a highly effective approach for simulating the light propagation through a capillary embodiment of BI with precise agreement to experimentally observed results. However, long computation times were a recurring problem with the wave model approach. Larger capillaries with outer diameters near 500 μm or above took weeks for

simulations to be completed. As the movement towards plastics became pervasive in microfluidics and thus BI, a further toll was placed on the wave model since the shapes and sizes of flow channels are widely varying, with no set geometry as in capillaries. While ray tracing did show some promise simulating light propagation through a capillary at wide backscattered angles, the approach failed to accurately depict the interference pattern near direct backscatter. This is especially problematic for our simulations since the detector placement in BI is generally close to the centroid. Further compounding problems, typical microchips have planar dimensions with sharp edges which ray tracing is inherently ill equipped to model. An alternative approach was considered here to better service the new requirements from working with planar flow cells of various geometries in a plethora of potential plastic substrates.

3.2.1 *ASAP Optical Modeling*

Commercially available modeling software was provided to the Bornhop group via educational license by the Breault Research Organization (BRO). This advanced systems analysis program (ASAP®) can be used to model optical systems. ASAP simulates light interaction with optical and mechanical components by Monte-Carlo simulations. Over 1000 light sources exist in the ASAP library for use in simulations while specific sources can be added by the user. The light emitted by these sources can be simulated by tracing geometric rays, wave-optical beams, or wave fields all in three dimensional space. Code is written in a script format to create sources and build the optical and mechanical components of the system. ASAP software offers an exceptional advantage over the previous techniques discussed when describing the mechanical setup of the system. Programs such as AutoCad® or Rhinoceros®, often used to design microchips, can be directly imported into ASAP. This allows a more robust approach to simulating the light propagation in multiple prototypes helping to streamline the engineering process, potentially saving both time and money on unnecessary fabrication procedures. Analysis programs are built into ASAP software allowing rapid characterization once the simulation is complete. Calculations such as power and intensity are easily made from drop

down menus while monitoring splits or tracking individual beams through components can also be accomplished.

Light interaction through the BI system has been studied previously using ASAP software in the work of Swinney *et.al.*[10] In their work, the microfluidic chip was created by etching a fused silica substrate. This technique created hemispherical flow channels with a small flat piece at the apex due to the etching process. A flat piece (top plate) of fused silica was annealed to the etched structure creating a channel for possible fluid flow. Access holes to the channel were laser ablated. Simulations performed by Swinney, *et.al*[10] confirmed experimental results whereby the interference pattern shifts spatially with changes in the refractive index of the solution contained within the channel. Different wavelengths of light and altering the ratio of the substrate/top plate thickness were also shown to affect the properties of the interference pattern produced.[10]

3.2.2 *Modeling Different Channel Geometries*

ASAP modeling software was used here to simulate the light interaction through the BI system in a plastic substrate, PDMS. Three different geometries (Figure 3.5) for the channel structure were chosen to compare sensitivity of different designs and help guide the direction of future fabrication requirements. Since most traditional lithographic techniques produce planar structures, including the soft lithographic approaches typically used to fabricate microfluidic channels in PDMS, a rectangular geometry was selected. The rectangular channel is also the easiest design to fabricate, decreasing both production time and cost. A circular geometry, already known to produce high contrast interference fringes, was selected for its well known sensitivity in the capillary BI embodiment. The circular geometry would serve as a standard by which all other

Figure 3.5. Three flow channel geometries: rectangular, semi-circular, and circular compared by ASAP during optical modeling of BI system.

geometries would be compared. The semi-circular channel was selected to mimic devices typically obtained during wet etch procedures such as the fused silica chip mentioned previously. If their sensitivities were shown to be comparable, a semi-circular channel would allow for faster chip production compared to that of a circular polymeric structure by easing alignment and assembly requirements.

A coherent light source propagated as wave-optical (parabasal) beams were used in the ASAP simulations. These beams are treated as rays, but carry phase and polarization information as well as have a physical extension in space. This characteristic allows for the central rays to miss an edge during propagation, but still have the beam bend depending on how much of the physical extension contacts the edge. Code was written in ASAP to setup the optical model as close to known experimental conditions as possible. The parabasal beams were positioned 283 mm from the flow channel and were given a wavelength of 632.8 nm. One thousand beams were used in the simulations and multiple splits were allowed. The beams impinged the channel perpendicular to fluid flow. Optical properties and average experimental dimensions of the polymeric chip, the glass slide bonded to the PDMS, and the black absorbing mount were input into the script file. The results of the simulation are limited in accuracy by the number of beams traced and the precision in which the system is described.

The rectangular channel was set to have fluidic dimensions of 60 μm in width and 70 μm in height. Simulated fringe patterns produced by altering the refractive index of the fluid contained within the rectangular channel are shown in Figure 3.6. As seen experimentally and published elsewhere[1, 2, 4, 10, 11], the position of the simulated interference pattern detected by BI is sensitive to the refractive index of the fluid contained within the microfluidic channel. The range in refractive indices displayed in Figure 6 is 0.001. For a $\Delta RI = 1 \times 10^{-5}$, the fringe pattern produced by the rectangular channel shifted 0.02°. The interference pattern produced by the rectangular channel was not observed to have shifted for $\Delta RI > 1 \times 10^{-6}$. The detection limit common to most experimental results obtained by BI when using a single microfluidic channel molded in PDMS with no signal filtering or compensation are in a refractive index units (RIU)

range of high 10^{-7} to low 10^{-6}. This would indicate the simulations using wave-optical beams in ASAP software to describe the light propagation through BI do so with reasonable accuracy.

The semi-circular and circular channel geometries were also modeled by ASAP using the same optical configuration described for the rectangular structure. To maintain an accurate comparison of the three different geometries, each fluidic channel's cross sectional area was exactly the same in each simulation. Completion of the simulations again using parabasal beams indicated a dramatic increase in sensitivity for the hemispherical and circular channels geometries when compared to the earlier results from the rectangular channel analysis. Whereas the rectangular PDMS channel simulation produced a 0.02° fringe shift for a $\Delta RI = 1 \times 10^{-5}$, the fringe pattern produced the semi-circular and circular channels shifted 6°. The fringe patterns for both the semi-circular and circular channels were still seen to have shifted for $\Delta RI = 1 \times 10^{-8}$ with little

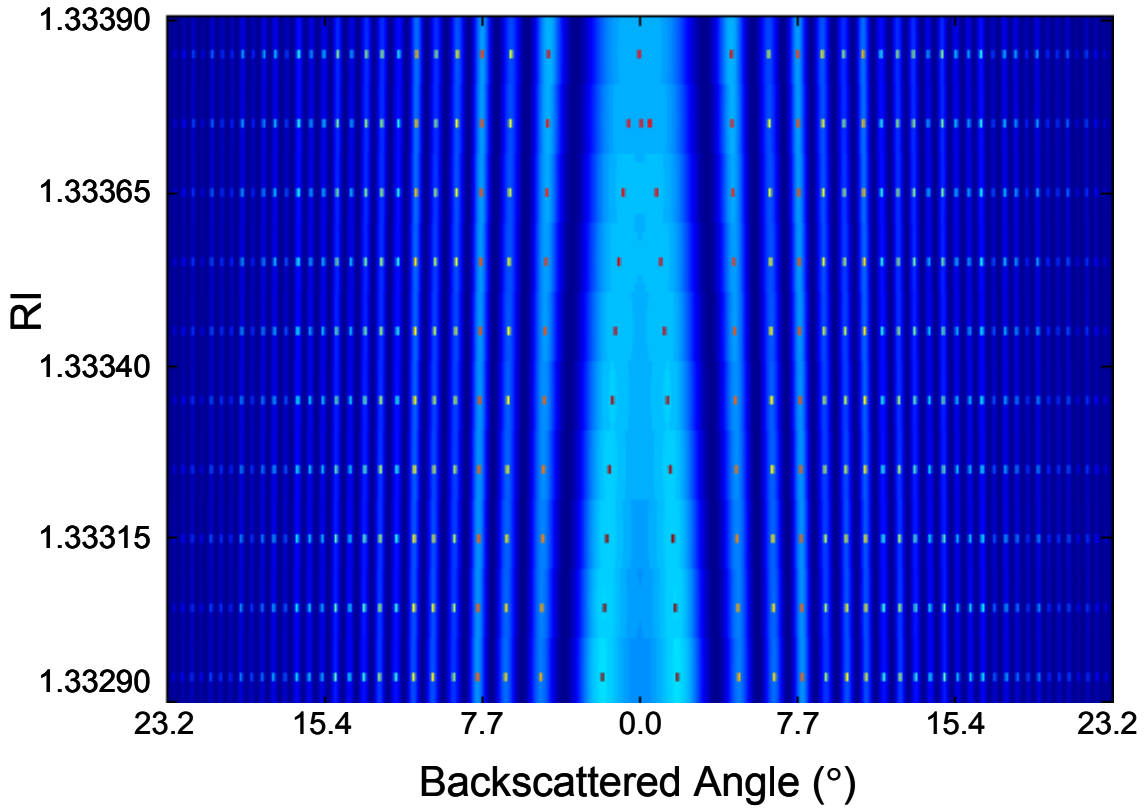

Figure 3.6. Simulated fringe shift due to changing the RI of the fluid in a rectangular channel (60 µm by 70 µm) by ASAP modeling software.

to no difference in the degree of their displacement. This represents a two orders of magnitude increase in sensitivity for the semi-circular and circular channels.

3.3 Fringe Analysis and Sensitivity

The high finesse BI instrument is capable of sensing infinitesimal changes to the spatial position of interference fringes produced during experiments because of the highly resolved maxima and minima. Since the interference pattern is produced by the interaction of light waves with the structure, interfaces, and fluids of the microfluidic chip many factors determine the spatial distribution and orientation of the fringes including channel dimensions, channel geometry, substrate material, affinity layers, and the fluid within the flow cell. The size and shape of interference fringes produced during BI experiments, as well as their frequency, are heavily dependant upon the same parameters.

Any changes to these parameters alter the path light takes through the device and in turn modify the interference pattern. Small changes in optical pathlength are detected as spatial shifts in the fringe position by BI. However, larger modifications to the system can greatly influence the frequency and distribution of the interference pattern and thus vary the overall sensitivity of the instrument. As mentioned above, the channel geometry plays an important role in the system sensitivity. Simulations showed that changing the channel shape from a rectangular to a circular or semi-circular geometry (while maintaining equivalent surface areas for each geometry) increased system sensitivity by two orders of magnitude. Interference fringes produced by thin walled capillaries were also shown to shift spatially to a higher degree than capillaries with thicker walls. For instance, a capillary with an ID = 100 μm and an OD = 160 μm produced a 1.626° spatial shift when the RI was changed by 5×10^{-4}. However, another capillary with the same inner core diameter but 28 μm thicker outer shell only produced a 0.834° spatial shift for the same variation in RI, thereby cutting the system sensitivity in half. A similar trend was also observed by Swinney et.al[2]. The overall size of the capillary can also play an important role with simulations suggesting sensitivity is inversely proportional to capillary size. In fact, sensitivity was shown to

decrease by a factor of 3.5 when a capillary with an ID = 542 μm and an OD = 673 μm was compared to the more standard 100 μm : 160 μm (ID : OD) fused silica capillary. Even the ratio of chip height to thickness of substrate support has given insight into the system with an optimal ratio of 2 : 1 exhibiting an ~33% increase in sensitivity over chip height to substrate support thickness ratios of 5 : 1 or 1 : 1.[10] The wavelength of light chosen as the illuminating source also influences sensitivity with shorter wavelengths outperforming sources with longer wavelengths. Refractive index unit (RIU) detection limits calculated from simulations by ASAP software produced $\Delta\eta = 9.74 \times 10^{-6}$ for a 488 nm coherent light source while 670 nm light yielded a detection limit of $\Delta\eta = 1.39 \times 10^{-5}$.[2]

BI sensitivity to spatial position is greatly enhanced by its multi-pass nature, whereby light can interact with the fluid sample and the microchip numerous times. Calculations into the effective optical pathlength suggest photon interaction within the microfluidic channel increases, on average, a factor of 100. A quasi-hemispherical channel with a depth of 40 μm and a width of 90 μm was evaluated to have an effective optical pathlength of ~ 1 cm. However, this represents a mere average pathlength for light interaction within the microfluidic channel with some rays undoubtedly traversing the fluid and channel more frequently than others. This may be manifested in the interference pattern by certain fringes (i.e. those that propagate in the channel longer) exhibiting higher sensitive with changes to the channel structure/topology or fluidic media. In capillary embodiments of BI, three distinct frequencies can be seen in the interference pattern as demonstrated in Figure 3.7 and reported previously.[1,12] The high frequency (HF) component shows no sensitivity to variations in the refractive index of the

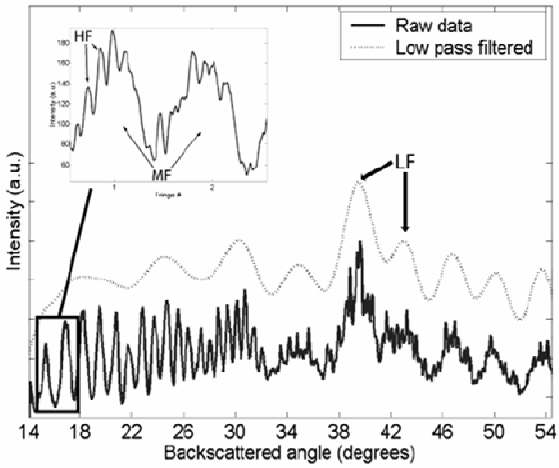

Figure 3.7. Demonstration of the low frequency (LF), medium frequency (MF), and high frequency (HF) components of the interference pattern produced by a capillary with an ID = 100 μm and an OD = 160 μm.[1]

fluidic media and was revealed to be spatially fixed. It was determined the high frequency component is produced by scattering from the edges of the capillary and thus has no interaction with its inner core. The low frequency (LF) component of the capillary embodiment exhibited little sensitivity to changes in the optical pathlength as well. This frequency component is primarily produced by the *common* interference of light reflected from the front of the capillary and the back wall of the capillary. The medium frequency (MF) component does however demonstrate ultrahigh sensitivity as it is created by interference from light impinging the front and back walls of the capillary core. Rays from the front and back of the capillary experience a large relative change in optical pathlength and thereby induce the medium frequency component to shift spatially with changes to the channel structure/topology or fluidic media.

While the above description holds true for circular channel geometries, the same cannot be said for rectangular geometries. The interference pattern produced by rectangular channels in fact shows no high frequency component (Figure 3.8). And unlike the capillary, the low frequency component is also highly sensitive to any changes in the optical path. Experimental observations have shown the low frequency component can, in some cases, produce a greater response than the medium frequency with reduced noise. Quantitative measurements of simulated interference patterns obtained from rectangular channels by ASAP software also predicts fringes closer to the centroid shift spatially to a higher degree. The first fringe removed from the centroid shifts more

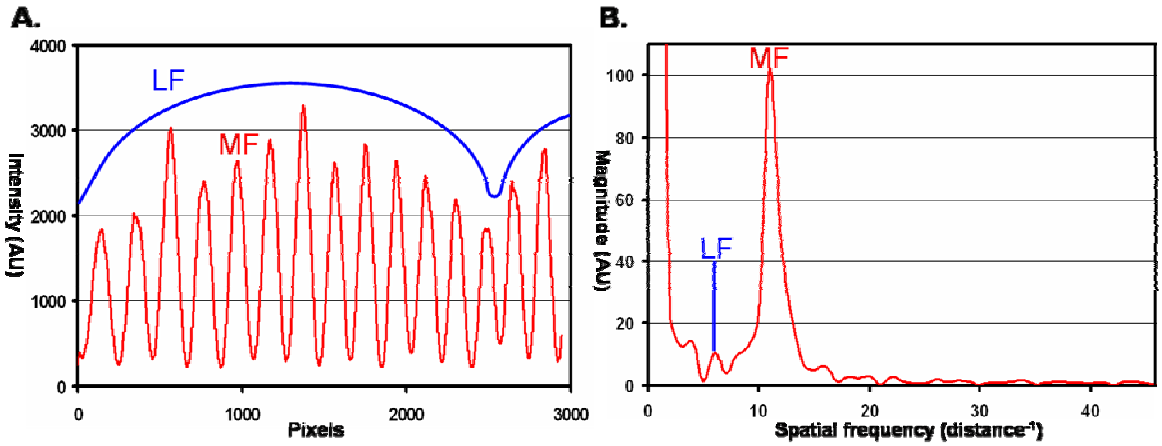

Figure 3.8. **A.** Low frequency (LF) and middle frequency (MF) components are easily distinguished in the interference pattern produced by rectangular channel geometries. **B.** The magnitude spectrum also demonstrates the presence of two frequencies. Note the absence of any high frequency component.

than four times further than the sixth fringe for a channel 60 μm tall and 70 μm wide. The interference pattern originating from rectangular channels can also be biased to one side of the centroid by creating a slight angle in the typically perpendicular incidence angle of the wavefront of light with respect to the channel/fluidic flow. This creates an effect similar to a Fabry-Perot interferometer and also increases the diffraction at two corners of the rectangular channel. Even more intriguing, through our collaboration with Dr. Florian Forster (formerly of Lund University, Lund, Sweden), simulations of light propagation through rectangular structures using a Finite-Difference Time-Domain (FDTD) model predicted 'hot spots' in the resulting interference pattern where sensitivity was increased over a factor of 100.

3.4 Summary

The wave model proved to be an excellent prognosticator for the interaction and propagation of light through a capillary embodiment of BI. Simulations produced by the wave model correlated to experimental observations with very high accuracy. Both the prediction of TIR and the overall description of the interference pattern by fringe counting illustrated the wave model's applicability to any future work using capillary flow cells. Ray tracing, while not nearly as accurate as the wave model, could be used as fast first approximation of capillary experiments as the wave model does require long calculation times. Ray tracing could be especially applicable to any insight into the interference pattern not near the centroid (ca. ± 6°).

Simulations of light interaction with multiple channel geometries in PDMS using ASAP optical modeling software provided a measure of sensitivity to guide chip selection on an experiment by experiment basis. ASAP provides exceptional utility, allowing for the rapid simulation of various channel designs in a wide range of substrate materials with the use of multiple optical components. The utility of ASAP is expanded further by its ability to import chip designs from commonly used software programs as well as its built-in analysis functions. Furthermore, simulations produced using ASAP software also gave great insight into the future directions that should be explored in chip fabrication by indicating increased sensitivity for semi-

circular and circular channel designs. A brief synopsis was also given offering an analysis of the interference pattern and insight into the sensitivity of BI.

(1) Sorensen, H. S.; Pranov, H.; Larsen, N. B.; Bornhop, D. J.; Andersen, P. E. *Analytical Chemistry* **2003**, *75*, 1946-1953.

(2) Swinney, K.; Markov, D.; Bornhop, D. J. *Review of Scientific Instruments* **2000**, *71*, 2684-2692.

(3) Horton, R.; Williams.Wj *Journal of the Optical Society of America* **1973**, *63*, 1204-1210.

(4) Tarigan, H. J.; Neill, P.; Kenmore, C. K.; Bornhop, D. J. *Analytical Chemistry* **1996**, *68*, 1762-1770.

(5) Pedrotti, F.; Pedrotti, L. *Introduction to Optics*; Prentice Hall, 1996.

(6) Kerker, M.; Matijevic, E. *Journal of the optical society of America* **1961**, *51*, 506-508.

(7) Watkins, L. S. *Journal of the Optical Society of America* **1974**, *64*, 767-772.

(8) Marcuse, D.; Presby, H. M. *Journal of the Optical Society of America* **1975**, *65*, 367-375.

(9) Bohren, C. F.; Huffman, D. R. *Absorption and Scattering of Light by Small Particles*; Wiley: New York, 1983.

(10) Swinney, K.; Markov, D.; Bornhop, D. J. *Analytical Chemistry* **2000**, *72*, 2690-2695.

(11) Markov, D.; Begari, D.; Bornhop, D. J. *Analytical Chemistry* **2002**, *74*, 5438-5441.

(12) Markov, D.; Swinney, K.; Norville, K.; Lu, D.; Bornhop, D. *ELECTROPHORESIS* **2002**, *23*, 809-812.

CHAPTER IV

MICROFLUIDIC SYSTEMS

4.1 Planar Fabrication

Planar channels are commonplace in microfluidic devices. The lithographic techniques mentioned previously (*see 2.1.2*) are two dimensional processes limiting designs to linear coordinates in an x (width) versus y (height) plane. Curved surfaces are generally dependant upon isotropic wet etches requiring harsh chemicals (strong acids, strong oxidizers, e.g.) and limiting throughput. Research driven interests are best served by a combination of optical[1] and soft lithography[2]. Optical lithography affords the use of a 'master' structure from which multiple chips can be fabricated by soft lithographic processes. A background of both optical and soft lithography is given here along with a general outline for the production of PDMS chips used in later applications (*see Chapter VI*).

4.1.1 *Optical Lithography*

Optical or photolithography is a well established method for the fabrication of 'master' structures. As stated earlier, photolithography is a parallel processing technique used in combination with a photomask, a photoresist coated substrate, and a mask aligner. In photolithography, the entire pattern of the photomask is cast onto the coated substrate in a single step. Optical lithography primarily uses ultraviolet (UV) light sources during the exposure process with i-line sources (365 nm) the most common. However, the specific wavelength used is resist dependant. The UV wavelengths employed in photolithography cause lateral structural resolution to be diffraction limited. The diffraction effects can be lessened by contact printing which reduces the gap between the photomask and the substrate to almost zero. The resolution of most general use cleanroom mask aligners is on the order of the light source's wavelength, thus 365-500 nm.

The photomask used in optical lithography contains the fluidic design of the desired microchip. The design is created using typical graphics software such as AutoCad® or CleWin®. The photomask is typically fabricated by two methods: e-beam lithography or transparency printing. The resolution of structures attainable by transparency printing is dependant upon the resolution of the printer used. High dpi (dots per inch) printers in the range of 20000 – 40000 are needed to generate structures of 20 μm. This renders transparency printing to primarily large scale structures (ca. 50 μm and above). Photomasks produced by e-beam lithography are the most commonly used masks in chip fabrication. E-beam photomasks offer single nanometer resolution. They are also much more durable than transparency masks, consisting of thick soda lime with a thin layer of chrome. It is worth noting that the widths of the line dimensions in the photomask become the width of the channels in the microfluidic chip.

The photoresists used in optical lithography are generally organic/inorganic polymers that can either be crosslinked by photoactivation (negative resist) or solubilized by photolysis (positive resist). There are two general methods to make resists photoactivatable: incorporate photosensitizers or groups that undergo photocycloaddition into the polymer or add initiators or sensitizers to the resist solvent system. Films of photoresist are spun onto pre-cleaned wafers. Clean wafers are a necessity for high grade fabrication as contaminants can be transferred or prevent the polymerized resist from adhering to the wafer. The thickness of the film is governed by the spin speed used and the viscosity of the photoresist. This is an important parameter to optimize as the thickness of the film will become the height of the channels in your final device.

Figure 4.1. Example of T-topping from overexposure of SU-8 by low UV wavelengths.

The negative photoresist, SU-8 (Microchem), is one of the most widely used resist in chip fabrication. SU-8 contains a photointiator called triaryl sulfonium salt.[3] Upon UV exposure the photoinitiator generates an acid. The acid catalyzes polymerization with the

addition of heat. The optimized absorbance for SU-8 is at 365 nm. Absorbance of higher energy light can result in a phenomenon termed T-topping (Figure 4.1). T-topping creates negative sidewalls. At wavelengths below ~350 nm the top of the resist is overexposed, limiting light penetration and thus polymerization. The exposure time required for complete initiation to occur is based on the thickness of the photoresist layer. Microchem provides exposure dosage versus film thickness graphs with there resists helping streamline fabrication.

The fabrication of masters in this project employed an e-beam generated photomask and different viscosities of the negative photoresist, SU-8 (Figure 4.2). CleWin 2.7 layout editor software was used to design the fluidic network. A soda lime/chrome mask was generated from this design by Delta Mask (The Netherlands) where the chrome layer was ~ 100 nm in thickness. Three inch silicon wafers (P <100>) were generally used as the substrate material of the master. Silicon wafers were cleaned by sonication in isopropyl alcohol (IPA), rinsing with distilled water and followed with treatment by a boiling piranha solution (1 : 4 of 40% hydrogen peroxide: concentrated sulfuric acid). The wafers were rinsed and placed on a hot plate at 95°C for 5 minutes just prior to resist deposition. SU-8 2000 series photoresists were evenly deposited on the Si wafer using a Laurell WS-400 Bench-top single wafer spinner. A few milliliters of the resist were poured onto the center of the wafer and spinning commenced in a two stage process. The first spin is generally around 10 seconds at a few hundred rpm's (revolutions per minute) to spread the resist. The speed of the wafer was then increased thousands of rpm's for approximately half a minute to form a homogeneous coating. The wafer was then removed from the spin coater and placed on a hot plate for a soft bake to remove solvent (typically 3 min @ 65°C ⇒ 9 min @ 95°C). The wafer was allowed to cool to room temperature. UV exposure through the photolithographic mask for seconds was accomplished using a Karl Suss MJB3 contact mask aligner. Following irradiation,

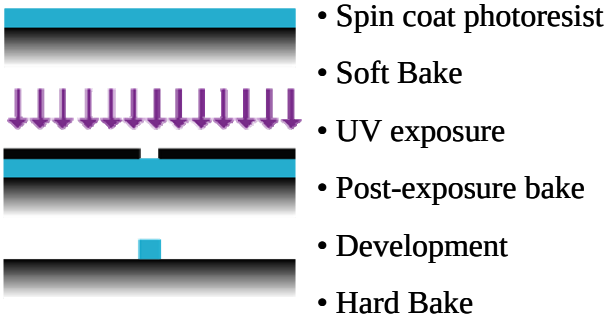

Figure 4.2. Generic outline of master production.

a post exposure bake (PEB) was performed (1 min @ 65°C ⇒ 7 min @ 95°C) to promote polymerization. The wafer was again cooled to room temperature. Unexposed areas of SU-8 photoresist were then removed using a SU-8 organic developer from Microchem. Isopropyl alcohol (IPA) was used to ensure the wafer was completely developed. IPA will form a milky white substance on the wafer if any unexposed photoresist remains. The master mold was then rinsed and hard baked (~5 hours @ 200°C) to ensure device stability. An Alphastep 200 stylus surface profiler (Tencor Instruments) was used to accurately measure the height of the standing relief structures.

4.1.2 *Soft Lithography*

Soft lithography is a cost effective and convenient method for micro and nanofabrication. The technique presents a rapid manner by which prototypical devices can be designed and fabricated within one day's time. The two most common aspect of soft lithography are cast/replica molding and microcontact printing (μCP). In microcontact printing, an elastomeric stamp with patterned relief structures is dipped into a solution. The stamp is then pressed onto a substrate and makes firm contact for a few seconds and is then removed. The solution is thus transferred to the substrate in the same pattern as the relief structure of the stamp. μCP is a common technique used for the patterning of surfaces with self-assembled monolayers.[4-6]

Cast molding is used to effectively duplicating the fluidic network of the master produced by optical lithography in an elastomeric substrate. UV and thermally curable polymers are used as the casting agents and poured over the master structure. After the polymers are cured they physically removed from the master and can be sealed to a solid support for fluid flow.

The most common cast polymer currently being used in soft lithographic fabrication is polydimethlysiloxane (PDMS). PDMS is an inorganic, elastomeric material exhibiting excellent qualities for microchip fabrication. Since it is an elastomer, PDMS can make conformal contact with the solid master substrate ensuring an accurate replication of the channel structures. PDMS is gas permeable, an attractive quality for cell studies.[2] However, the fluids that can be used in PDMS molded channels are limited as numerous inorganic solvents swell PDMS.[7] The

elastomer does have good thermal stability though with relatively low shrinkage upon curing. PDMS is chemically inert, has a low interfacial free energy and is not hydroscopic.[2] The surface of PDMS can be easily modified allowing surface attachment of biomolecules.[8, 9] PDMS devices are also compatible with optical systems as PDMS itself is optically transparent down to approximately 300 nm while exhibiting no auto fluorescence. The use of PDMS as a substrate for microfluidic devices allows for large-scale integration.[10]

All microfluidic chips used in the applications section were fabricated by soft lithographic techniques. Cast molding was performed using PDMS, purchased as Sylgard 184 (Dow Corning, Midland, MI). Prior to casting, the PDMS was mixed in a 10 : 1 ratio (base : curing agent) and degassed in a vacuum desiccator. PDMS was cast over the master that had been placed into a 100 mm × 15 mm Falcon Petri dish (Becton Dickinson, Franklin Lakes, NJ) such that the height of the PDMS was ~ 2 mm. The Petri dish was again placed into a desiccator and a vacuum was applied for further degassing. Once no air bubbles were visibly present, the Petri dish was removed from the desiccator and set in a large convection oven for roughly 8 hours @ 65°C.

After the curing process was complete, the Petri dish was removed from the oven and allowed to cool briefly. The PDMS microchip was physically removed from the Si master mold by fine precision scalpel and tweezers. Access ports for sample introduction (2 ports) and applied vacuum/waste removal (1 port) were mechanically punched out by stainless steel capillary tubing. PDMS, with the fluidic network facing up, was then plasma oxidized for ~ 10 sec by along with a 3″ × 1″ × 1 mm microscope glass slide (Fisher Scientific) cleaned in the same fashion as the bare Si wafer. Oxidation of the PDMS promotes a hydrophilic channel surface. Following oxidation, the PDMS was sealed to the microscope slide so that the fluidic network was in contact with the glass. Water was kept in the channels molded in the PDMS until experiments were run to help maintain the hydrophilic surface created by plasma oxidation. All optical and soft lithography steps were conducted in VIIBRE (Vanderbilt Institute for Integrative Biosystems Research and Education) clean rooms.

4.2 Fabrication of Semi-circular Channels

The modeling performed in Chapter 3.2 predicted semi-circular and circular channels molded in PDMS would give two orders of magnitude greater sensitivity when used in the BI system as compared to rectangular channels. However no standard protocol existed for the fabrication of circular geometries in any type of substrate at the inception of this project. It had been shown though that the slit width of a protective mask through which isotropic etching of a substrate occurs played an important role in the etched geometry.[11] The initial strategy was to isotropically etch fused silica to produce semi-circular channels, but this approach provided no fruitful results. Semi-circular channels were eventually fabricated for use in the BI system by the isotropic etching of silicon through a tiny slit. Subsequently, the silicon was electroplated (for structural stability). Injection molding of the electroplated master allowed for the rapid fabrication of polymeric chips with semi-circular channels at low costs. Details for the ***final*** fabrication steps (Figure 4.3) are provided below forgoing details of the numerous iterations that were attempted and the many different parameters (slit width, protective masks, ethane solutions, etc.) that were altered to obtain the desired structure.

4.2.1 *Sacrificial Layers and Mask Opening*

Bare silicon wafers with no doping were submitted to a stringent cleaning process (Table 1) to ensure the silicon surface was extremely clean and the native oxide layer was removed. A clean surface is essential for the uniformity and adhesion of the sacrificial layer. If any defects are present pinholes will be created in the sacrificial layer permitting undesired etching and creating unwanted features in the substrate. The removal of the native SiO_2 layer is critical for this procedure. Any SiO_2 that remains on the silicon wafer will thus be under the sacrificial layer. Since hydrofluoric acid (HF) is in the etching mixture, this native oxide would be removed from under the sacrificial layer and thus destabilize the entire protective mask.

Silicon nitride, Si_3N_4, was used as the sacrificial layer immediately above the silicon substrate. Low pressure chemical vapor deposition (LPCVD) was used to grow 190 nm of Si_3N_4 on the Si wafer. Si_3N_4 served as the final etch resist. The etch mask pattern was defined in the

Si_3N_4 layer by lift-off of silicon dioxide using a negative photoresist. Futurex 1000 PY negative tone photoresist was applied in a 1.5 μm thick layer by spin coating and soft-baked on a hotplate for 35 seconds at 150°C. The resist was exposed for 400 seconds through a photolithographic mask containing the desired pattern using a Karl Suss MJB3 mask aligner.

Table 4.1. Procedure for cleaning the Silicon wafer.

A. Removal of unwanted organics and some metals.
1. The wafer is immersed in a (5 : 1 : 1) solution of H_2O : NH_4OH : H_2O_2. The solution is heated to 75 - 80°C for 10 minutes.
2. The solution is quenched under running DI water for 1 minute.
3. Washed the wafer in DI water for 5 minutes.
B. Removal of the native SiO_2 layer.
1. The wafer is immersed in a (1 : 50) solution of concentrated HF : H_2O for 15 seconds.
2. Washed in running DI water with agitation for 30 seconds.
C. Removal of heavy alkali metals.
1. The wafer is immersed in a (6 : 1 : 1) solution of H_2O : HCl : H_2O_2 for 10 minutes at 75 - 80°C.
2. The solution is quenched under running DI water for 1 minute.
3. Washed in DI water for 20 minutes.

The wafer was then post-baked for 1 minute at 100°C and developed in Futurex RD6 developer for 13 seconds. Lift-off was facilitated by a controlled undercut formed during development of the Futurex photoresist. Photoresist residues (approx. 200 nm in thickness) were removed by a brief oxygen plasma etch, leaving 1.3 μm of photoresist on the exposed areas. Using a quartz sample, 200 nm of SiO_2 were deposited on the wafer by E-beam evaporation in the VIIBRE labs. The lift-off procedure was then achieved by submersion of the wafer in photoresist stripper with sonication for 1 hour creating an opening in the oxide layer. The sacrificial nitride layer was then opened by boiling phosphoric acid. Etching in H_3PO_4 was performed between 165 - 175°C for 50 minutes. The phosphoric acid etch rate for Si_3N_4 is over 1000 times faster than SiO_2.

4.2.2 *Silicon Etching*

Isotropic etching of the Si wafer through the nitride mask is performed by a HNA solution with agitation. HNA is a combination of concentrated hydrofluoric acid (HF), concentrated nitric acid (HNO_3), and concentrated acetic acid (CH_3COOH) in a 1 : 2 : 1 volume ratio. The nitric acid oxidizes the silicon surface to silicon oxide. The SiO_2 is then continuously etched by the HF in an isotropic fashion releasing SiF_4(g). Acetic acid is present to reduce the surface tension and limit the numbers of bubbles at wafer/Si interface which can stop or alter the chemical etch of the silicon surface. The HNA mixture etched the Si wafer at roughly 10 μm/min. The etched channel structures had some visually observable surface roughness. Chemical "polishing" was accomplished by immersion of the etched structures in a mixture of NH_4F (3.7 g) and conc. H_2O_2 (10 ml) at room temperature for 3 minutes. The chemical polishing removed 1 - 2 μm of silicon, as

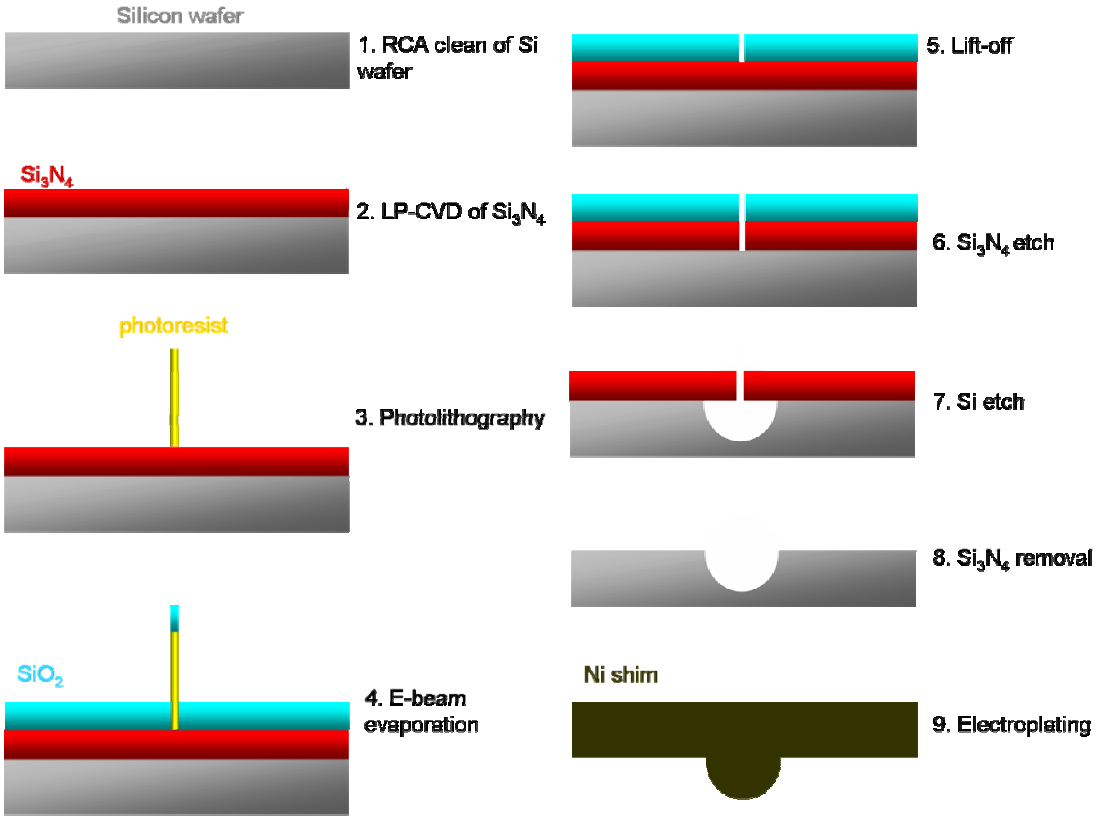

Figure 4.3. Procedural schematic of isotropic etch in Si wafer.

measured by profilometer. The silicon nitride mask was removed in boiling concentrated H_3PO_4 at 175°C for 90 minutes as the final step.

Figure 4.4A displays the sample Si wafer with PDMS poured into the semi-circular structure. The depth of the etch was 50 μm and the total width of the structure was 101 μm creating an almost perfect hemispherical structure. This result was obtained using a 5 μm slit width in the sacrificial layer. The surface roughness of the obtained semicircular structures was reduced by a chemical polishing step using a mixture of NH_4F and H_2O_2. This polishing step removed approximately 1 – 2 μm.

4.2.3 *Electroplating and Injection Molding*

Since the silicon wafer does not have a high enough conductivity for use in electroplating, a thin film (ca. ~2 nm) of gold was sputtered onto the Si wafer. The wafer was then shipped to Dandisc (Sakskøbing, DK). There the wafer was electroplating with nickel (Ni) in a similar fashion as that reported earlier (*see 2.1.2*). The Ni shim (Figure 4.4B) was pealed off the Si wafer resulting in a negative relief of the fabricated structure. However, the electroplating process transfers the surface motif almost undistorted to the backside of the resulting nickel shim. This approach is not acceptable for high accuracy injection molding because the high pressures employed in the molding process would deform a shim with an uneven backside substantially. We used the strategy of plating a thicker nickel shim than required and removing the transferred motif from its backside by grinding to form a planar back. The Ni shim was 400 μm thick and needed to be ground down to 275 μm to fit into the injection molding tool. Grinding was performed on an automated high precision grinder (Logitech PM5, Logitech, Glasgow, Scotland). The slurry used for the first 100 μm consisted of 9 μm Al_2O_3 particles while the last 25 μm were removed by polishing with a diamond slurry (<1 μm particles).

Topas 8007 and 5013 from Ticona (Ticona AS, DK) were the polymers chosen for injection molding. Topas was chosen for multiple reasons not the least of which was because *free* samples were supplied. Topas is an optical grade polymer with low birefringence, high light transmission (92%), and minimal elongation characteristics. But even more importantly, Topas

8007 and 5013 have the same optical properties but different glass transition temperatures (T_g), 70°C and 130°C respectively. This difference in T_g allows two semi-circular chips, one of each Topas polymer, to be aligned and bonded at T > 70°C to create a fully circular polymer chip as seen in Figure 4.4C. Briefly, two unsealed flow systems, one Topas 8007 chip and one Topas 5013 chip, were treated in oxygen plasma to increase their hydrophilicity. The treated surfaces were found to have a water contact angle of <10° for weeks. The open systems were sealed by aligning the two chips with the fluidic networks facing each other, resulting in a circular channel. The two halves were pressed together by a pressure of 8.7 kPa and then heated to 100°C in a vacuum oven. The interference pattern produced with water in the circular channel when put in a BI configuration is seen in Figure 4.4D. The fringe pattern has a very high frequency component that dominates lower frequencies typically seen with capillary fringe patterns. Upon inspection of the Ni shim by SEM at higher magnifications (Figure 4.4B), it is possible the high frequency component arose from the surface roughness and the deformities present in the shim and thus transferred to the microchip. Another possibility for the presence of the high frequency component is the thickness of the polymer chip (~ 6 mm), since two pieces were bonded together.

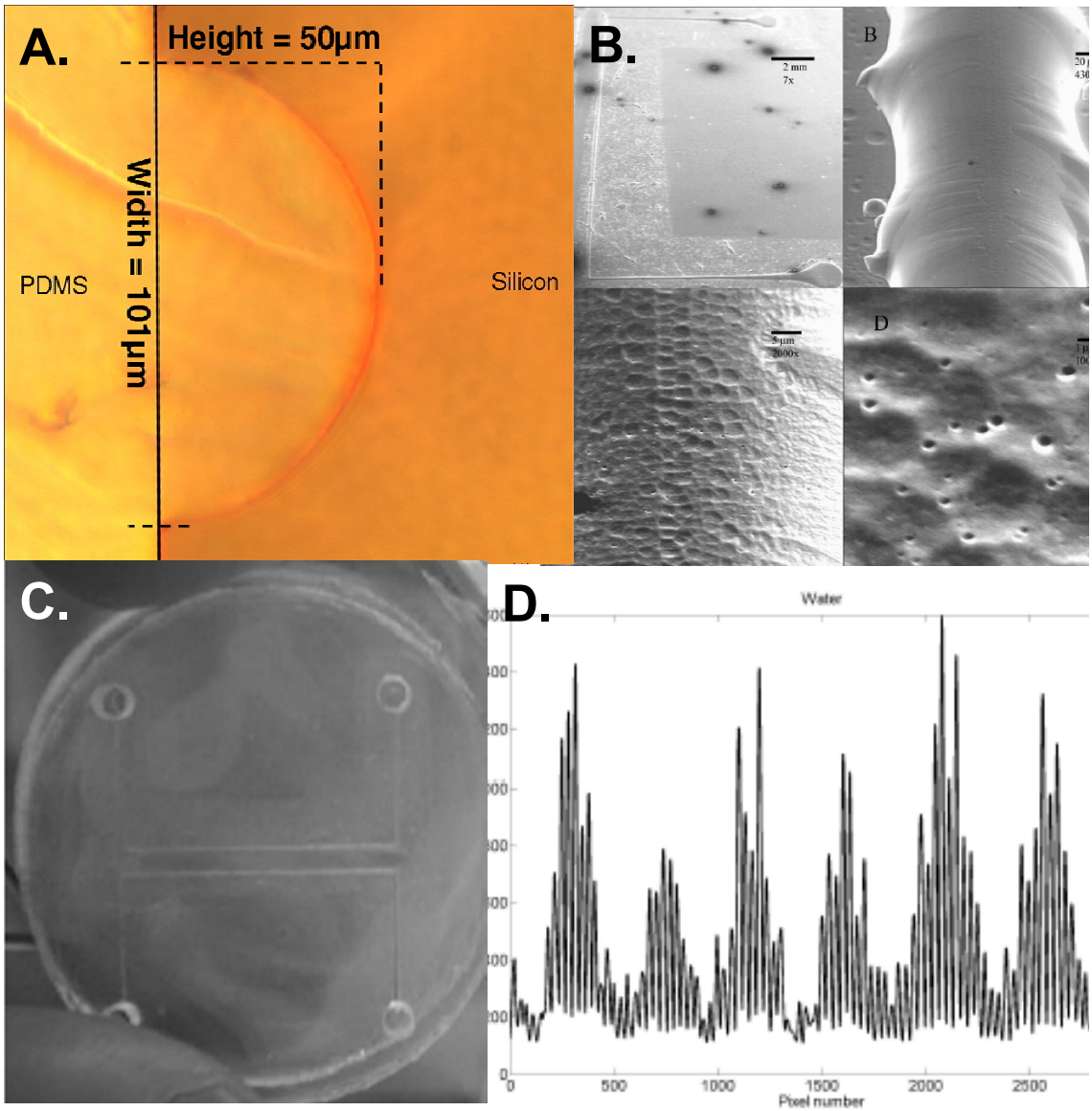

Figures 4.4. An image of PDMS poured into the Si wafer (**A**), SEM pictures taken of the Ni shim at different magnifications (**B**), a two annealed Topas polymer injection molded chips forming a circular channel (**C**) and an interference pattern produced from one of the annealed polymer chips (**D**) is shown.

4.3 Fluidics on the Microscale

Microfluidic devices have enormous potential in biological and chemical sciences through the manipulation of biomolecules in tiny spaces.[10, 12-14] However, in order to create functional microfluidic devices one must first understand the fluidic phenomena that dominate the

microscale. These phenomena can dictate device engineering. Yet understanding of fluidic events on the microscale can help researchers design experiments not possible on the macroscale. A brief introduction into some of the characteristics that are associated with microfluidic flow is given with a focus on in-line mixing for microreactors.

4.3.1 *Background*

In microfluidics, pressure driven flow of liquid is laminar. (Pressure driven flow is the method we use to move fluids about our microdevices and will thus be the only type of flow mentioned.) Laminar flow can be described as adjacent layers of flow with well–defined streamlines. At the fluid–solid interface the speed of the flow is zero, termed a no-slip boundary. The fluid flows in parallel layers, with no disruption between the layers. The flow profile is said to be parabolic. The dimensionless Reynold's number is usually used to describe if the flow is laminar or not. The Reynold's number is given by [15]

$$\mathrm{Re} = \frac{\rho \cdot \nu_s \cdot L}{\eta}, \qquad \text{Eqn. 1}$$

where ν_s is the mean velocity, ρ is fluid density, η is the dynamic fluid viscosity and L is the characteristic length. For circular tubes a Reynold's number under 2300 constitutes a laminar flow. In microfluidics the characteristic length is on the order of microns resulting in Reynold's numbers less than or equal to 50. In this laminar flow regime the only exchange of material between adjacent layers is by diffusion. This means that by introducing one fully miscible liquid into another, the two liquids flows will stay separated[16] for a considerable time period. Diffusion across these adjacent flows takes time as described by Fick's laws. The distance traveled over time by diffusion can be calculated by the Einstein-Smoluchowski equation[17], derived from Fick's first law of diffusion

$$d_{diff} = \sqrt{2 \cdot D \cdot t}, \qquad \text{Eqn. 2}$$

where D is the diffusion coefficient and t is time. Flow systems can be designed like integrated circuits with complete control of the liquid handling[18]. This means that multiple liquid samples can

be introduced into each other with very little consumption of sample. Yet a common challenge is often the rapid and efficient mixing of the samples. Static diffusion of large molecules (e.g. high MW proteins) can take a long time to travel even the small distances associated with microfluidics. Figure 4.5 displays simulations based on Fick's law for the distance traveled by various molecules having different diffusion coefficients.

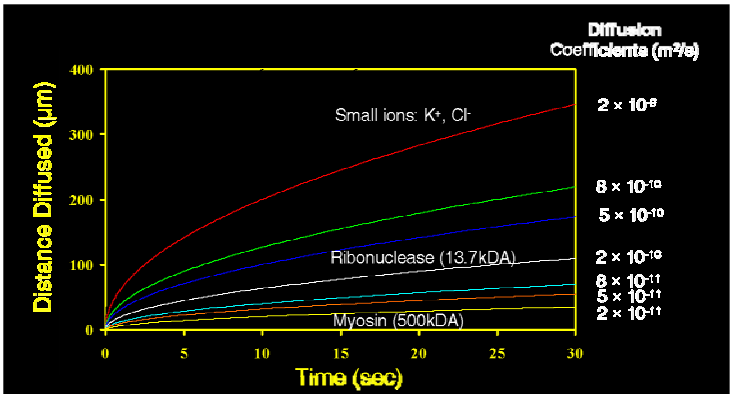

Figure 4.5. Simulated distances different sized molecules diffuse over 30 seconds.

4.3.2 *Mixing in Microchips*

The art of mixing on the microscale is to efficiently maximize the interfacial surface area and concentration gradient. Mixing can be split into two sections, active and passive mixing. Active mixing is when energy from outside the flow system is introduced to the liquid to enhance mixing.[19-23] Active mixing schemes are often difficult to implement into flow systems and require increased fabrication times. Passive mixing uses the flow energy to maximize mixing.[24, 25] Passive mixing is still diffusion based, but as with the creation of eddies the surface area of the liquid plug is increased, thereby decreasing the length needed to diffuse before mixing has occurred.

A fast, efficient, in–line mixer is needed to mix the proteins together as rapidly and as uniformly as possible if free-solution protein binding studies are to be possible. There are two important considerations related to fluid transport of biomolecules in microreactors. First, how completely the complementary proteins interact (i.e. what percentage of sample ends up binding). And second, how much time elapses between the initiation of binding and the initiation of observation (Ideally this time is negligible with the need to measure at the time of mixing). Despite the small length scales involved (less than 100 μm), relying solely on molecular diffusion to produce the necessary molecular interactions could take too long.

Several microfluidic mixing techniques were designed and the applicability to the BI system was investigated. Our objective was to augment diffusion by using different (fixed) channel geometries to produce flows that, in effect, stir the biomolecules together. The effectiveness of using channel geometry to enhance mixing in microscale flows is well documented.[26,27] One straightforward way to accomplish mixing is through 'hydrodynamic focusing'–reducing the channel width drastically, so the channel appears to be squeezed. Preliminary modeling consisted of a two-dimensional representation of a channel that mixes two different solutions with 'hydrodynamic focusing' (Figure 4.6). This channel mixes by constricting the flow (in this case from 70 μm down to 16 μm), which stretches the interface between the two solutions and enables diffusion to more rapidly homogenize the flow. In the results shown, the two solutions enter the mixing channel at the left and flow is from left to right. The initial 70 μm wide channel is 375 μm long. The 16 μm wide center section, 'squeeze', is 200 μm long. And the final 70 μm wide section is 300 μm long. In order to illustrate the mixing, the top incoming stream is assumed to contain a uniform concentration of 'red' molecule with a diffusion coefficient, D=0.5 μm^2/ms. Figure 4.6 shows the distribution of 'red' molecule when the flow rate through the channel was Q=0.2 μL/min, the same order of magnitude as in our experiments (giving 4 mm/s in the constriction). Diffusive mixing in a straight channel is shown for comparison. It is clear that hydrodynamic focusing enhances protein transport across the channel.

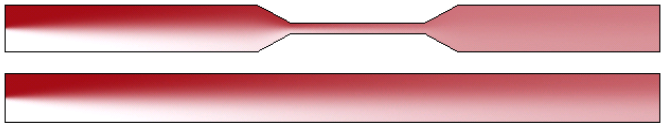

Figure 4.6. Modeled comparison of diffusional mixing with and without a 'squeeze' section.

Figure 4.7 shows the layout of our photolithographic chromium mask, fabricated by DeltaMask (Netherlands) for microreactor devices. This mask has 'hydrodynamic focusing', serpentine, and combined 'hydrodynamic focusing'- serpentine mixers. Serpentine mix due to centrifugal forces encountered at the bend (racetrack effect) leading to a distortion of the laminar flow profile and thus stretching the interfacial surface. Specifically, we have included on the mask 6 diffusion mixers based on 'hydrodynamic focusing', where the flow is focused from 70 μm down

to 8, 12, and 16 μm with constriction lengths of 200 μm and 2 mm, 2 serpentine mixers containing 10 and 20 U-turns connected by a 5 mm long straight channel, and 2 mixers that combine both serpentine and 'hydrodynamic focusing' mixers.

Ultimately, the proteins should be transported into the observation region as quickly as possible. However, as the flow rate through a hydrodynamic system is increased, diffusion has less time to mix the streams and the concentration will be less uniform. Therefore a delicate balance between flow rate, the mixer design and molecules to be investigated must be achieved for the optimization of detection in the BI system during the study of molecular interactions and particularly reaction kinetics.

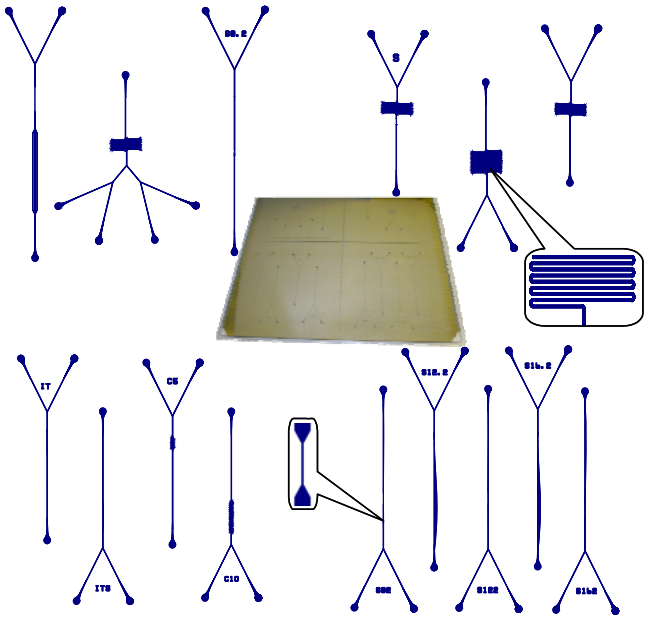

Figure 4.7. Mixer designs and the chrome mask are shown.

4.4 Summary

The fabrication of planar channel structures was easily achieved by a combination of optical and soft lithography. The use of a common negative resist exposed at the required wavelength, gave rise to well defined relief structures on a master device. Microfluidic chips molded in PDMS provided excellent versatility for rapid prototyping. This fact was especially useful when investigating the different mixer designs. Following numerous experimental observations with different PDMS micromixers, a serpentine-squeeze hybrid mixer was selected to carry out the molecular interaction studies. By slight manipulations of the flow rate, mixing

artifacts could be teased out of the system while molecules could be brought into near proximity for the observation of binding by BI.

The fabrication of semi-circular channels in a polymeric substrate was also realized. This process allows for high throughput production of highly sensitive channel designs by injection molding. However, processes such as Si_3N_4 deposition and mask opening need further optimizing in order to reduce pinholes and surface roughness. Unfortunately, the semi-circular device was fabricated too late in the process to incorporate into any experiments. All binding assays were instead performed using rectangular channels molded in PDMS.

(1) Campbell, S. *The Science and Engineering of Microelectronic Fabrication*; Oxford University Press: New York, 1996.

(2) Xia, Y. N.; Whitesides, G. M. *Annual Review of Materials Science* **1998**, *28*, 153-184.

(3) LaBianca, N.; Gelorme, J. *SPIE* **1995**, *2438*, 846-852.

(4) Wilbur, J. L.; Kumar, A.; Kim, E.; Whitesides, G. M. *Advanced Materials* **1994**, *6*, 600-604.

(5) Kumar, A.; Abbott, N. L.; Kim, E.; Biebuyck, H. A.; Whitesides, G. M. *Accounts of Chemical Research* **1995**, *28*, 219-226.

(6) Xia, Y. N.; Zhao, X. M.; Whitesides, G. M. *Microelectronic Engineering* **1996**, *32*, 255-268.

(7) Lee, J. N.; Park, C.; Whitesides, G. M. *Analytical Chemistry* **2003**, *75*, 6544-6554.

(8) Sorensen, H. S.; Larsen, N. B.; Latham, J. C.; Bornhop, D. J.; Andersen, P. E. *Applied Physics Letters* **2006**, *89*, -.

(9) Markov, D. A.; Swinney, K.; Bornhop, D. J. *Journal of the American Chemical Society* **2004**, *126*, 16659-16664.

(10) Thorsen, T.; Maerkl, S. J.; Quake, S. R. *Science* **2002**, *298*, 580-584.

(11) Fan, Z. H.; Harrison, D. J. *Analytical Chemistry* **1994**, *66*, 177-184.

(12) Werdich, A. A.; Lima, E. A.; Ivanov, B.; Ges, I.; Anderson, M. E.; Wikswo, J. P.; Baudenbacher, F. J. *Lab on a Chip* **2004**, *4*, 357-362.

(13) Prokop, A.; Prokop, Z.; Schaffer, D.; Kozlov, E.; Wikswo, J.; Cliffel, D.; Baudenbacher, F. *Biomed Microdevices* **2004**, *6*, 325-339.

(14) Anderson, M. J.; Hansen, C. L.; Quake, S. R. *Proceedings of the National Academy of Sciences of the United States of America* **2006**, *103*, 16746-16751.

(15) Hubbard, D. S.; Houlne, M. P.; Kiefer, G.; Janssen, H. F.; Hacker, C.; Bornhop, D. J. *Lasers in Medical Science* **1998**, *13*, 14-21.

(16) Bains, G.; Freire, E. *Analytical Biochemistry* **1991**, *192*, 203-206.

(17) Bornhop, D. J.; Contag, C. H.; Licha, K.; Murphy, C. J. *Journal of Biomedical Optics* **2001**, *6*, 106-110.

(18) Torres, F. E.; Kuhn, P.; De Bruyker, D.; Bell, A. G.; Wolkin, M. V.; Peeters, E.; Williamson, J. R.; Anderson, G. B.; Schmitz, G. P.; Recht, M. I.; Schweizer, S.; Scott, L. G.; Ho, J. H.; Elrod, S. A.; Schultz, P. G.; Lerner, R. A.; Bruce, R. H. *Proc Natl Acad Sci U S A* **2004**, *101*, 9517-9522.

(19) West, J.; Karamata, B.; Lillis, B.; Gleeson, J. P.; Alderman, J.; Collins, J. K.; Lane, W.; Mathewson, A.; Berney, H. *Lab on a Chip* **2002**, *2*, 224-230.

(20) Yang, Z.; Matsumoto, S.; Goto, H.; Matsumoto, M.; Maeda, R. *Sensors and Actuators a-Physical* **2001**, *93*, 266-272.

(21) Liu, R. H.; Lenigk, R.; Druyor-Sanchez, R. L.; Yang, J. N.; Grodzinski, P. *Analytical Chemistry* **2003**, *75*, 1911-1917.

(22) Qian, S. Z.; Bau, H. H. *Analytical Chemistry* **2002**, *74*, 3616-3625.

(23) Paik, P.; Pamula, V. K.; Fair, R. B. *Lab on a Chip* **2003**, *3*, 253-259.

(24) Schwesinger, N.; Frank, T.; Wurmus, H. *Journal of Micromechanics and Microengineering* **1996**, *6*, 99-102.

(25) Lee, G. B.; Chen, S. H.; Huang, G. R.; Sung, W. C.; Lin, Y. H. *Sensors and Actuators B-Chemical* **2001**, *75*, 142-148.

(26) Whitesides, G. M.; Stroock, A. D. *Physics Today* **2001**, *54*, 42-48.

(27) Liu, R. H.; Stremler, M. A.; Sharp, K. V.; Olsen, M. G.; Santiago, J. G.; Adrian, R. J.; Aref, H.; Beebe, D. J. *Journal of Microelectromechanical Systems* **2000**, *9*, 190-197.

CHAPTER V

SIGNAL INTERPRETATION AND DATA ANALYSIS

5.1 Manifestation of the Interference Pattern

The interference pattern in BI is solely produced by the microchip architecture and the fluid it contains, hence the amount of effort given to optimize fabrication (*see Chapter IV*). Any changes to either component will result in a change to the interference pattern.[1-23] The BI technique has been modeled by multiple methods, all of which simulate a high contrast interference pattern that is dependant upon both the channel geometry and composition, further verifying experimentally observed results.[8, 9, 14, 15, 22]

The interference pattern itself is produced by the interaction of light waves with the structure, interfaces, and fluids of the microfluidic chip. Incident light waves experience reflection, refraction, and diffraction during propagation through the microchip as well as possible scattering from fluid content or surface roughness. Simulations of the light propagation through the BI system have shown both the surface and fluid within the microchannel are interrogated several times by numerous passes of light. BI sensitivity to changes in the optical pathlength brought

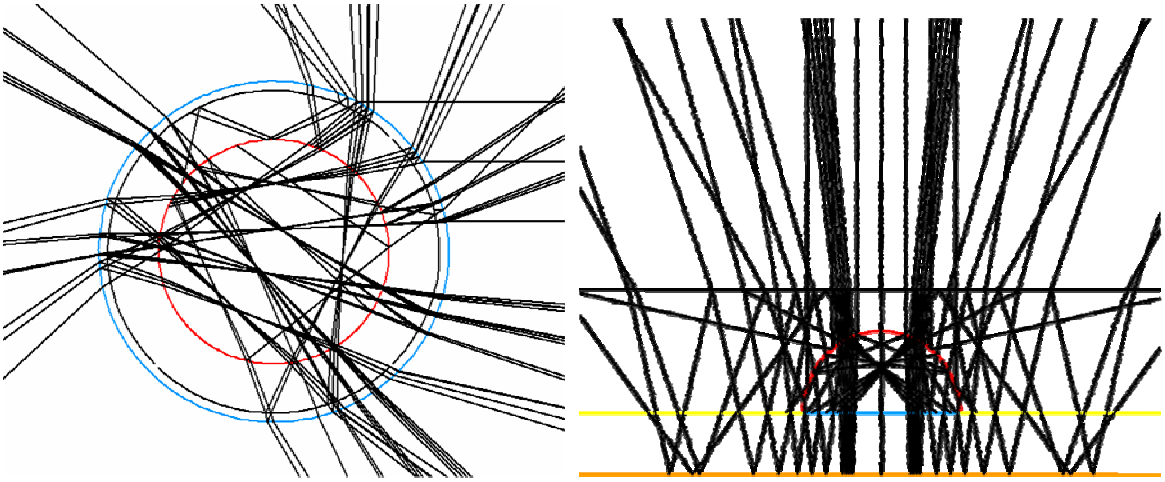

Figure 5.1. Simulations of the multi-pass aspect of light waves in the BI system for circular and semi-circular geometries are shown.[14, 15]

about by any changes to the media or channel structure/topology is greatly enhanced by the multi-pass aspect.

The multi-pass component of BI is easily understood in the capillary or semi-circular embodiments. There the curved surface acts like a lens focusing waves of light into the center of the flow channels. The waves interact with the fluid and the channel surface, being reflected and refracted repeatedly. A closer look at earlier modeling studies predicts this behavior in circular and semi-circular channel structures (Figure 5.1). What seems less obvious is the high contrast interference pattern produced experimentally when using planar/rectangular channel geometries (Figure 5.2). In fact, ray tracing approaches at modeling light propagation through a BI system with rectangular geometry show no interference at all. Early investigations into the manifestation of such well defined constructive and destructive interference led us to believe the high contrast interference pattern is produced by diffraction at the corners of the rectangular channels. In close

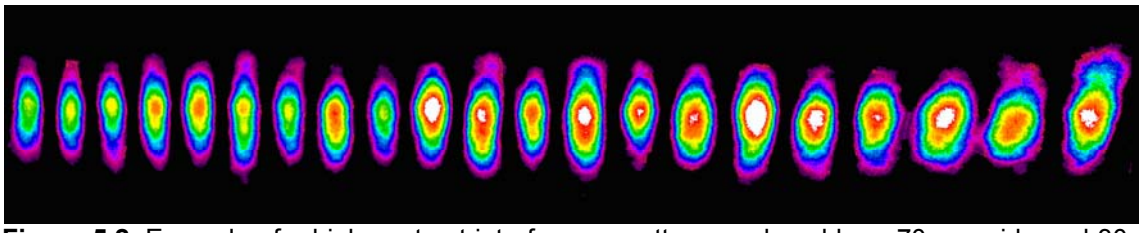

Figure 5.2. Example of a high contrast interference pattern produced by a 70 μm wide and 30 μm tall rectangular channel in the BI system captured with a laser beam analyzer (LBA).

collaboration with Dr. Florian Forster (formerly of Lund University, Lund, Sweden) the system was modeled in a Finite-Difference Time-Domain (FDTD) model. The model propagates a beam in incremenatal steps through the entire BI system, requiring extensive computation times. Limited results were obtained with Dr. Forster, but confirmation to our earlier hypothesis was validated. The pattern did arise from light diffraction of the corners of the rectangle, in particular the two bottom corners where the polymer, glass slide, and liquid reach an interface.

5.2 Interrogation of the Interference Pattern

Several approaches have been used previously in the BI system for spatial fringe position analysis. Early investigations saw use of a PIN photodiode and a precision air slit. Here the detector was positioned on a single fringe near $1/e^2$ intensity. Movement of the fringe could then be detected by a change in voltage. As the apex of the fringe (considering a Gaussian shape) moved toward the detector the voltage would increase with a linear response. This approach was later refined with a small avalanche photodiode[19] and reference arm[22] capabilities increasing sensitivity. Detector positioning was a drawback to this transducer as well as source instability. Since the displacement of the interference pattern was measured indirectly by light intensity, any change in intensity caused by the source or environment would indicate an erroneous fringe displacement. Other methods such as a CCD camera with a laser beam analyzer (LBA)[10] and a bicell[23] were also attempted. However, these approaches were also limited by the interrogation of a single fringe and showed no significant progress in sensitivity.

A concerted effort was then made to interrogate multiple fringes in order to increase detection limits. Markov, *et.al*[24] demonstrated the use of a linear CCD array with appropriate computational algorithms was well suited for the detection of multiple interference fringes produced in the BI system. Directing multiple fringes onto the CCD array promotes signal averaging and enhanced S/N results. Since the CCD is a large area device, three to upwards of 12 fringes from the interference pattern can be used, eliminating the need to align the slit-

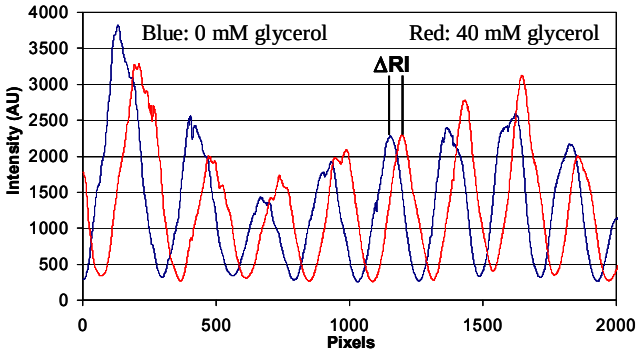

Figure 5.3. Spatial movement of the interference pattern is shown by altering the optical pathlength of light through the system, in this case changing the refractive index of the solution. The shape and periodicity of the intensity profile remain appreciably unchanged by small changes to the optical pathlength.

photodetector with respect to $1/e^2$ intensity on a particular fringe. A comparison of the different transducers used is given in Table 5.1. *(The CCD w/Fourier Analysis method is used in all applications presented in Chapter VI)*

Since the shape and pitch of the fringes did not change appreciably with small changes to the optical pathlength (Figure 5.3) the intensity profile can be viewed as a spatially varying signal. Any lateral shift of the interference pattern detected by the linear CCD array can be viewed as the original signal with an added phase shift. Therefore, Fourier analysis techniques can be applied to quantify the added phase and thus positional shifts to the interference pattern.

Briefly, a Fourier transform of the fringe pattern profile collected by a CCD array gives one peak in the Fourier domain corresponding to the spatial frequency of the fringe pattern. In BI, this phase is calculated as: φ = arctan (Im/Re), where *Re* and *Im* are real and imaginary components of the FT corresponding to the fringe spatial frequency. Since the arctan(•) is defined on the interval of $(-\frac{1}{2}\pi; \frac{1}{2}\pi)$ the sign ambiguity can be addressed by looking simultaneously at the signs of both real and imaginary parts of the FT and by adding, when necessary, a value of π to the calculated φ thus obtaining estimation of the signal spatial phase in the range of $(0; 2\pi)$.

Through the integration of the FFT function directly into the CPU core, Fourier transform calculations are performed rapidly allowing BI phase changes to be quantified and displayed in real-time at speeds up to 200 Hz in a custom designed graphical user interface (GUI). Briefly, voltage from the CCD is digitized by the A/D converter on the interface card and passed to the CPU. A DLL (dynamic linked library) supplied by Ames Photonics was used to fetch this data. A custom software program utilizing

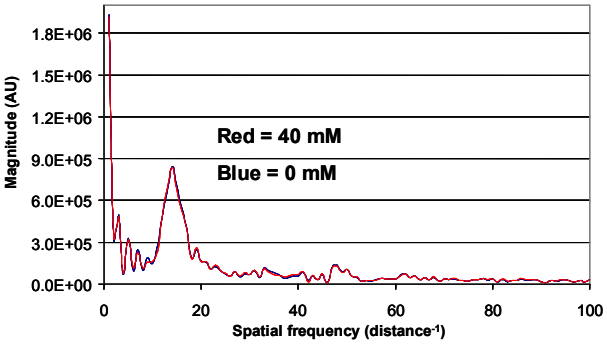

Figure 5.4. Presented here is the FFT magnitude spectrum of the two fringe profiles displayed in Figure 5.3. The fact that the shape and periodicity of the fringe pattern does not change appreciably with small variations in the optical pathlength is further demonstrated here by the fact both fringe patterns have the same spatial frequency.

Intel's Math Kernel Library allows access to processor level functions and thus the ability to perform calculations at CPU core speed.

Table 5.1. Comparison of the sensitivity of different interrogation methods used in BI.

Interrogation Method	Detection Limit (RIU)
Bicell	**4×10^{-6}**
slit-photodetector w/reference arm	**1.5×10^{-7}**
CCD w/ LBA	**5×10^{-5}**
CCD array w/minimum tracking	**6.7×10^{-6}**
CCD array w/Fourier phase analysis	**7×10^{-8}**

5.3 Data Analysis

Fourier analysis of an interference pattern gives a phase value specific to that pattern as described above. Initially, this Fourier analysis approach was performed offline since the custom program and GUI had not yet been implemented. In this case, single spectra of the interference pattern were taken, each having been produced from a known fluid and surface topology. Relative signals could be compared by monitoring each pattern's individual phase value taken from the same frequency in the magnitude spectrum to monitor positional changes in the interference pattern.

Surface chemistry experiments were performed in such a manner.[4] Once a molecule had been attached to the channel surface, buffer was introduced and the interference pattern was recorded. The immobilized molecule could then be interrogated with a solution containing either a potential binding partner or control. The solution would then be rinsed from the channel and buffer was again added. The interference pattern was recorded and the phase value obtained was compared relative to the value calculated when just the initial molecule was immobilized on

the surface. Changes in the phase value were attributed to binding events having taken place, thus altering the affinity layer on the channel surface. Increasing concentrations of the binding partner solution would be introduced and a linear response was obtained until saturation was reached.

Saturation binding experiments are important to us as they allow for the determination of the equilibrium dissociation constant (K_D), a measure of binding affinity and thus a description of the molecular interaction.[25] Based on the *law of mass action* and assuming the reaction reached equilibrium, the maximum binding signal, Y, (calculated as the relative change in phase) can be plotted versus the concentration (X) of the binding partner (ligand, substrate, etc.). This saturation curve can be fit to the equation

$$Y = \frac{B_{MAX} \cdot X}{X + K_D}, \qquad \text{Eqn. 1}$$

where B_{MAX} represents the maximum saturation density. Routine fitting software can be used to determine B_{MAX}, K_D and their uncertainties at any confidence interval. Saturation binding experiments, also called end point analysis or steady-state binding, are routinely used for the determination of K_D.

The fractional occupancy can also be determined in a similar manner assuming the reaction is governed by the law of mass action at equilibrium. For a reversible bimolecular reaction where A (immobilized molecule) and B (binding partner) react to form C (product) the fractional occupancy (Θ) of A is given by

$$\Theta = \frac{[C]}{[A]+[C]}. \qquad \text{Eqn. 2}$$

Substitution and rearrangement of Eqn. 2 using

$$K_D = \frac{[A]\cdot[B]}{[C]}, \qquad \text{Eqn. 3}$$

gives the fractional occupancy as

$$\Theta = \frac{[C]}{[A]+[C]} = \frac{([A]\cdot[B])/K_D}{[A]+([C]/K_D)} = \frac{[B]}{[B]+K_D}. \qquad \text{Eqn. 4}$$

The law of mass action model does make certain assumptions:

- all binding sites are equally accessible
- molecules are either free or bound
- no partial binding states are allowed
- binding does not alter the molecular species
- binding is reversible

Also, when binding occurs to an immobilized molecule there is no assumed lateral interaction between adsorbed species, the surface is assumed to be homogeneous, and the maximum binding allowed is a monolayer. Furthermore, neither the fractional occupancy nor saturation binding equations take into account ligand depletion with each assuming excess amounts of ligand. In fact, experiments are generally run at high ligand concentrations to ensure no ligand depletion. Alternative approaches have been taken to calculate K_D values from steady-state binding experiments where ligand depletion was answered for.[26, 27]

Through the implementation of our custom designed software, BI is now able to monitor surface reactions or free-solution interactions in real-time, sampling phase from a monitored frequency of the interference pattern at rates up to 200 Hz. Monitoring kinetics can offer further details about molecular interactions (rates of association and dissociation) while also providing an intra system corroboration of results obtained from steady-state analyses. Kinetic analysis can be used to monitor possible transition states as well as avoid potential inadequacies that can be associated with steady-state experiments as demonstrated in Figures 5.5. Finite element differencing was used to simulate binding curves with equivalent equilibrium data. The two graphs show markedly different kinetics, but the same equilibrium binding parameters. Thus a steady-state experiment would observe these systems as identical, unable to distinguish between two systems having the same K_D and n values, but vastly different on and off rates.

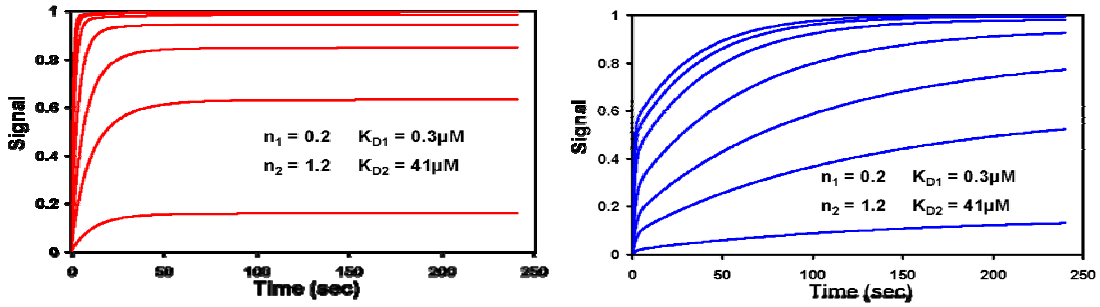

Figure 5.5. Kinetic simulations using finite element differencing are shown. Both interactions have the same equilibrium binding parameters and would thus be perceived as identical by steady-state analysis. However, as the kinetic traces exhibit, the two systems are very dissimilar.

A first attempt at analyzing kinetic data recorded during BI experiments was made. Since two reactants are mixed on-chip in solution phase BI molecular interactions, a quantitative solution to a generic, bimolecular reversible reaction was accomplished by the derivation of a first order, ordinary differential equation (ODE). The generic reaction is presented below

$$\mathbf{[R] + [L] \underset{k_2}{\overset{k_1}{\rightleftharpoons}} [R{\bullet}L]} \quad \text{Eqn. 5}$$

where k_1 and k_2 are the on and off rates respectively, $[R]$and $[L]$ are the concentrations of the two reactant species and $[R \bullet L]$ is the concentration of the product formed. Association of the reaction at any time, t, proceeds as $[R]_t \cdot [L]_t \cdot k_1$ while the reversible dissociation of the product progresses by $[R \bullet L]_t \cdot k_2$. The net rate of this reaction is defined by

$$\frac{d[R \bullet L]}{dt} = [R]_t \times [L]_t \times k_1 - [R \bullet L]_t \times k_2 . \quad \text{Eqn. 6}$$

Assuming $[L] > [R]$, we find that the initial concentration of L remains relatively unchanged at equilibrium or $[L]_0 \cong [L]_{eq}$ and thus $[L]$ can be treated as a constant. By the law of mass action, the amount of free $[R]$ at any time, t, can be expressed by the difference in the initial concentration of $[R]$ and any amount lost during the formation of the product by Equation 7

$$[R]_t = [R]_0 - [R \bullet L]_t . \quad \text{Eqn. 7}$$

Substitution of the expression for free $[R]$ (Eqn. 7) into Equation 6 coupled with the fact the concentration of $[L]$ can be treated as a constant yields

$$\frac{d[R \bullet L]}{dt} = ([R]_0 - [R \bullet L]_t) \times [L]_0 \times k_1 - [R \bullet L]_t \times k_2 . \quad \text{Eqn. 8}$$

Multiplying through and rearranging we generate

$$\frac{d[R \bullet L]}{dt} + (k_1 \cdot [L]_0 + k_2) \cdot [R \bullet L]_t = [R]_0 \times [L]_0 \times k_1 . \quad \text{Eqn. 9}$$

Equation 9 represents a first order, ordinary differential equation (ODE) of the form

$$y' + p(x)y = r(x) . \quad \text{Eqn. 10}$$

This 1st order ODE has the general solution

$$y(x) = e^{-h} \cdot [\int e^h \cdot r \cdot dx + c] \quad \text{Eqn. 11}$$

where $h = \int p(x)dx$.[28] Substituting Equation 9 into the form of this general solution leaves us with

$$[R \bullet L]_t = e^{-\int (k_1 \cdot [L]_0 + k_2)dt} \cdot [\int e^{\int (k_1 \cdot [L]_0 + k_2)dt} \cdot [R]_0 \cdot [L]_0 \cdot k_1 \cdot dt + c] . \quad \text{Eqn. 12}$$

Integration of Equation 12 yields

$$[R \bullet L]_t = e^{-(k_1 \cdot [L]_0 + k_2) \cdot t} \cdot (\frac{e^{(k_1 \cdot [L]_0 + k_2) \cdot t} \cdot [R]_0 \cdot [L]_0 \cdot k_1}{k_1 \cdot [L]_0 + k_2} + c) . \quad \text{Eqn. 13}$$

Multiplying through Equation 13 and canceling terms gives us the general solution to Equation 9 as

$$[R \bullet L]_t = \frac{[R]_0 \cdot [L]_0 \cdot k}{k_1 \cdot [L]_0 + k_2} + c \cdot e^{-(k_1 \cdot [L]_0 + k_2) \cdot t} . \quad \text{Eqn. 14}$$

Boundary conditions must be imposed to solve for the constant, c. At the initial starting point, $t = 0$, no product exists, such that $[R \bullet L]_0 = 0$. At $t = \infty$, the product concentration is at equilibrium and has achieved its maximum value, $[R \bullet L]_\infty = [R \bullet L]_{eq} = [R \bullet L]_{MAX}$. Applying the first boundary condition to Equation 14 provides a value for the constant, c , by

$$[R \bullet L]_0 = 0 = \frac{[R]_0 \cdot [L]_0 \cdot k_1}{k_1 \cdot [L]_0 + k_2} + c \cdot e^{-(k_1 \cdot [L]_0 + k_2) \cdot 0} = \frac{[R]_0 \cdot [L]_0 \cdot k_1}{k_1 \cdot [L]_0 + k_2} + c \cdot e^0 . \qquad \text{Eqn. 15}$$

Since $e^0 = 1$, c is thus equal to

$$c = -(\frac{[R]_0 \cdot [L]_0 \cdot k_1}{k_1 \cdot [L]_0 + k_2}) . \qquad \text{Eqn. 16}$$

By applying the second boundary condition, an expression for the maximum value of product can be found by

$$[R \bullet L]_\infty = \frac{[R]_0 \cdot [L]_0 \cdot k_1}{k_1 \cdot [L]_0 + k_2} + c \cdot e^{-(k_1 \cdot [L]_0 + k_2) \cdot \infty} = \frac{[R]_0 \cdot [L]_0 \cdot k_1}{k_1 \cdot [L]_0 + k_2} + c \cdot e^{-\infty} . \qquad \text{Eqn. 17}$$

The exponential function raised to negative infinity is equal to zero. Therefore the second term of Equation 17 cancels out and the maximum value of binding is given by

$$[R \bullet L]_\infty = [R \bullet L]_{eq} = [R \bullet L]_{MAX} = \frac{[R]_0 \cdot [L]_0 \cdot k_1}{k_1 \cdot [L]_0 + k_2} . \qquad \text{Eqn. 18}$$

This evaluation is further verified by Atkins and de Paula.[29] Substitution of the expression found for the constant (Eqn. 16) into the general solution of Equation 14 yields

$$[R \bullet L]_t = \frac{[R]_0 \cdot [L]_0 \cdot k_1}{k_1 \cdot [L]_0 + k_2} - \left\{ \frac{[R]_0 \cdot [L]_0 \cdot k_1}{k_1 \cdot [L]_0 + k_2} \cdot e^{-(k_1 \cdot [L]_0 + k_2) \cdot t} \right\} . \qquad \text{Eqn. 19}$$

Simple algebra allows for the collection of terms producing

$$[R \bullet L]_t = \frac{[R]_0 \cdot [L]_0 \cdot k_1}{k_1 \cdot [L]_0 + k_2} \cdot \left(1 - e^{-(k_1 \cdot [L]_0 + k_2) \cdot t}\right) . \qquad \text{Eqn. 20}$$

Substitution of Equation 18 into the previous equation gives rise to

$$[R \bullet L]_t = [R \bullet L]_{MAX} \cdot \left(1 - e^{-(k_1 \cdot [L]_0 + k_2) \cdot t}\right) . \qquad \text{Eqn. 21}$$

Equation 21 represents a single exponential of the general form, $y = a(1 - e^{-\tau x})$. Non-linear least squares fitting of kinetic traces for molecular interactions detected during BI experiments to this general form allows extraction of quantitative data. While the value of a defines the maximum product formed, evaluation of τ permits the determination of binding affinity for the molecular interaction. The value of τ, often called the observed rate (k_{obs}), is equal to,

$k_1 \cdot [L]_0 + k_2$ from Equation 21. Plotting the observed rate, τ, determined from multiple kinetic traces with varied initial concentrations of L should exhibit a linear relationship over the concentration range (Figure 5.6). Substitution of k_{obs} into the equation of a straight line, $y = mx + b$, where here $y = k_{obs}$, yields $k_{obs} = k_1 \cdot [L]_0 + k_2$. The slope of the line, m, corresponds to k_1. The initial concentration of L for each kinetic trace is equivalent to x, and the y-intercept, b, is the same as k_2. Since $K_D = \frac{k_2}{k_1}$, the y-intercept divided by the slope of the best fit line for the graph of k_{obs} versus $[L]_0$ can be used to determine the equilibrium dissociation constant.

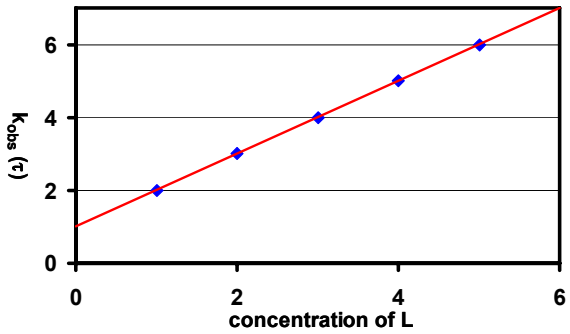

Figure 5.6. Expected linear relationship of the observed rate versus the initial concentration of L.

5.4 Noise Assessment and Error Analysis

Analytical detection methods are often described by figures of merit that quantitatively characterize the performance of the instrument. Among these figures of merit, sensitivity and detection limit are exceedingly important in determining the suitability of an analytical technique for a given problem. The capability of an instrument to discriminate between small amounts of analyte is defined as sensitivity whereas the detection limit of the instrument is the minimum amount of analyte that can be sensed.[30] More specifically, analytical sensitivity, γ, is limited by the standard deviation in the measurement, s_s, by the equation

$$\gamma = \frac{m}{s_s}, \qquad \text{Eqn. 22}$$

where m is the slope of a calibration curve. Since analytical sensitivity is dependant upon the standard deviation in the measurements it also is a *de facto* measure of precision. Detection limits (DL) for analytical instruments are generally accepted to be a minimum concentration or mass of analyte that can be detected at a known confidence level. The minimum detectable signal is contingent upon the magnitude of the analytical signal being larger than a control or blank signal by some factor of the variation in the control signal. This is commonly referred to as a signal to noise ratio, denoted S/N. The minimum detectable signal, S_m, can be determined from measurements of a control sample, $S_{control}$, and uncertainties associated with those measurements, $s_{control}$, by the equation

$$S_m = S_{control} + k \cdot s_{control}, \qquad \text{Eqn. 23}$$

where k is a chosen multiple of the deviation in the measurement. Three is most often chosen as the multiple k, representing an ~99% confidence level of detection. The S_m value calculated in Equation 23 can be converted to a mass of concentration detection limit in conjunction with a simple calibration curve. The value obtained in choosing k = 3, is typically represented as a three sigma detection limit or 3σ DL.

All measurements made by analytical instruments consist of two components: signal and noise. The signal carries information relative to the analyte. Noise however consists of superfluous information unrelated to the analyte. As seen above, noise in the measurement increases imprecision and limits the amount of analyte that can be detected, drastically diminishing the performance of an analytical instrument. Multiple sources of noise exist in the BI system. Recorded fringe patterns exhibit noise that manifests itself as irregular contours in each fringe. Some of this noise is due to temporal fluctuations in the light intensity captured by the CCD. True spatial noise in the fringe pattern is associated with: non-uniformities in the laser beam, heterogeneities in the microchip structure, or concentration and RI gradients within the sample.

Shot noise and Johnson noise, both types of white noise, present as high frequency fluctuations in the phase signal output of the BI system. The primary source of white noise in the

BI system is at the CCD array. There thermal agitation of the electrons produced by light striking the linear array of silicon photodiodes and the transfer of these electrons across p-n junctions creates current and voltage fluctuations that appear in the signal readout. Random fluctuations in laser intensity also contribute to high frequency noise components. High frequency environmental noise adds yet another cause of imprecision with electrical components of the BI system picking up electromagnetic radiation from various external sources.

Low frequency noise ($1/f$) is problematic for the BI system, reducing stability over time in the form of long-term drift. Low frequency noise, often called flicker noise, arises from optical and mechanical parameters that define the interference pattern and becomes significant at frequencies less than 100 Hz. Two contributing low frequency noise sources in the BI system are mechanical instability of the mirror and/or light source as well as gradual drift in laser output arising from plasma noise and tube heating. However, the principal source of low frequency drift is environmental noise, specifically gradual temperature fluctuations. The refractive index of liquids is highly dependant upon temperature with a change of 1°C resulting in the RI of water altered by 0.01% (i.e. $\frac{\partial \eta_{H_2O}}{\partial T} \cong 1 \times 10^{-4} / °C$). Temperature stability around 0.01°C fundamentally confines BI detection limits to 1×10^{-6} RIU.

Signal averaging can help to minimize high frequency sources of noise, therefore the spectral intensity in BI experiments is integrated over 100 – 500 μsec. With that said, the signal quality during BI experiments is quite good with respect to high frequency noise as the root-mean-square noise (rms) is typically around 0.001 phase units over a one to two second period. This value can be lowered even further by digital filtering (low-pass) the signal output. Efforts to negate low frequency sources of noise are commonly employed for BI experiments. Mechanical and structural vibrations are reduced due to BI components being mounted on isolated optical breadboards. The optics labs in Dr. Bornhop's group at Vanderbilt University constantly regulate temperature within the 0.01°C range with individual units positioned above each optical breadboard. Further temperature stability is gained by an additional unit controlling the microchip mount. A Melcor MTCA-6040 60W temperature controller was used in BI experiments presented

in *Chapter VI* to serve in this function. The Melcor instrument provides another order of magnitude in attainable detection limits by increasing temperature control to one millidegree Centigrade resulting in a fundamental detection limit of 1×10^{-7} RIU. A measure of the low frequency noise and drift in BI experiments can be made by looking at the steady-state signal. Plotting the last 10 – 15 seconds of experiments performed in *Chapter VI* (when dynamic equilibrium has been reached) yields statistically flat lines with slopes in the range of 1×10^{-4} – 1×10^{-5}. Even at these instrumental noise levels, BI can routinely detect attomole (10^{-18}) quantities of analyte.

Measurements made by analytical instruments also have some degree of uncertainty associated with them termed experimental error. One of the two types of experimental error is reproducible upon repetition of the experiment under invariable conditions. Termed systematic or determinate error, this error introduces a bias into the measurement. However, systematic error can in principle be exposed and corrected by various approaches whether that be alteration of the experimental design, calibration curves, etc. Molecular interaction assays performed by BI have only two distinguishable determinate errors: mixing artifacts and baseline drift with increasing amounts of free ligand at high concentrations. In-line mixing of control compounds within the microchip produce a signal ($S_{control}$) across a range of concentrations with a relatively constant magnitude. Since the magnitude of this signal is constant regardless of concentration it can be subtracted out as background noise. The other systematic error is only problematic at high concentrations (≥ high μM) of larger molecular weight constituents. At such concentrations, excess ligand causes the starting point of the molecular interaction to shift linearly. A calibration curve of the ligand can therefore be used to baseline subtract this offset.

The other type of experimental error is termed random or indeterminate with its name aptly describing its characteristics. Indeterminate error occurs due to uncontrollable elements in the measurement. Random error creates both positive and negative fluctuations in the measurement at near equivalent rates of recurrence. Unlike systematic error, random error cannot be eliminated from the measurement rather reduced by better experimental design. The high frequency and low frequency noise components discussed above are examples of random

error. Unchecked these fluctuations would mask any true signal measured during BI experiments. However, with the proper design and implementation random noise can be effectively minimized allowing for the excellent sensitivity capable from the BI instrument.

As stated in *Section 5.3*, kinetic traces for molecular interactions detected during BI experiments are fit to a single exponential of the form $y = a(1-e^{-\tau x})$. A nonlinear least squares regression algorithm is used to analyze kinetic data and is easily accessible by multiple programs including SigmaPlot, Origin, Prism, etc. Nonlinear regression uses iterative optimization procedures to compute the parameters a and τ for each molecular interaction curve. Since nonlinear least squares regression is an iterative process, initial values for each parameter must be entered. These starting values must be reasonably close to undetermined parameters or the optimization procedure may not converge. Poorly chosen initial values can cause the fitting routine to converge at a local minimum rather than the global minimum that defines the least squares estimates. The parameters calculated by the fitting routine have some uncertainty associated with their 'goodness of fit'. The uncertainty (or residual) in a and τ for molecular interactions performed in *Section 6.2* were roughly 10^{-4} and 10^{-3} respectively. The parameter a describes the asymptotic region of the binding curve where steady-state conditions have been reached. With that being said, the residuals of a are a reflection of the low frequency noise discussed earlier and it should be noted that these values are similar in magnitude. The parameter τ defines the shape of the exponential rise in the molecular interaction trace. The uncertainties in τ are one order of magnitude greater than those of a due primarily to its increased dependency on high frequency noise components at times near zero. The high frequency noise component of the BI system is ~10^{-3} corresponding to the residuals of τ, indicating the accuracy of observed rate constants are limited by high frequency noise.

Once a, τ, and their uncertainties have been calculated, these parameters can be used to calculate the equilibrium dissociation constant of any molecular interaction studied as described in *Section 5.3*. An end point analysis can be performed by plotting a versus the concentration of ligand which will exhibit a hyperbolic relationship. This plot is then fit to Equation 1 by any of the aforementioned analysis programs resulting in quantitation of K_D. As with the

analysis of kinetic data, end point analyses are also fit by nonlinear least squares regression techniques. The computed K_D value will thus have a degree of uncertainty associated with it. As K_D is determined with respect to a in saturation binding experiments, the error in a is propagated through the calculation of K_D as described by Harris[31]. Furthermore, the use of algorithms in fitting software enables the determination of K_D at any desired confidence quickly and efficiently.

As stated in *Section 5.3*, plotting the observed rate constant, τ, as a function of ligand concentration produces a linear relationship. The slope of the line corresponds to the on-rate for the molecular interaction while the y-intercept is linked to the off-rate of the reaction. Linear least squares analysis is used to obtain an analytical solution for a 'best fit' line through the rate data as well as the error in slope and y-intercept of the line (and thus the error in K_D). The method of linear least squares is a widely used technique for fitting linear data. Linear least squares regression assumes there is no error in abscissa values and there is error only in the ordinate. Furthermore, the error in the τ values is presumed to be distributed evenly about the value (Gaussian) and the errors across all τ values in a set are consistent. Outliers in the data greatly affect the variance of the best fit line by their failure of the last assumption.

Linear least squares regression[31] determines the slope (m) of the best fit line through any data set by

$$m = \frac{\begin{vmatrix} \sum (x_i y_i) & \sum x_i \\ \sum y_i & n \end{vmatrix}}{\begin{vmatrix} \sum (x_i^2) & \sum x_i \\ \sum x_i & n \end{vmatrix}} \quad , \qquad \text{Eqn. 24}$$

where x is the abscissa value, y is the ordinate value, i refers to a particular value in a total number elements (n). The y-intercept of the same line is determined in a similar manner with

$$b = \frac{\begin{vmatrix} \sum (x_i^2) & \sum (x_i y_i) \\ \sum x_i & \sum y_i \end{vmatrix}}{\begin{vmatrix} \sum (x_i^2) & \sum x_i \\ \sum x_i & n \end{vmatrix}} . \qquad \text{Eqn. 25}$$

As stated above, the only deviations in the fit are found in the ordinate values. The variance in these vertical deviations, s_y^2, can be calculated by

$$s_y^2 = \frac{\sum(d_i^2)}{n-2}, \qquad \text{Eqn. 26}$$

where d represents the vertical deviation of each ordinate value from the best fit straight line. The variance in the vertical deviations can be used to calculate the standard deviation in the slope and y-intercept as calculated by the method of least squares. The standard deviation of the slope, s_m, is equal to

$$s_m = \sqrt{\frac{s_y^2 \cdot n}{\begin{vmatrix} \sum(x_i^2) & \sum x_i \\ \sum x_i & n \end{vmatrix}}}, \qquad \text{Eqn. 27}$$

Similarly, the standard deviation of the y-intercept, s_b, can be found by:

$$s_b = \sqrt{\frac{s_y^2 \cdot \sum(x_i^2)}{\begin{vmatrix} \sum(x_i^2) & \sum x_i \\ \sum x_i & n \end{vmatrix}}}, \qquad \text{Eqn. 28}$$

Linear least squares analyses of the observed rate constant versus ligand concentration yields both the values of association and dissociation rates of the molecular interaction as well as the deviation in their measurement. The uncertainty in the determination of τ from the nonlinear regression algorithm is propagated through the calculation of the on and off rates yielding an equilibrium dissociation constant by the equation $K_D = \frac{k_2}{k_1}$ with its associated error.

5.5 Summary

A description of the interference pattern was given. A closer look at simulations of the light propagation through the BI system revealed the inherent high sensitivity of the instrument is most likely due to the multiple passes light makes through the microfluidic channel. Digital signal processing of the signal was discussed as well as approaches for data analysis. A detailed derivation was given outlining the steps taken to analytical solve for K_D from kinetic measurements using the BI system. While our first attempt at kinetic analysis fails to completely describe higher ordered systems it does offer a functional assessment of the molecular interaction and applicable K_D values. It is worth noting that equation 21 has been used elsewhere in the literature for the determination of binding affinities.[32, 33] Factors affecting the noise of the BI system were also discussed as well as approaches to minimize their presence. An error analysis was presented, indicating the possible limitations noise may place on the overall performance of the instrument.

(1) Bornhop, D. J. *Applied Optics* **1995**, *34*, 3234-3239.

(2) Bornhop, D. J.; Hankins, J. *Analytical Chemistry* **1996**, *68*, 1677-1684.

(3) Kenmore, C. K.; Erskine, S. R.; Bornhop, D. J. *Journal of Chromatography A* **1997**, *762*, 219-225.

(4) Latham, J. C.; Markov, D. A.; Sorensen, H. S.; Bornhop, D. J. *Angewandte Chemie-International Edition* **2006**, *45*, 955-958.

(5) Markov, D. A.; Bornhop, D. J. *Fresenius Journal of Analytical Chemistry* **2001**, *371*, 234-237.

(6) Markov, D. A.; Swinney, K.; Bornhop, D. J. *Journal of the American Chemical Society* **2004**, *126*, 16659-16664.

(7) Markov, D. A.; Dotson, S.; Wood, S.; Bornhop, D. J. *Electrophoresis* **2004**, *25*, 3805-3809.

(8) Sorensen, H. S.; Pranov, H.; Larsen, N. B.; Bornhop, D. J.; Andersen, P. E. *Analytical Chemistry* **2003**, *75*, 1946-1953.

(9) Sorensen, H. S.; Larsen, N. B.; Latham, J. C.; Bornhop, D. J.; Andersen, P. E. *Applied Physics Letters* **2006**, *89*, -.

(10) Swinney, K.; Markov, D.; Hankins, J.; Bornhop, D. J. *Analytica Chimica Acta* **1999**, *400*, 265-280.

(11) Swinney, K. A.; Bornhop, D. J. *Journal of Microcolumn Separations* **1999**, *11*, 596-604.

(12) Swinney, K.; Pennington, J.; Bornhop, D. J. *Microchemical Journal* **1999**, *62*, 154-163.

(13) Swinney, K.; Pennington, J.; Bornhop, D. J. *Analyst* **1999**, *124*, 221-225.

(14) Swinney, K.; Markov, D.; Bornhop, D. J. *Review of Scientific Instruments* **2000**, *71*, 2684-2692.

(15) Swinney, K.; Markov, D.; Bornhop, D. J. *Analytical Chemistry* **2000**, *72*, 2690-2695.

(16) Swinney, K.; Bornhop, D. J. *Applied Spectroscopy* **2000**, *54*, 1485-1489.

(17) Swinney, K.; Bornhop, D. J. *Analyst* **2000**, *125*, 1713-1717.

(18) Swinney, K.; Bornhop, D. J. *Electrophoresis* **2000**, *21*, 1239-1250.

(19) Swinney, K.; Bornhop, D. J. *Electrophoresis* **2001**, *22*, 2032-2036.

(20) Swinney, K.; Nodorft, J.; Bornhop, D. J. *Analyst* **2001**, *126*, 673-675.

(21) Swinney, K.; Nodorft, J.; Bornhop, D. J. *Applied Spectroscopy* **2002**, *56*, 134-138.

(22) Tarigan, H. J.; Neill, P.; Kenmore, C. K.; Bornhop, D. J. *Analytical Chemistry* **1996**, *68*, 1762-1770.

(23) Wang, Z. L.; Swinney, K.; Bornhop, D. J. *Electrophoresis* **2003**, *24*, 865-873.

(24) Markov, D.; Begari, D.; Bornhop, D. J. *Analytical Chemistry* **2002**, *74*, 5438-5441.

(25) Motulsky, H.; Christopoulos, A. *Fitting Models to Biological Data Using Linear and Nonlinear Regression*; Oxford Univeristy Press: New York, 2004.

(26) Swillens, S. *Molecular Pharmacology* **1995**, *47*, 1197-1203.

(27) Wang, Z. X.; Jiang, R. F. *Febs Letters* **1996**, *392*, 245-249.

(28) Kreyszig, E. *Advanced Engineering Mathematics*, 7th ed.; John Wiley & Sons, Inc.: Hoboken, 1992.

(29) de Paula, J. a. A., P. *Physical Chemistry*, 7th ed.; W. H. Freeman, 2001.

(30) Skoog, D.; Holler, F.; Nieman, T. *Principles of Instrumental Analysis*, 5th ed.; Harcourt Brace and Company: Orlando, 1998.

(31) Harris, D. *Quantitative Chemical Analysis*, 5th ed.; W.H. Freeman and Company: New York, 1999.

(32) Sapsford, K. E.; Liron, Z.; Shubin, Y. S.; Ligler, F. S. *Analytical Chemistry* **2001**, *73*, 5518-5524.

(33) Lahiri, J.; Isaacs, L.; Tien, J.; Whitesides, G. M. *Analytical Chemistry* **1999**, *71*, 777-790.

CHAPTER VI

APPLICATIONS

BI can be used to monitor label-free molecular interactions in very small volumes by either a bulk or surface sensing mode.[1-4] In the surface sensing mode, molecules of interest are immobilized onto the functionalized surface of a microfluidic channel. The immobilized molecule can then be interrogated by passing solutions through the channel. Any interactions can be monitored by BI in real-time or as an end point analysis. However, studying molecular interactions where one of the participants is immobilized to the substrate can be problematic for multiple reasons. Not only can the surface chemistry employed by tedious and time consuming, but the chemistry can also exhibit reduced surface activity over time. Even more troublesome, is the affect surface immobilization has on the molecular interaction itself with reports showing equilibrium constants can be off by as much as a factor of 6 and kinetic parameters can be altered by a factor of 30 when compared to solution phase interactions.[5]

The ability to perform pure liquid–phase molecular binding analyses in a μ-TAS format would eliminate many of the problems that arise from immobilization chemistries, while allowing the study of samples in ultra-small volumes. BI offers this capability and has been previously used in such a manner for the free solution analysis of enzyme kinetics in capillaries. However, as mentioned previously (*see 4.1.4*), the implementation of plastics to nanotech devices has yielded capillary investigations near obsolete.

Here we look at the use of BI for surface sensing studies as a potential competitor to SPR. Solution phase molecular interactions are also performed in a microchip format. These investigations are compared to published literature values and at times cross-validated with alternative techniques to examine the accuracy and versatility of the BI sensing technique.

6.1 Surface Bound Experiments

6.1.1 *Immobilization Chemistry*

For the first time, a simple photoactivatable surface chemistry[6, 7] was shown to allow the immobilization of target molecules in a microchip facilitating label-free, reversible molecular interaction assays via biotin/avidin linkage. A carbene-generating form of photobiotin consisting of a biotin moiety, spacer arm, and photoactivatable group was used to functionalize microchannels molded in PDMS (*see Section 3.1 for microchip fabrication*). A 0.5 mg/mL solution of this carbene-generating photobiotin was made in a solvent system containing water, Tween-20, and acetone in a 49.98 : 0.02 : 50 ratio (v : v). A small volume (ca. 5 – 7 µL) of the photobiotin solution was introduced into the PDMS channels and allowed to dry. Irradiation of the photobiotin molecule caused photolysis of the diazarine group producing an electronically excited n-p* state. Formation of an excited state di-radical was followed by internal conversion and production of a carbene. The highly reactive carbene was then inserted into the oxidized substrate. As a result, a homogeneous layer of biotin molecules was strongly bound to the channel surface. A solution of ExtrAvidin (0.5 mg/mL) was injected into the same channels and allowed to incubate for 30 minutes. ExtrAvidin recognizes the imidazoline ring that is cis fused to a tetrahydrothiophene ring and binds to biotin with high affinity (K_a = 2.5 × 10^{11} M^{-1}).[8] The resulting biotin/avidin complex formed is very stable to changes in temperature, pH, and denaturing agents, unlike the lysine/glutaraldehyde/streptavidin/ethanolamine sandwich

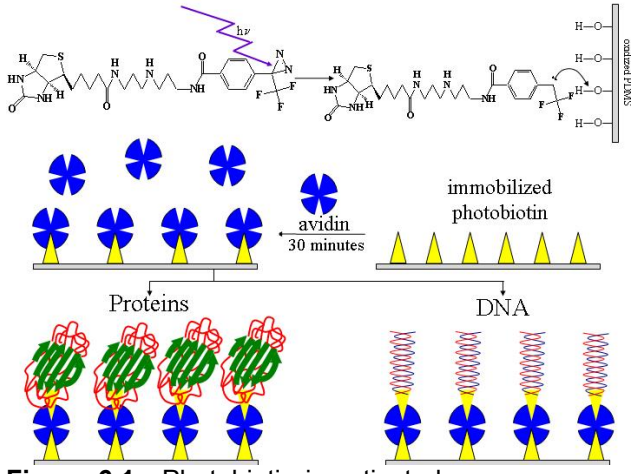

Figure 6.1. Photobiotin is activated upon exposure to UV light promoting insertion into the oxidized PDMS substrate. Avidin binds strongly to the immobilized layer of biotin. The tetrameric nature of avidin signifies that it can simultaneously bind the surface bound biotin as well as any biotinylated target molecule that passes through the channel.

described in our earlier binding experiments.[2] Fluorescent images (not shown) of FITC-labeled avidin were used to confirm that the surface chemistry used for immobilization was successful. Thus, any biotinylated target of interest could henceforth be immobilized onto the PDMS-molded channel surface. And while this method proved to be widely effective in functionalizing PDMS surfaces, the technique could also be employed on glass, fused silica, silicon, acrylic and various polymers. This simplified and direct immobilization strategy resulted in the production of a cost-effective, disposable microchip applicable to the study of multiple molecular interactions. This photobiotin approach further improved not only our earlier binding studies but those commonly used for surface activation interaction assays.[9, 10]

6.1.2 *Experimental Setup*

In order to evaluate the new immobilization chemistry, two reversible binding pairs were studied: protein A (P_A) to the immunoglobulin IgG and the hybridization of complementary 30mer DNA strands. Both sets of interaction assays were performed using a traditional BI experimental setup (Figure 6.2). In short, a focusing lens (Oz Optics, Ontario, Canada) with a 283 mm working distance was fiber optically coupled to a 5mW, 632.8 nm HeNe laser (Melles Griot, Carlsbad, CA). The output beam was directed onto a microchip molded in PDMS using a highly reflective (> 99%) aluminum mirror. The mirror above the PDMS chip was positioned so that the incident beam was directed onto the flow channel orthogonal to fluid flow. The angle of the mirror and the correct working distance ensure parallel rays impinge the channel. The proper working distance was measured both physically and by adjusting the reflected laser spot size in the far field. When properly aligned, the spot size of the laser beam at the channel was calculated to have a diameter of 100 μm. The PDMS microchip was securely

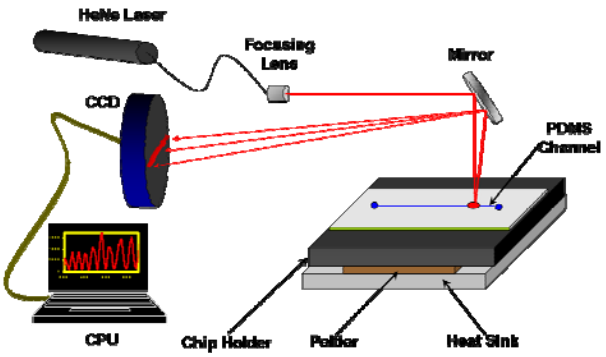

Figure 6.2. Experimental setup for BI molecular interaction assays (*not drawn to scale*).

mounted on top of an aluminum block. A Melcor temperature controller (Trenton, NJ) was used to closely regulate the temperature of the system through a Peltier thermoelectric cooler attached to the mounting block. The microchip assembly was connected to two translation stages which allow movement of the chip in both x and y directions. A portion of the high resolution backscattered interference pattern produced upon the interaction of light with the microchip was directed by the same mirror onto a GARRY 3000 CCD array (Ames Photonics, Hurst, Texas) functioning as a position sensing transducer (*see Section 5.2*). The CCD array contains 3000 pixels with each pixel 7 μm wide, 200 μm tall, and having 7 μm center-to-center spacing. The array has a total length of 21 mm and has a pseudo-Gaussian spectral response from 350 – 1100 nm with its quantum efficiency centered near 500 nm.

The laser and temperature controller were powered on and allowed to equilibrate over a one hour period prior to starting any experiments. The centroid of the backscattered interference pattern was located just above the focusing lens insuring that the alignment of the system was along a central plane. The CCD array was positioned near direct backscatter in order to capture what was simulated to be the most spatially sensitive section of the interference pattern. Typically, the edge of the CCD array was positioned to capture the 5^{th} or 6^{th} constructive interference fringe from the centroid and outward. Although the modeled fringes nearest direct backscatter produced larger spatial shifts with changes to the optical pathlength with respect to fringes farther out, a balance between sensitivity and the working conditions of the system must be met when aligning the CCD near the centroid. Light intensity near direct backscatter is extremely high and must be attenuated so as to not saturate the detector. However, in doing so, the only fringe that remains detectable in the current setup is the centroid, negating the need and advantages of the large area CCD array and FFT algorithm. Also, the interference fringes near direct backscatter are less sinusoidal and resemble more of a damped oscillator or Bessel function degrading the FFT output and making the determination of a dominant spatial frequency troublesome. Furthermore, the frequencies that are easily quantified in the magnitude spectrum of the FFT at positions very close to the centroid are often times masked by DC noise.

6.1.3 *Protein A and IgG*

The Protein A•IgG molecular interaction was the first chosen in testing the new biotin/avidin surface chemistry for a direct comparison to our previously published results.[2] Discussed in detail later (*Section 6.2.1*), P_A contains four high affinity (K_a = 2×10^8 - 4.54×10^8 M^{-1})[11, 12] binding sites capable of interacting with the F_c region from IgG of several species, including human and rabbit. A biotinlyated form of P_A was immobilized onto the walls of a microfluidic channel molded in PDMS using the surface chemistry described in *Section 6.1.1*. Unreacted P_A was washed out of the channel with a solution of phosphate buffered saline (PBS) containing a small percentage (< 5%) of Tween-20. After unreacted P_A had been removed, the interference pattern was recorded with buffer solution present in the microchannel as described in *Section 5.2*. This measurement corresponds to the red and white plaid monoliths in Figure 6.3. Upon removal of the buffer from the PDMS channel, a 0.5 mg/mL solution (PBS @ pH = 7.2) of the F_c fragment from human IgG was introduced into the microchannel and allowed to interact with P_A for ~5 min. The channel was then rinsed with PBS/Tween-20 to remove any unbound IgG and left in buffer. Again the interference pattern was recorded corresponding to the solid red bars in Figure 6.3. Bound IgG was removed from immobilized P_A using an acetic acid wash. This reversible binding assay was repeated 5 times with all results reported in Figure 6.3. As seen from the small error bars in the plot, the molecular interactions were monitored with excellent S/N (s_{pooled} = 0.0017). Quantification of the interaction was taken as the difference in the magnitude of the two signals. The average signal change for binding taken across all five runs was 0.196 radians (± 0.021). The non-complementary fragment of IgG, F_{ab}, served as the control. When allowed to interact with P_A under the same conditions, the F_{ab} fragment presented no discernable signal (change in

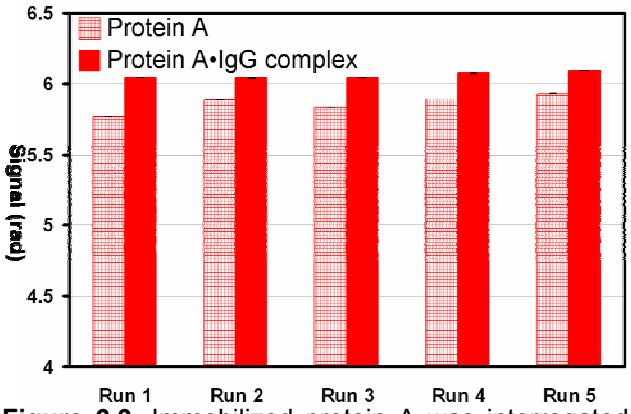

Figure 6.3. Immobilized protein A was interrogated five times with a 0.5 mg/mL solution of IgG.

RI/phase) above that of the noise level. Assuming that the complete reaction between the binding pair took place and based on the target surface coverage, the 3σ detection limit for the P_A•IgG interaction was 4×10^{-17} moles or 40 attomoles in a 500 pL probe volume. These results represent a two orders of magnitude increase in sensitivity when compared to the same P_A/IgG experiments performed previously.[2, 13]

6.1.4 *DNA Hybridization*

The use of microfluidic chips to perform nucleic acid analyses has allowed the detection and discrimination of multiple DNA sequences[14, 15] and can eventually facilitate high throughput screening techniques[16]. As further demonstration of the utility of BI, a label-free reversible DNA assay was performed. Immobilization of a biotinylated 30mer of mActin (5′-ACTCATCGTACTCCTGCTTGCTGATCCACA-3′, MW = 9622.5, and T_M = 68.7°C) onto the surface of PDMS channels was possible with the biotin/avidin surface chemistry as described above. Non-labeled, complementary DNA strands were successively hybridized to the immobilized mActin 30mer and then removed by a NaOH wash. Binding events of complementary DNA followed an exponential growth for BI over concentrations ranging from 5 nM to roughly 500 mM with excellent convergence as R^2 = 0.988 (Figure 6.4). A 5 μM concentration of nonsense strand, according to the Watson-Crick model, served as the control and showed no appreciable signal. Assuming hybridization went to completion and

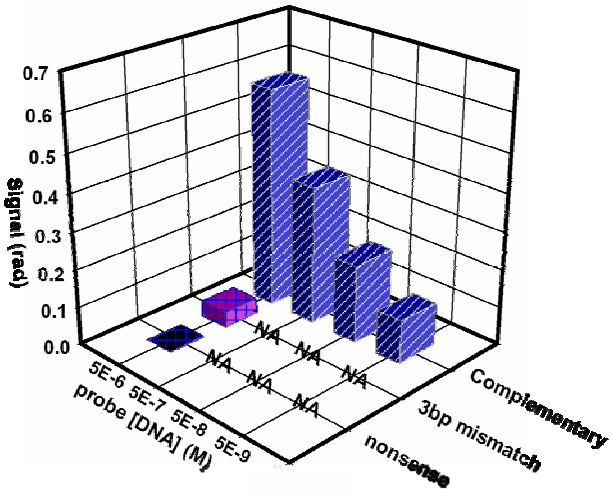

Figure 6.4. Shown is the binding affinity of a complementary DNA strand to an immobilized target over multiple complementary strand. The complementary strand is also compared to a 3bp mismatch and control strands at high concentration. All probe strands were allowed 20 minutes for hybridization.

100% channel surface coverage was attained, at 3σ, 36 attomoles of DNA were quantifiable in a 500 pL detection volume.

Ultimately it would be desirable to screen arrays of interactions with molecules having conserved sequences varied by single point mutations or with slight variations due to mutagenesis. In order to avoid perturbations and reduce costs, screening large arrays of molecules would be better served by determinations made in a label-free format (i.e. *sans* fluorophore or radioligand). A step toward this goal was accomplished here using BI by discrimination of a slight sequence variation in DNA hybridization. An oligomer consisting of a 3 base pair (3bp) mismatch at positions 5, 15, and 25 from that of the complementary mActin strand was used as an initial test of specificity. The experiment consisted of immobilizing the mActin 30mer as noted above, followed by a repetitive hybridization test with a 5 μM solution of the 3bp mismatch strand. Three trials of these experiments produced an average signal corresponding to >140% of that for the nonsense strand and ca. 7% of the complementary strand as seen in Figure 6.4.

6.2 Solution Phase Interactions - *Proof of Concept*

6.2.1 *Background*

In order to first characterize the capability of BI to monitor solution phase molecular interactions a test case was chosen. Due to its previous use (*Section 6.1.3*) and well described properties, the P_A•IgG system was again studied here. P_A•IgG provided a model system to evaluate the analytical performance of BI in determining binding data for free solution assays and serve as a standard by which measurements could be compared.

As stated above (*Section 6.1.3*), P_A binds the F_c region of IgG from several species, including human and rabbit with high affinity.[11, 12] IgG is a member of the diverse family of immunoglobulins (or antibodies) that define humoral immunity. Immunoglobulins are glycoproteins produced by *B* cells and are effective against extracellular phases of viral infection and bacterial infections.[17] All immunoglobulins consist of four subunits: two identical light chains

(~23 kD) and two identical heavy chains (53 – 75 kDa). These four chains form a quaternary structure consisting of a symmetric dimer in the shape of a Y (Figure 6.5). Response of the humoral immune system is initiated with the recognition of foreign macromolecules called antigens by membrane bound immunoglobulins on *B* cells, often termed *B* cell receptors or BCR. Two antigen binding sites are located in the F_{AB} fragment of an antibody. These regions of the immunoglobulin are specific to a particular epitope. An epitope is a short peptide sequence on the surface of the antigen. Once a BCR recognizes the epitope and binds the antigen, the *B* cell engulfs the complex and partially digests the antigen.[18, 19] Digested fragments on the *B* cell surface are recognized by *T* cells.[20, 21] The *T* cells consequently release interleukins promoting proliferation and differentiation of *B* cells.[13] The new *B* cells are primarily plasma cells which secrete large amounts of antigen specific antibodies that bring about cell death.[22] Protein A however disrupts the humoral immune destruction of antigens. Present on the cell wall of the bacteria *Staphylococcus aureus*, P_A binds the F_C region of immunoglobulins rather than the antigen binding domains in the F_{AB} fragments. Phagocytosis of the bacteria is reduced by this altered binding approach and is the principal factor for the virulence of *Staphylococcus aureus*.

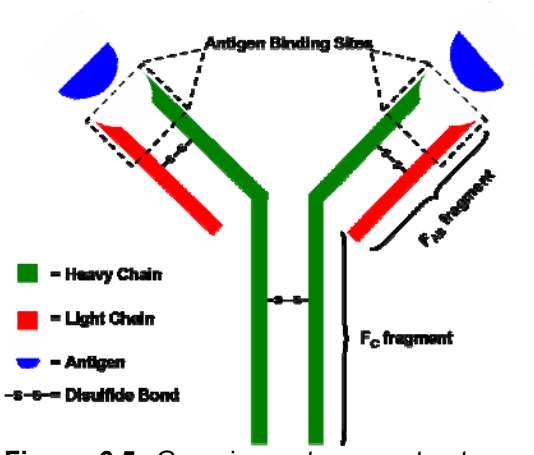

Figure 6.5. Generic quaternary structure of the symmetric dimer formed by immunoglobulins.

6.2.2 *Experimental*

Solution phase BI interrogations of P_A and IgG interaction assays were performed using a similar experimental setup to that of surface sensing mode (Figure 6.6A). The only difference between the two setups is the type of microfluidic chip used. In the surface sensing mode, straight channels molded in PDMS were used as there was no need for active mixing. However, as discussed in detail previously (*Section 4.3*), reactants in solution phase BI experiments must

be mixed in the channel prior to detection of any molecular interaction. A serpentine mixer with additional hydrodynamic focusing (Figure 6.6B) was employed for the P_A•IgG binding experiments as well as all free solution molecular interactions presented in this chapter. A fabricated microchip used in some solution phase experiments is displayed in Figure 6.6C with a United States quarter to offer some perspective on the size of a functioning chip.

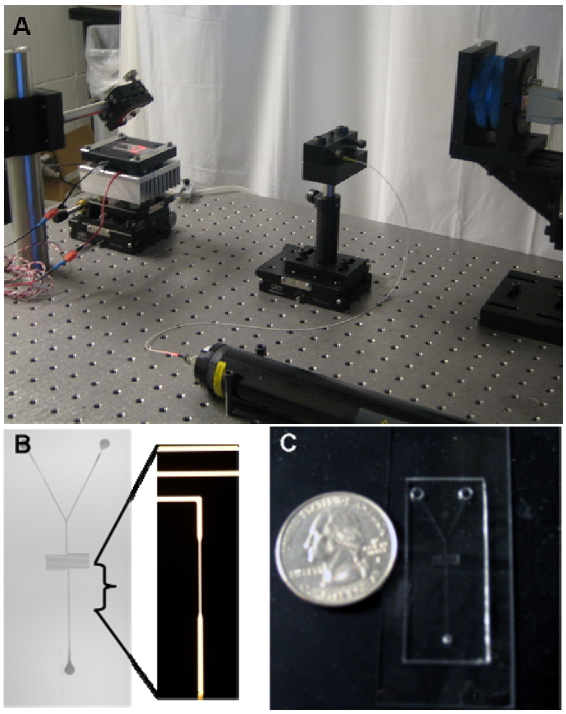

Figure 6.6. Digital picture of the BI experimental setup (A), microscopic image of the photolithographic mask containing the mixer design used (B), and a digital image of a microreactor chip molded in PDMS (C).

All solutions of P_A and IgG were buffered at a pH = 7.2 with 0.15M $Na_2H_2PO_4$, 0.1M KCl, 0.1mM EGTA, and 0.1% sodium azide. The pH of each solution was adjusted by the addition of small amounts 5N NaOH or 5N HCl and monitored by a standard pH electrode. The concentration of P_A was held constant throughout the experiment at 2.5 nM. A range of concentrations for the F_C fragment of IgG (10, 15, 20, 30, and 40 nM) were sequentially mixed with P_A on-chip. Each solution phase molecular interaction was monitored in real-time (ca. 100 Hz) over a span of ~60 seconds. The array of binding signals detected by BI is presented in Figure 6.7. As can also be seen from Figure 6.7, a control run was performed whereby Protein A was mixed with the F_{AB} fragment of IgG. In order to indicate a worse case scenario of potential non-specific binding and mixing artifacts, the concentration of the F_{AB} was kept at the highest quantity used during the P_A•IgG experiments. The F_{AB} control produced < 1.6% of the observed signal at equivalent F_C concentrations. The absolute signal of the control was found to be 0.026 radians (± 0.0032). As the magnitude of the non-binding interaction remains constant across various concentrations of

the F_{AB} fragment, this measurement is seen as more a mixing artifact rather than non-specific binding which is generally reported to increase with added concentrations of ligand.

6.2.3 *Analysis and Results*

Kinetic and steady-state analyses were performed as outlined in *Section 5.3*. Briefly, nonlinear least squares regression was used to fit the kinetic traces in Figure 6.7 to a single exponential: $y = a(1-e^{-\tau x})$. Iterative optimization procedures were used to compute the parameters a and τ for each molecular interaction curve of P_A with the various concentrations of IgG. A linear relationship between the observed rate of interaction ($k_{obs} \equiv \tau$) and the concentration of the F_C fragment was observed with the linearity reported in Figure 6.8A. The coefficient of determination, R^2, was calculated to be 0.987 indicating very little variation between the data points and the best fit line determined by linear least squares. As described in *Section 5.3*, the slope and y-intercept of the best fit line in Figure 6.8A correspond to the on and off rates of the molecular interaction respectively. Therefore determination of the slope and intercept (as well as their respective errors) using the method of least squares (*see Section 5.4*) enable the determination of K_D from the kinetic traces of P_A-IgG by the aforementioned equation, $K_D = \frac{k_2}{k_1}$. The equilibrium dissociation constant as calculated in this manner from BI measurements was 7.91 nM (±1.21) with the uncertainty in the K_D value determined by the error of the slope and y-intercept. The K_D determination obtained by BI is highly accurate, falling well within the range of earlier published results.[11, 12] Upon closer examination of the kinetic data, the on rate for the molecular interaction of protein A and the F_C fragment of IgG was calculated to be 2×10^7 $M^{-1}s^{-1}$ while the off rate was measured to be 0.02 s^{-}

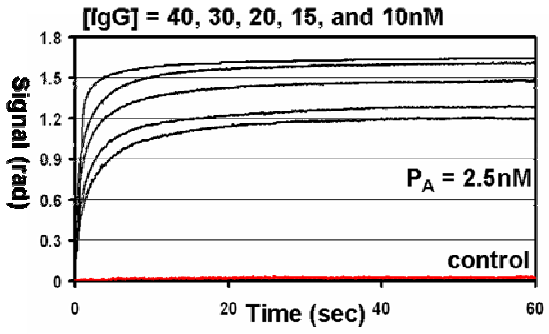

Figure 6.7. Real-time kinetics of P_A interacting with different concentrations of the F_C fragment of IgG (black traces) and a control (red trace) consisting of the F_{AB} fragment of IgG.

[1]. The rates of the P_A•IgG system as determined by an acoustic waveguide sensor were markedly different from those determined by BI. Saha, *et.al*[11] measured the on and off rates as 8.02×10^3 $M^{-1}s^{-1}$ and 2.77×10^{-4} s^{-1} respectively for the interaction of IgG with protein A. However, in their experiments, Saha, et.al relied on simple protein adsorption to a gold coated surface for immobilization of protein A onto a microchip format. Protein adsorption onto a surface is a fairly unreliable and heterogeneous method for surface functionalization unlikely to withstand the rigors involved with multiple interrogations by IgG at high flow rates. On rates for molecular association are often diminished by diffusion to the protein coated surfaces and steric hindrance. Conversely, off rates tend to be enhanced in surface bound studies by increased flow rates, reduced activity of the immobilized protein and again steric hindrance. Mass transfer effects are also problematic in molecular interactions at surfaces with the size of the probe molecule, the flow rate, and the characteristic distance traversed all adding dimensionalities of possible error and further explaining the difference in the two methods observed kinetic parametes.

A steady-state analysis was used to further corroborate our kinetically derived description of the P_A•IgG system. As described in *Section 5.3*, the end point values, a, determined by nonlinear regression exhibit a hyperbolic relationship as a function of the concentration of IgG.

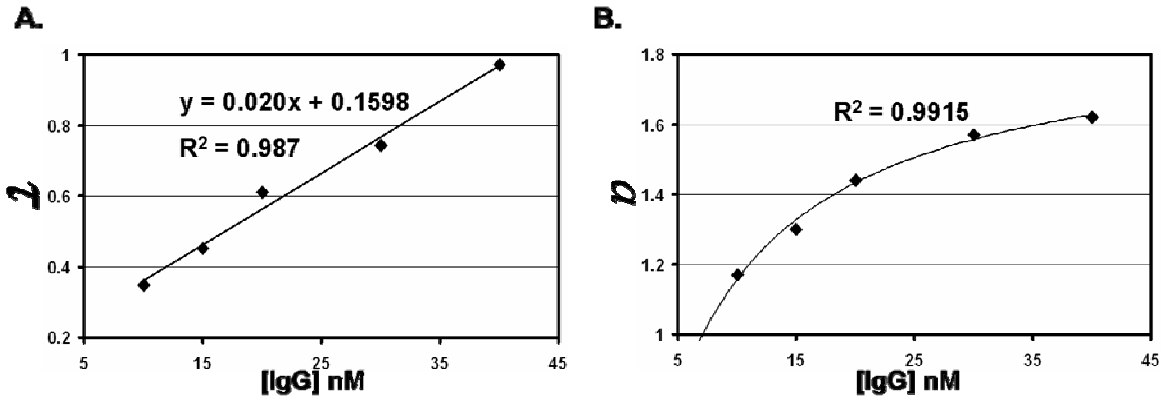

Figure 6.8. Kinetic analysis (**A**) of the P_A•IgG interaction yields a linear relationship for the observed rate of reaction over the concentration range of IgG studied. An end point analysis (**B**) of the signal determined at steady-state conditions was analyzed using nonlinear regression techniques built-in to Prism® fitting software. Both analysis techniques of BI data produce K_D values very similar to each other and well within accepted literature values.

Fitting this relationship to the saturation binding equation (Chapter V, Equation 1) based on the law of mass action allows a second determination of the equilibrium dissociation constant. The biostatistical software package Prism® (Graphpad, San Diego, CA) was employed to fit the end point data and compute K_D. The standard steady-state parametric fitting routine found in Prism yielded a K_D value of 6.27 nM (±0.47). Not only does this thermodynamic evaluation provide accurate results in comparison to accepted published values for the equilibrium dissociation constant of the P_A•IgG system, but it also demonstrates excellent precision with the kinetically derived parameter.

6.3 Calmodulin Studies

6.3.1 Background

The initial solution phase interactions of Protein A and IgG helped to validate the BI technique was capable of monitoring label-free molecular interactions without the need for tedious immobilization chemistries. Furthermore, kinetic and thermodynamic data could be readily obtained from BI measurements and were found to correlate well to previously published results. Upon completion of these preliminary investigations a broader and more diverse group of interactions were chosen to explore the dynamic range of the BI instrument for free solution assays. Molecular interactions of calmodulin, a calcium binding protein heavily involved in cellular processes, were performed with four various ligands: a small ion (Ca^{2+}), a small molecule inhibitor (trifluoperazine dihydrochloride), a peptide from the sequence of skeletal muscle myosin light chain kinase (sk-MLCK), and a protein phosphotase (Calcineurin). These four ligands range from 40.04 Da to roughly 77.8 kDa in molecular weight and differentially bind Calmodulin with affinities from $10^5 – 10^9$ (M^{-1}).

Calmodulin (CaM) is a highly conserved, low molecular weight protein (16.7 kDa) essential to the regulation of calcium in eukaryotic cells.[23] CaM is an EF-hand protein, whereby two α-helices connected by a loop form a ‘hand’ that binds calcium.[23, 24] CaM contains four such hands each containing 12 amino acid residues that serve as the active site for calcium binding.[23]

Two of the four binding loops are located in the N-terminal of calmodulin and are denoted as loops I and II while the remaining two binding domains are found in the C-terminus (loops III and IV) as seen in Figure 6.10. Calcium ions are thought to bind sequentially to the C and N terminal domains yet cooperatively intra-terminally.[25-27] In fact loops III and IV bind calcium with 6 – 10 times higher affinity than the binding domains of the N-terminus.[27, 28] Calcium is a key component in cell signaling pathways and can readily cross the plasma membrane through ion channels. Calcium is known to either initiate or have a primary function in cascading cellular events that involve: glycogen and lipid degradation, muscle contraction, cell division, apoptosis, and the release of chemical transmitters.[23] Calmodulin serves to buffer and transport calcium thereby helping to regulate these processes.

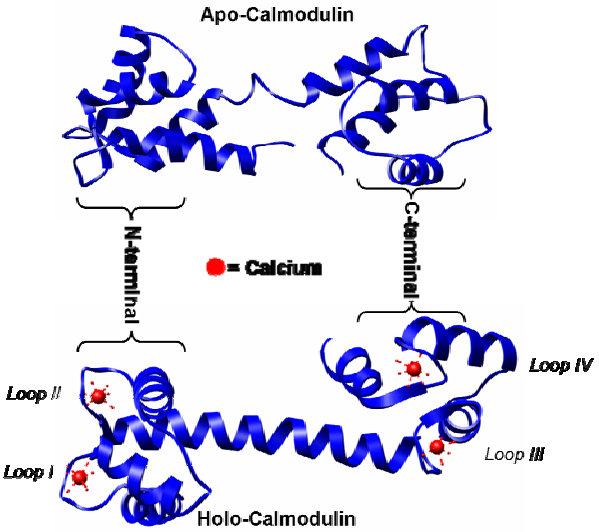

Figure 6.9. Structural comparison of the apo- and holo-states of calmodulin. The four calcium (red dots) binding loops are indicated. Apo-calmodulin (pdb = 1CFD) and holo-calmodulin (pdb = 1CLL) were taken from the Protein Data Bank and displayed using the freeware Chimera.

Apo-calmodulin (no bound calcium) undergoes a large conformational change after binding calcium thereby inducing latent activity and drastically altering the protein structure (see Figure 6.9). The two antiparallel α-helices in each EF-hand motif become perpendicular in the holo-calmodulin (bound calcium) state.[29, 30] This α-helical rearrangement tightens the binding loops making them less solvent accessible.[31] The α-helical content of holo-calmodulin increases by as much as 10% when compared to the apo-state.[23] The N to C terminal linker becomes more flexible in the holo-state with higher exposure of hydrophobic surfaces dramatically increasing calmodulin binding to target molecules. In fact, holo-calmodulin can bind and regulate over 25 different molecules involved in a plethora of cellular functions.[32, 33]

Trifluoperazine is a member of the phenothiazine antipsychotic drug group. Trifluoperazine alters cell signaling in the brain by two independent pathways. The molecule is an antagonist for the D2-like family of dopamine receptors. Dopamine receptors (i.e. G-protein-linked receptors) are found in all eukaryotes and mediate a diverse array of signaling molecules including hormones, neurotransmitters, etc. D2-like activation increases phosphodiesterase activity. Phosphodiesterases inactivate cAMP (3'-5'-cyclic adenosine monophophate) by hydrolysis to AMP, producing an inhibitory effect in neurons. Therefore antagonism of the dopamine receptor by trifluoperazine negates phosphodiesterase activity and its inhibition of neurotransmitter signaling. In a secondary pathway, trifluoperazine can inhibit calmodulin stimulation of 3'-5'-cyclic nucleotide phosphodiesterase which again inactivates cAMP. Trifluoperazine is thought to hinder calmodulin regulated phosphodiesterase activity by binding a hydrophobic pocket in the C-terminal domain of the calcium activated form of calmoldulin making contact at 13 residues.[34, 35] Holo-calmodulin compacts upon binding trifluoperazine, collapsing about the N to C terminal linker (Figures 6.10 and 6.11). A trifluoperazine derivative, trifluoperazine dihydrochloride (TFP), was studied in our holo-CaM binding interactions.

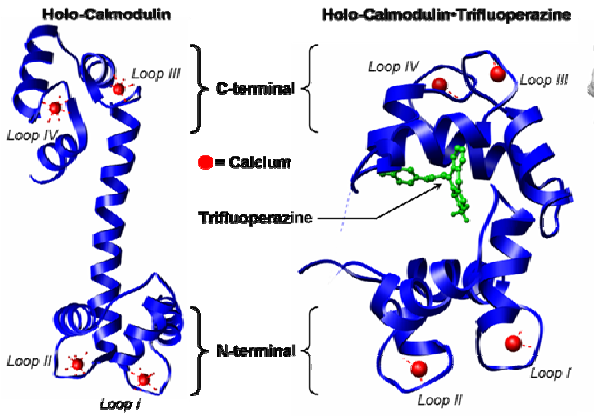

Figure 6.10. Ribbon structure of holo-calmodulin observed after binding to trifluoperazine. Holo-calmodulin (pdb = 1CLL) and the trifluoperazine bound species (pdb = 1CTR) were taken from the Protein Data Bank and displayed using the freeware Chimera.

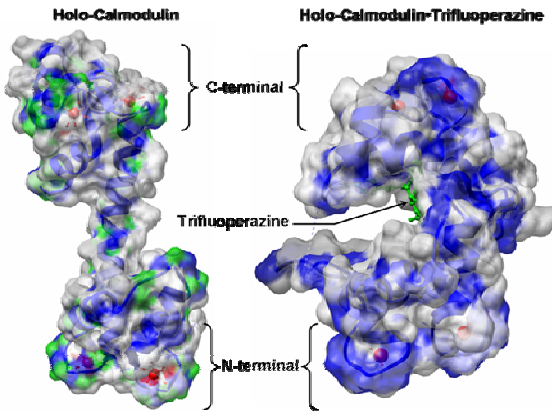

Figure 6.11. A surface structural comparison of holo-calmodulin to trifluoperazine bound holo-calmodulin better demonstrates the compaction seen upon ligand binding.

As mentioned previously, calcium can either initiate or have a primary function in cascading cellular events. Many of the indirect effects of calcium are mediated by the phosphorylation of proteins. Multiple phosphorylation pathways are catalyzed by a family of protein kinases dependent upon the holo-calmodulin complex. Termed CaM-kinases, these enzymes phosphorylate serines and threonines on proteins. The first CaM-kinase to be discovered was myosin light chain kinase (MLCK), an important component in muscle contraction. An influx of calcium into the smooth muscle will bind calmodulin and activate myosin light chain kinase. MLCK phosphorylates the myosin light chain which can then bind actin producing muscle contraction via a molecular motor.

Lastly, the serine-threonine protein phosphotase, calcineurin was employed as a high molecular weight ligand for our calmodulin studies. Calcineurin is the major Calmodulin binding protein in the brain.[36] Regardless of its source, calcineurin is present as a heterodimer. The catalytic subunit, calcineurin A, is a 58 – 64 kDa protein containing a calmodulin binding site, a secondary subunit binding site, as well as an autoinhibitory domain in the C-terminus.[37] The second subunit, calcineurin B, is a 19kDa protein. It consists of a dumbbell structure similar to that of calmodulin and was initially classified as an 'EF-hand' calcium binding protein.[38] Calcineurin B has two lobes connected by a flexible helical linker with two calcium binding loops present in each lobe.[39] One loop binds calcium at a slightly higher affinity ($K_D < 10^{-7}$ M) than the remaining three loops ($K_D \sim \mu M$).[40] Calcineurin preferentially dephosphorlyates proteins such as: neurogranin, neuromodulin, MAP-2, and tau protein.[41] Calcineurin is also involved in the auto immune response. Detection of antigens in the body increases the intracellular concentration of calcium activating calcineurin. Calcineurin induces transcription of IL-2 which in-turn stimulates T cell response.[42, 43] Furthermore, as noted above, calcineurin A, contains a calmodulin binding site. Calcineurin inhibits the calmodulin regulated activation of 3'-5'-cyclic nucleotide phosphodiesterase by binding Calmodulin with high affinity, rendering the multifunctional protein unavailable to further processes.

6.3.2 Experimental

Investigations of apo-calmodulin (Sigma, St. Louis, MO) binding calcium were conducted in a non-calcium containing buffer. An apo-calmodulin solution was prepared in a 0.1 M HEPES, 0.1 M KCl, and 0.1 mM EGTA buffer at a final concentration of 5 μM. A series of six calcium containing solutions were prepared in the same buffer system having final Ca^{2+} concentrations of: 12.5, 25, 37.5, 50, 75, and 100 μM. Each solution was buffered at a pH = 7.5 as measured by a standard pH electrode with minor adjustments made as needed by the addition of small amounts of 5 N NaOH or 5 N HCl.

Molecular interactions of holo-calmodulin with trifluoperazine dihydrochloride (TFP), the small peptide sequence from the calmodulin binding domain of smooth muscle myosin light chain kinase (hence forth called sm-MLCK), and calcineurin were performed in a calcium containing buffer system to ensure calmodulin was in its conformationally active state. Holo-calmodulin solutions were prepared in 0.1 M HEPES, 0.1 M KCl, and 0.2 mM $CaCl_2$ at final concentrations of 2 μM, 5 nM, and 10 nM for TFP, sm-MLCK, and calcineurin interactions respectively. Solutions of trifluoperazine dihydrochloride were varied in concentrations using the same calcium containing buffer at 5, 7.5, 10, 15, 20, and 25 μM. The MLCK peptide was aliquoted into concentrations of 5, 10, 20, 30, 40, and 50 nM with the aforementioned calcium containing buffer. Calcineurin was solubilized by the calcium buffer as well and diluted into aliquots of 10, 20, 40, 60, 80, and 100 nM. Each of these solutions was buffered at a pH = 7.5 with their measurements and any adjustments made in the same manner as noted above.

All solutions were filtered and degassed prior to binding experiments. Solutions were kept on ice during the experiment and briefly allowed to warm to room temperature prior to their introduction into the microchannel. The experimental setup used in all BI investigations of calmodulin interactions was the same as defined in *Section 6.1.2*. The mixing chip design used was a hybrid serpentine-hydrodynamic focusing mixer as described in *Section 4.3* and displayed in *Section 6.1.2*. All experiments were conducted at 25°C and held stable by a MELCOR temperature controller coupled to a Peltier device. Approximately 4 μL of each reactant was used

in obtaining each association curve. Binding experiments were monitored in real-time at frequencies ca. 50-100 Hz and in detection volumes on the order of picoliters.

6.3.3 Results and Analysis

The raw data (black traces) as detected by BI for all molecular interactions of calmodulin are shown in Figure 6.12. The interaction of apo-calmodulin with calcium is shown in the graph at the upper left hand corner. As expected, the highest concentration of calcium, 100 μM, produced the greatest observable signal among all the calcium concentrations with each successive reduction in calcium concentration yielding a diminished signal. The higher concentrations of calcium were also observed to reach equilibrium faster, a trend predicted by the law of mass action. A 5 μM solution of calmodulin mixed with a 100 μM solution of calcium in the presence of

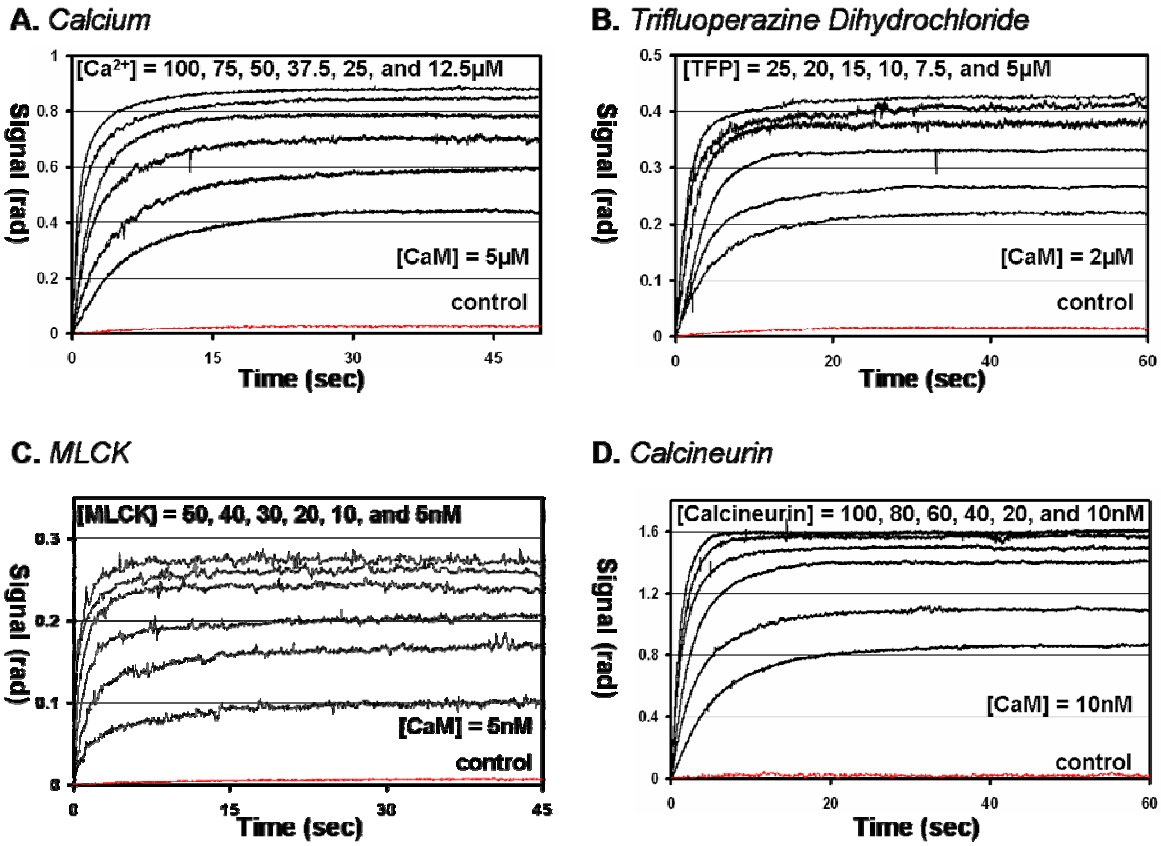

Figure 6.12. Kinetic traces (black) of the association of calmodulin with a small ion (A), a small molecule inhibitor (B), a small peptide (C), and a large protein (D) as detected in real-time by BI. Control experiments (red traces) produced no appreciable signal.

excess EGTA (a calcium chelater) served as the control. The control showed < 3% of the signal observed in the absence of the Ca^{2+} chelating agent EGTA at the same concentrations of CaM and Ca^{2+}. The molecular interaction of holo-Calmodulin with the small molecule inhibitor, short peptide sequence, and the high molecular weight protein all exhibited similar qualitative trends. The highest concentration of {*ligand*} (shorthand for any of the holo-CaM binding partners) produced the largest signal observed by BI with respect to each subset of interactions. Lower concentrations took more time to reach steady state conditions. Controls for the holo-calmodulin interactions consisted of the fixed concentration of calmodulin used in each respective assay mixed with the highest concentration of ligand used in said assay with both constituents in the absence of calcium. Since no calcium was present, calmodulin should be present in its inactive, apo-state where the N to C terminal linker is less accessible and no hydrophobic areas are

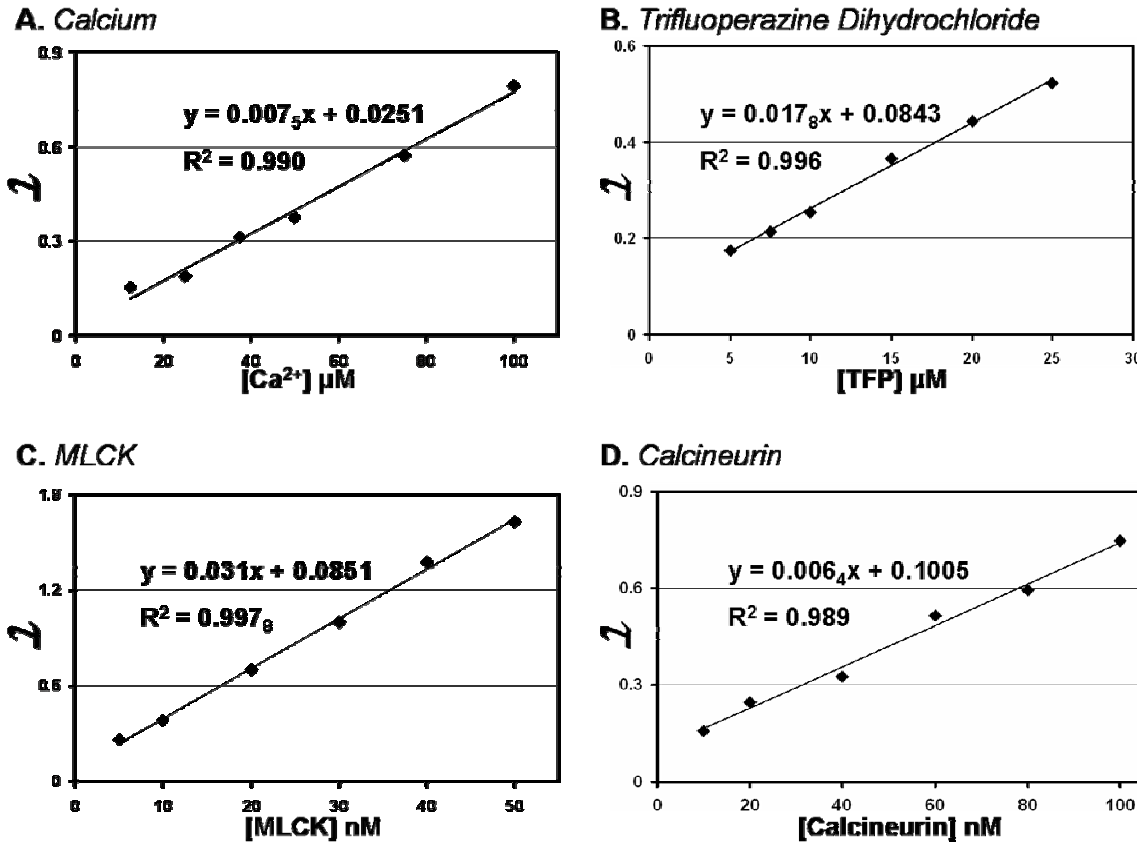

Figure 6.13. The observed rates calculated by nonlinear regression of the association curves of calmodulin interacting with calcium (A), trifluoperazine dihydrochloride (B), MLCK (C), and calcineurin (D) plotted as a function of ligand concentration.

available for ligand binding. BI measured changes in phase for the controls of TFP, MLCK, and calcineurin were found to be less than 4%, 2.6%, and 1.5% respectively of the analytical signals detected at equivalent concentration of ligand and holo-calmodulin while in the presence of calcium.

Kinetic and steady-state analyses were performed as outlined in *Section 5.3* and as first demonstrated with the solution phase interaction of protein A and IgG in *Section 6.2.3*. All kinetic traces presented in Figure 6.12 were fit to a single exponential of the form $y = a(1-e^{-\tau x})$ using nonlinear least squares regression. The parameter τ describes the exponential rise of the molecular interaction. Also called the observed rate, k_{obs}, a qualitative inspection of the association curves in Figure 6.12 indicate τ increases with increasing ligand concentration. This can be deduced theoretically from the law of mass action where the association of a molecular interaction proceeds as a function of concentration and rate. Plotting the observed rate calculated by nonlinear regression of the kinetic traces versus concentration of {*ligand*} yields a linear relationship as seen in Figure 6.13. The best fit lines through the observed rates as determined by the method of least squares exhibit high linearity with the lowest coefficient of variation value obtained across all assays equal to 0.989 for the holo-calmodulin•calcineurin interaction. The least squares analyses of the linear plots in Figure 6.13 was also used to determine the slope and y-intercept of the best fit line through each data set (displayed within each graph) and the respective errors associated with the determination of the parameters. Furthermore, as described in *Section 5.3*, the equilibrium dissociation constant for each calmodulin•{*ligand*} interaction can be calculated by means of the slope and y-intercept determined from the graph of a particular {*ligand*} as these parameters respectively correlate to the on and off rates of the molecular interaction.

End point analyses as described in *Section 5.3* were also performed on each calmodulin•{*ligand*} molecular interaction. Nonlinear regression of the kinetic traces in Figure 6.12 to a single exponential provides a description of the asymptotic region of the plot and thus the steady-state by the parameter a. Charting a as a function of {*ligand*} produces a hyperbolic relationship common to saturation binding experiments as seen by end point graphs of the

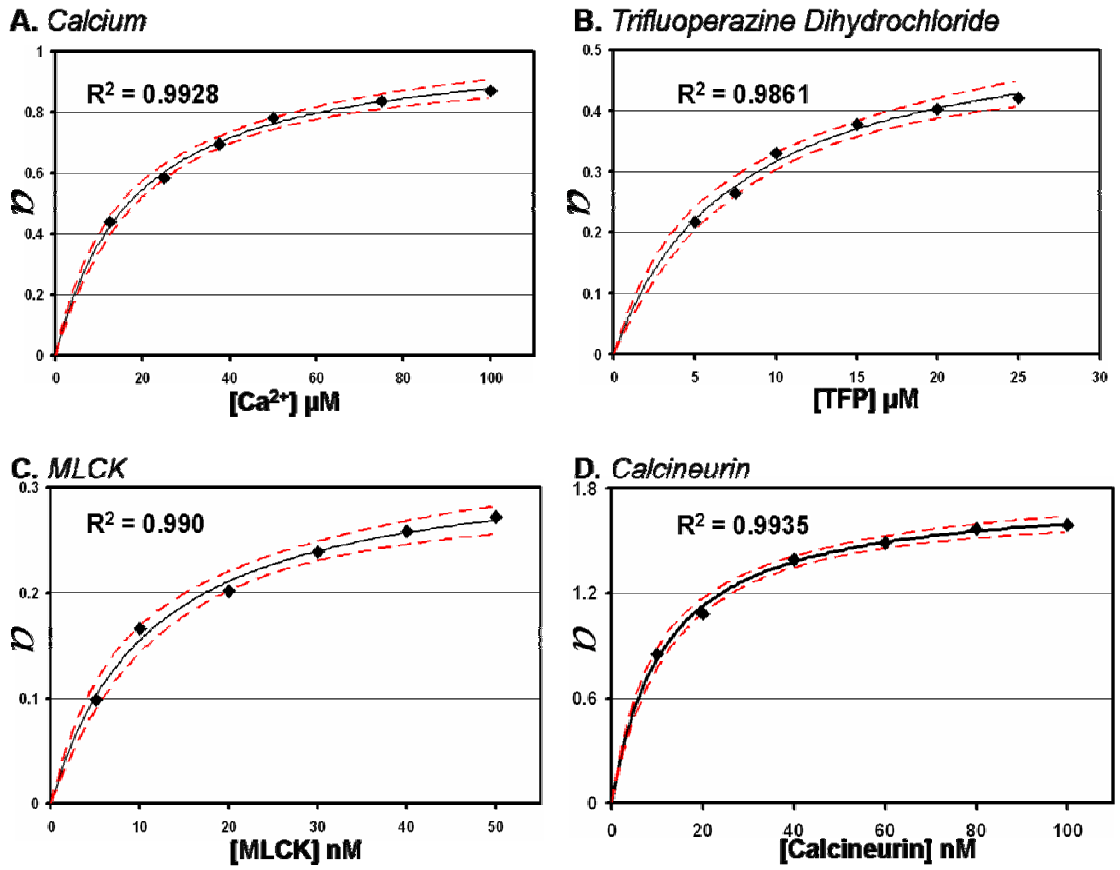

Figure 6.14. Steady-state analyses of the molecular interaction between calmodulin and calcium (A), trifluoperazine dihydrochloride (B), MLCK (C), and calcineurin (D). The parameter a describes the asymptotic region of the association curve and is found by iterative nonlinear regression of said curve. Red traces indicate the 95% confidence limit.

calmodulin interactions displayed in Figure 6.14. Nonlinear least squares fitting of the hyperbolic curve to the steady state binding equation (*Chapter V*, Equation 1) based on the law of mass action allowed a second determination of the equilibrium dissociation constant. The nonlinear fits (black solid lines) of the saturation curves were in close agreement with the end point data presenting R^2 values approaching singularity. The dashed red traces in each graph signify the 95% confidence band of the nonlinear fit. As in *Section 6.2.3*, the biostatistical software package Prism® was employed to fit all end point data and compute K_D for each calmodulin•{*ligand*} molecular interaction using a built-in steady-state parametric fitting routine.

Determinations of the equilibrium dissociation constants obtained in calmodulin interactions through kinetic and steady-state analysis of BI experiments were compared against each other and previously published values in Table 6.1. The equilibrium binding data garnered

by BI detection of the calmodulin interactions agreed well with the literature and fall within the experimental error of K_D values determined by alternative techniques ranging from affinity chromatography, stopped flow fluorescence and SPR. The equilibrium dissociation constants determined by kinetic and steady-state analysis of the raw BI data are also comparable in magnitude offering an intra-system validation of BI obtained results. The largest discrepancy

Table 6.1. Comparison of K_D values for Calmodulin interactions.

Ligand	K_D Determination by BI		*Published Values*
	Kinetic Analysis	Steady-state Analysis	
Calcium	**3.36 µM** (± 5.75)	**17.77 µM** (± 1.55)	*1 – 10 µM*[51]
TFP	**4.73 µM** (± 1.07)	**7.64 µM** (± 0.85)	*4.5 – 5.8 µM*[52]
MLCK	**2.72 nM** (± 0.41)	**11.13 nM** (±1.21)	*~ 6 pM – 10 nM*[24, 48, 49]
Calcineurin	**15.67 nM** (± 5.12)	**11.57 nM** (±0.79)	*4 – 16 nM*[36, 53, 54]

between steady-state and kinetic derived data was seen for the apo-calmodulin•calcium interaction and the holo-calmodulin•MLCK interaction. Reexamination of the raw data (Figure 6.12C) for the holo-calmodulin•MLCK interaction shows significant error in the low frequency component of the traces. As discussed in *Section 5.4*, low frequency noise is crucial to the accurate assessment of the asymptotic region of the graph. This low frequency noise component creates uncertainty in the iterative parameter fitting of a, as partially hinted at by the low R^2 value in Figure 6.14C. The uncertainty is propagated through the end point analysis exacerbating error in the calculation of K_D. There is also some ambiguity in the sequence and source of the MLCK peptide. The MLCK ligand was synthesized and supplied by Applied Biosystems Incorporated (ABI) in a joint collaboration. Initially reported as (but never confirmed) to be M13 by ABI, this target peptide is derived from the binding domain of MLCK in skeletal muscle (sk-MLCK).[44] M13

consists of 26 residues: Lys-Arg-Arg-Trp-Lys-Lys-Asn-Phe-Ile-Ala-Val-Ser-Ala-Ala-Asn-Arg-Phe-Lys-Lys-Ile-Ser-Ser-Ser-Gly-Ala-Leu.[45] This sequence corresponds to C terminal residues 577 – 602 taken from rabbit sk-MLCK. Holo-calmodulin binds M13 with an affinity on the order of 1 – 5 nM.[44, 46] The hydrophobic side chains of residues four (Trp) and seventeen (Phe) interact respectively with the hydrophobic pockets of the C and N terminal domains in the holo-calmodulin complex exposed after coordination with calcium. Deletion of residues 19 – 26 in M13 have been shown to increase CaM affinity by a factor five.[47] The homologous sequence of M13 in smooth muscle MLCK is termed RS20 peptide and has the sequence: Arg-Arg-Lys-Trp-Gln-Lys-Thr-Gly-His-Ala-Val-Arg-Ala-Ile-Gly-Arg-Leu-Ser-Ser-Ser.[48] This serine buried C-terminal sequence also binds holo-CaM with high affinities (K_D = 1.6 nM).[48] The interaction of holo-calmodulin with sm-MLCK has shown markedly increased association kinetics compared with that of sk-MLCK having on-rates increased by as much as an order of magnitude.[46] Slight alterations to the RS20 sequence has further increased holo-CaM affinity for the sm-MLCK sequence with two well studied mutants being known as Trp and Tyr peptides. Deletion of the three C-terminal buried serines (residues 18 – 20), Trp sm-MLCK peptide, has increased affinity 1000-fold (K_D = 6 pM).[46, 49] It is believed ABI may have also used this peptide sequence at times. Substitution of tryptophan at residue four with the less hydrophobic tyrosine, Tyr sm-MLCK peptide, reduces this increased affinity however by diminishing the interaction with the hydrophobic pocket in the C terminal of holo-calmodulin.[49] Kinetic analysis of CaM•MLCK interactions determined by BI experiments show on rates of 3.1×10^7 $M^{-1}s^{-1}$. This positions the kinetics observed by BI just between those of sk-MLCK (10^{-6} $M^{-1}s^{-1}$)[46] and sm-MLCK (10^{-8} $M^{-1}s^{-1}$)[46]. Kinetic data does appear to preclude the Trp and Tyr derivatives of sm-MLCK.[49] The association rate determined by BI agrees best with data obtained by Török for an unidentified version of myosin light chain kinase.[50] However, due to the inactive ABI collaboration and their propensity to limit the information given to us, the exact primary sequence of the initial MLCK protein will likely never be resolved.

The apo-calmodulin calcium interaction has significant errors associated with both the kinetic and steady-state analysis. As seen in Figure 6.13A, the least squares fit of the observed rate of association for CaM•Ca^{2+} is less accurate at describing the data. The increased scatter in

the observed rate of the apo-calmodulin•calcium interaction is most likely due to the increased high frequency noise present in the first ten seconds of binding throughout the middle concentration of calcium kinetic curves (Figure 6.12A). The main source of error in the steady-state analysis of the apo-calmodulin•calcium interaction is due to the fitting routine chosen based on our kinetic model (*Section 5.3*). The kinetic model forces interactions to be fit to a single exponential regardless of the complexity of the system. Higher ordered systems such as apo-calmodulin•calcium, where CaM not only binds four calcium ions but also undergoes a large conformational, are much more aptly described by higher ordered functions, generally a double exponential for interaction studies. The single exponential had difficulty accurately describing the asymptotic region of the binding curve. The fit either tended to over or undershoot the true asymptote with a non-Gaussian distribution of error. This error in accurately parameterizing a causes added uncertainty to the calculation of the equilibrium dissociation constant.

While shortcomings in the kinetic model and data analyses have been acknowledged, initial investigations into a dynamic array of interactions have yielded accurate results with a commonality to previously published values confirmed by alternative detection methodologies. BI has been shown, in the case of the calmodulin interactions, to be widely applicable, highly sensitive and possess a broad dynamic range.

6.4 sHSP Interaction in Free Solution

6.4.1 Background

Proteins spontaneously self assemble into their native conformations under physiological conditions on a sub-second timescale.[55] Yet, there exists a vast array of possibilities by which residues in a protein can efficiently pack with estimates of possible conformations near 10^n (where n is the number of residues). In fact, it is estimated that a protein with 100 residues would need ~ 3.17×10^{79} years to fully explore all conformational possibilities. Proteins must therefore be guided through a largely ordered, quasi-direct pathway. It is thought the primary structure of a protein often dictates its secondary structure by directing a folding pathway.[17] Protein folding is

primarily driven by hydrophobic forces as the side chains of most nonpolar residues coalesce into the interior of the protein. Once folded, native protein conformation is maintained through a net stabilization of forces acting to both fold and unfold the protein. Beyond hydrophobic compaction, the folding mechanism is further satiated by Van der Waals forces and intramolecular hydrogen bonding between nearby residues as well as electrostatic interactions such as salt bridges on the protein surface.[56] While hydrophilic residues on the protein surface add stability through electrostatic interactions, there is also an energetic loss due to desolvation from the same process. The entropic gain of unfolding (a less ordered structure) and hydrogen bonding between solvent and residues with polar side chains are, among others, forces that favor the unfolded state of the protein. In fact, solvent effects play a key role in protein conformation either by attractive forces that destabilize the structure or entropic losses induced by the organization about nonpolar residues.[57, 58]

As noted above, protein structure is energy dependent, accounting for the interaction between adjacent residues and surrounding solvent molecules. The conformational energy of proteins is at a state of dynamic equilibrium. Governed by Le Chatelier's principle, any change induced upon the system will shift the equilibrium in order to minimize the energetic effect. Environmentally or chemically induced stress to the microenvironment of a protein has a profound impact on the overall stability and structure of the molecule. Post-translational modifications (e.g. phosphorylation, deamidification, and oxidation) further reduce the stability of the protein structure, lowering the energy barrier for unfolding. Mutations to the protein sequence are duplicitous in nature with core residue mutations affecting structure while both core and surface amino acid mutations alter thermodynamic stability. Even single point mutations can wreak havoc on protein stability and function. For instance, over 90% of cystic fibrosis patients of European descent possess a CFTR protein lacking phenylalanine at position 508. This single point mutation causes an aberrant conformation of the protein and has been genetically linked to the disease.[59]

Structural unfolding proceeds in a cooperative manner whereby any partial unfolding of the molecule leads to destabilization, further collapsing the entire protein into a random coil.

Increases in temperature, pH, and even concentration can lead to protein unfolding.[17, 56] Chemical denaturants such as detergents or urea can also unfold proteins by disruption and competition with native interactions. Protein misfolding or unfolding followed by aggregation has been reported to cause cytotoxicity and is directly involved in disease pathogenesis.[60] Amyloid deposits formed by the accumulation of insoluble aggregates of misfolded proteins are prevalent in neurodegenerative diseases such as Alzheimer's, Parkinson's, and Huntington's diseases.[61] Spongiform encephalopathies[62], cystic fibrosis[63], and other diseases[64, 65] have been directly linked to aberrant protein structure caused by either folding defects or alterations to the machinery that governs folding.

Partially unfolded, misfolded, and completely unfolded proteins present numerous solvent-exposed hydrophobic regions normally buried in the native state. Exposure of these hydrophobic areas to a polar solvent is thermodynamically unstable. Therefore, denatured proteins tend to seek out each other and bind through hydrophobic interactions in an attempt to shield the exposed hydrophobic areas from the polar solvent. This process is often times irreversible, leading to intra- and intermolecular aggregation followed by precipitation which (as described above) can lead to disease states. In order to prevent unfolding and protein aggregation as well as protect against the possible cytotoxic effects, the body produces proteins that 'sense' defective folding states and can deploy these molecules when stresses are induced in a manner akin to an immune response. Termed molecular chaperones, this family of proteins is essential to the prevention and reversal of aggregation, particularly in multi-domain and multi-subunit proteins.[17] Molecular chaperones repeatedly bind hydrophobic areas exposed in aberrant protein conformations facilitating re-folding to the native state.

While the exact mechanism by which chaperones maintain native protein conformation is not completely understood, it is well known that most members of the chaperone family are heat shock proteins (Hsp). *Hsp* gene transcription is induced by any detrimental changes to the microenvironment such as temperature (i.e. 'heat shock') thereby invoking a robust proliferation of proteins in a stress response.[17, 66-69] Furthermore, *Hsp* transcription is able to proceed rapidly as no time is required to assemble initiation complexes resulting in expeditious heat shock protein

expression.[70] Changes in pH or concentration, introduction of toxins, infections and other stresses to the microenvironment can elicit the same 'heat shock' response.[66, 67] Unlike most other constituents, heat shock proteins are fairly resistant to harsh conditions and can serve to protect and refold proteins denatured by environmental stress/toxic agents.[70, 71] The activation of a heat shock response is also dependant upon the cell, organ, or organism wherein the protein resides. For instance, yeast normally maintain high levels of Hsp and thus a higher basal thermotolerance. Therefore increased temperatures are needed to induce *Hsp* gene transcription in yeast compared to those typically required.[66]

Members of the heat shock protein family exhibiting chaperone activity have highly conserved primary structures across a range of organisms.[66, 67] While their separation into subclasses has yet to be standardized (with 3[67], 4[71], 5[72], and 6[73] subclasses being reported), their nomenclature is generally straightforward. Heat shock proteins are typically named by the molecular weight, in kDa, of their constituent monomer (i.e. Hsp72 consists of a 72 kDa monomer). The heat shock protein family is both diverse in nature and essential to cellular function. Hsp110 and Hsp104 are known to increase tolerance at high temperatures and be involved in adenosine triphosphate (ATP) dependant resolubilization of protein aggregates.[73, 74] Hsp90 is involved in numerous signaling and apoptotic pathways including the erbB2 signaling pathway for activation of Akt and cardiomyocyte survival.[75] Hsp70 and Hsp60 are recognized to refold proteins in an ATP dependant manner with Hsp40 regulating and sustaining the ATP hydrolysis cycle.[17, 76, 77] Hsp70 is also thought to play an important role in spermatogenesis[78] as well as the protection of gastric mucosa from cytotoxic conditions.[79]

Monomers of heat shock proteins encompassing low molecular weights that exhibit chaperone activity are generally grouped into a familial subset of Hsp. Identified as small heat shock proteins (sHsp), this group of molecular chaperones is the least conserved among the entire Hsp family with divergence predicted to be early in evolution.[80, 81] While the size (monomeric MW ranging from 8 – 32 kDa) and sequence fidelity of sHsp are variable throughout the subset, common characteristics are found among the members. Small heat shock proteins are omnipresent in nature with a multitude of functions, the most noted of which is their role in

preventing cytotoxic protein aggregation by mediating folding pathways. Yet, unlike other heat shock proteins, sHsp members function independently of ATP binding and hydrolysis.[82, 83] Small heat shock proteins are also found in high abundance with concentrations reaching 450 mg/mL at selected locations *in vivo*.[84] Although members of the sHsp family have by definition small monomeric units, they are known to form large multimeric complexes ranging from 200 kDa to 1.2 MDa.[85] These multimers form dynamic quaternary structures across the sHsp family (Figure 6.15). A few sHsp members, Hsp16.5 and Hsp26 for example, form well ordered, monodisperse complexes consisting of as many as 24 monomeric subunits.[72] However, the more observed

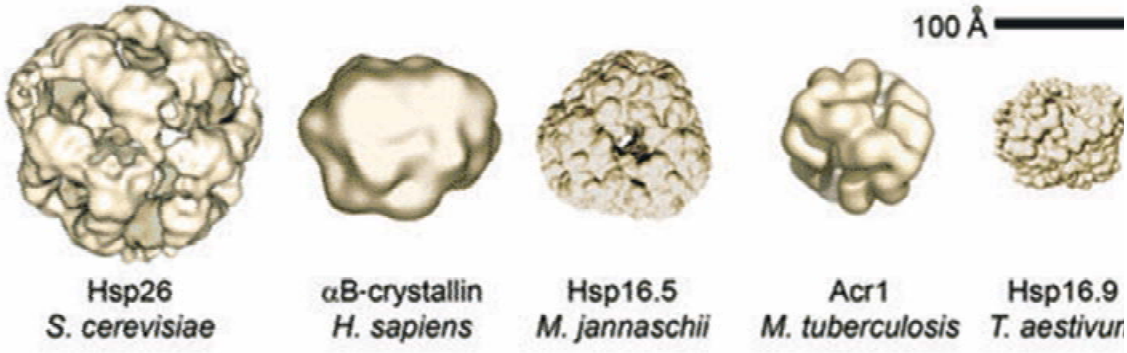

Figure 6.15. Variable quaternary structures of notable sHsp courtesy of Haslbeck, *et.al*.

trend across the family is assembly into polydisperse structures. Multimeric sHsp complexes can exchange subunits at rates of roughly 6×10^{-4} s^{-1}.[86] Subunit exchange between sHsp family members has also been characterized yielding copolymeric structures as exhibited by the formation of α-crystallin from multiple subunits of HspB4 and HspB5.[87] Small heat shock proteins are seen to shift between inactive and active forms possessing moderately low and high affinity for non-native proteins respectively.[80] This shift in activity states is stress induced and has been shown to be accompanied with a dissociation of the sHsp complex through disruption of the subunit contacts. A short peptide sequence (14 residues) at the end of the N-terminal, rich in both proline and alanine, has been determined to be highly involved in the dissociation process.[88] Investigations into the chaperone activity of Hsp27 by Shashidharamurthy *et.al*[89] indicate dissociation of the multimer is essential for the recognition and binding of aberrant proteins.

Dissociation of the sHsp complex is thought to expose previously buried binding sites, a hypothesis further validated by the increase in hydrophobicity exhibited by numerous sHsp under stress.[90]

As noted above, the primary structure of sHsp is not as highly conserved when compared to other heat shock proteins where Hsp70 for instance keeps nearly 50% sequence homology across proteins from both prokaryotic and eukaryotic cell types.[91] However, sHsp are characterized by a noted region of the C-terminus (~ 90 residues) referred to as the α-crystallin domain. The α-crystallin domain is comprised of a β-sheet sandwich followed by a short C terminal extension. The sandwich consists of two layers of antiparallel β-sheets connected by a

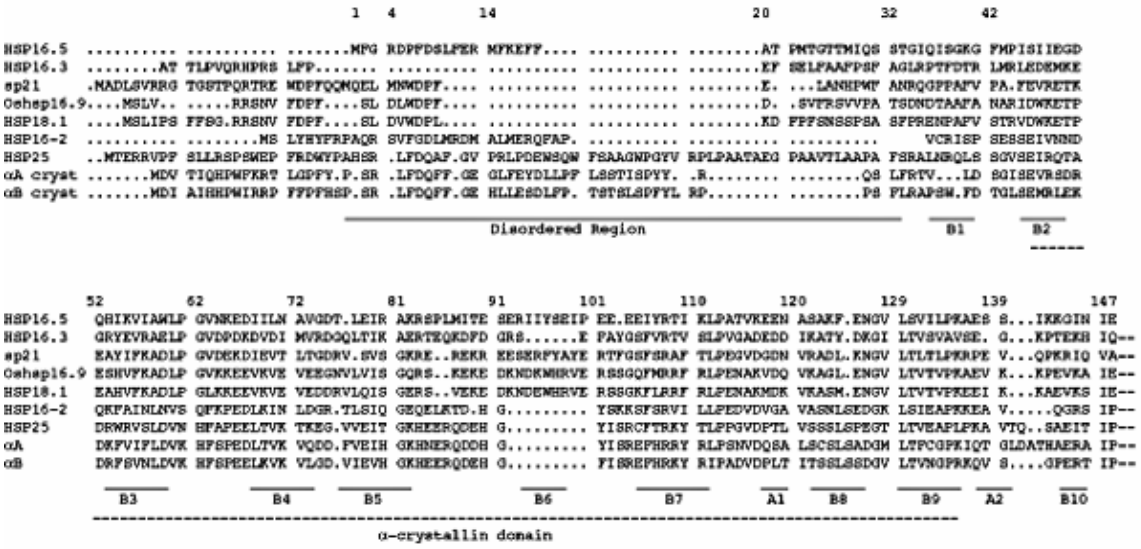

Figure 6.16. Amino acid sequence of selected sHsp underscoring the disordered, hydrophobic N-terminal region and the more conserved α-crystallin domain. Taken from Kim, K.K. *et.al*.

long uncoiled loop containing a short β-sheet itself. While the amino acid sequence of the α-crystallin domain is variable, the compact tertiary structure formed by the β-sheet sandwich is highly conserved within the sHsp family.[92, 93] The α-crystallin domain and flexible C-terminal extension are essential for dimer formation of monomers through subunit interaction (primarily between β-sheets present on the long uncoiled loop).[88, 93] The N-terminal domain has variable length and sequence within the sHsp family. Early attempts at determining the crystal structure of the hydrophobic N-terminal in some sHsp yielded only partially resolved images.[93] Recent

studies by Shi *et.al*[72] have shed new light on this clouded domain. Through a combination of structurally sensitive analytical techniques, investigators were able to determine the N-terminal domain was essential in the symmetry, order and global assembly of sHsp structure.[72]

Well known for their chaperone activity, sHsp also possess other important physiological functions including cellular growth[94], apoptosis[95], and the modulation of actin[96]. Hsp32, also known as heme oxygenase-1 (HO-1), catalyzes the degradation of heme to carbon monoxide, iron, and biliverdin as well as serving in the tissue protection of the gastric mucosa.[71] Hsp25 has been shown to decrease mortality in response to toxic agents[97] and protect colonic mucosa and intestinal epithelial cells from oxidative stress.[98] Additionally, Hsp27 is ubiquitous in human tissue. This small heat shock protein is thought to be involved in oncogenesis and resistance of cancer cells to chemotherapy.[99] Cancer cells have been shown to overexpress Hsp27 potentially aiding their survival and increasing tumor growth and metastasis.[99] Hsp27 and Hsp22 are associated with peripheral neuropathies.[87] Elevated levels of Hsp27 and HspB5 (αB-crystallin) have been found in ischemic heart[100-102] and the brains of patients suffering from neurodegenerative diseases such as Alzheimer's[103], Parkinson's[104], amyotrophic lateral sclerosis (ALS)[105], and others[106, 107]. The earliest identified (and most widely studied) small heat shock protein, α-crystallin, is actually formed from multiple subunits of two distinct sHsp: HspB4 (αA-crystallin) and HspB5 (αB-crystallin). Composing 40% of the protein mass in the mammalian lens, α-crystallin provides the lens with its refractive nature through its concentration gradient.[83] The transparency of the lens is also maintained by α-crystallin's role as a chaperone, preventing light scattering aggregates.[108, 109] Mutations to sHsp can have deleterious physiological effects. Mutations to Hsp27 and Hsp22 have been genetically linked to distal motor neuropathy and Charcot-Marie-Tooth disease.[110-112] Whereas the inhibition of Hsp27 is currently being examined for possible therapeutic effects in cancer treatment.[99] Mutation of αA-crystallin and αB-crystallin at residue 108 (Arg) causes cataract and desmin-related myopathy respectively.[109]

Advanced structural analysis techniques such as cryo-EM (cryo-electron microscopy) and EPR (electron paramagnetic resonance spectroscopy) have provided tremendous insight into the elucidation of sHsp structure left previously unresolved by standard crystallographic techniques.[72]

Determination of the function and thermodynamic properties of these structurally resolved sHsp provides investigators working paradigm for their dynamic behavior, opening up the possibility for truly preventive and therapeutic value. However, the sheer magnitude of potential structural variants and mutant sHsp constructs precludes the use of structural analysis techniques as selection tools. A more robust method is required for pre-screening sHsp deemed functionally relevant for further structural characterization. Optimal screening of sHsp analog libraries should be carried out by a technique capable of analyzing ultra-small volumes and amendable to high throughput formats. Additionally, the preeminent analytical signal should come from a non-derivatized sHsp, as labeling moieties (e.g. fluorophores or radioligands) can reduce protein yields and restrict the number of potential structural variants. With this in mind, BI has been used to characterize the thermodynamic properties of a phosphorylated construct of αB-crystallin. Initial studies into the interaction of this sHsp with a destabilized variant of T4 lysozyme (T4L) were compared to traditional detection methodologies, fluorescence and calorimetry, in a cross-validation of the technique. sHsp are capable of distinguishing aberrant proteins of similar structure varying only in their propensity for non-native, unfolded states. This property of sHsp was used to investigate the specificity afforded by BI in comparing two mutants of T4L possessing nearly identical structures but varying degrees of destabilization. Lastly, a physiologically relevant system was chosen to demonstrate the utility of the BI instrument. A mutation in the αA-crystallin sequence genetically linked to autosomal dominant cataract was studied.[113] Molecular interactions of the mutant with another lens bound protein were analyzed by BI with evaluated kinetic and thermodynamic parameters compared to the popular label-free, surface sensing technique surface plasmon resonance (SPR).

6.4.2 *Site-directed Mutagenesis*

Site-directed mutagenesis was used to form T4L and sHsp constructs using overlap extension PCR as described previously.[114-116] Briefly, synthetic oligonucleotides possessing the desired point mutation were used to generate DNA restriction fragments. PCR fragments were ligated into the appropriate restriction sites. T4L mutants were subcloned into the PBR222 vector

while sHsp constructs were subcloned into the pET 20(b+). All mutants were sequenced to confirm site-specific substitution and absence of any undesired products. Mutations are named throughout this dissertation by specifying the original residue, the number of the residue, and the new residue respectively. For the cataract study, a R49C substitution was introduced into a cysteine-less background of αA-crystallin whereby the cysteine at residue 131 was replaced with alanine to prevent disulfide linkage.

6.4.3 *Expression, Purification, and Labeling*

Competent BL21 (sHSP) or K38 (T4L) cells were transfected with respective mutant plasmids and cultured in Luria-Burtani (LB) broth containing small concentrations of ampicillin overnight at 32°C. This seed culture was then increased in volume and incubated for ~2 - 3 hours at 37ºC or until mid-log phase had been reached. After cooling to room temperature, induction of the *lac operon* from the addition of 0.4 mM IPTG (isopropyl β-D-thioglactopyranoside) allowed T7 RNA polymerase to start the expression of the mutant construct. Protein expression was carried out for 3 hours at 34ºC and 2 hours at ~ 30ºC post-induction for sHsp and T4L respectively. The cells were then harvested by centrifugation. After disposal of the supernatant, the cell pellet was resuspended in lysis buffer and sonicated. Prior to sonication, PMSF (phenylmethylsulfonylfluoride) was added to the suspension and served as a protease inhibitor. A 5% solution of PEI (polyethyleneimine) was added to precipitate DNA (BL21 cell lines only) and was then followed by a second centrifugation step. The supernatant was stored in a Falcon tube and kept at 5ºC overnight.

All T4L mutants were purified by a 2-D separation process. Cation exchange using a Resource S column was used as an initial clean-up step. Immediately following elution, T4L mutants were labeled with monobromobimane in a 10 fold stoichiometric ratio. Reaction of the fluorophore with cysteine at position 151 was allowed to proceed overnight to ensure complete derivatization. Although neither BI nor calorimetry require a labeled analyte for detection, all T4L mutants were fluorescently derivatized and used throughout the experiments to ensure no variability existed between the ligands used in each detection method. Labeled solutions were

further purified by size exclusion chromatography using a Superdex 75 column. The eluted analyte was concentrated using Amicon® centrifugal concentrators and characterized by UV-Vis spectroscopy. Labeling efficiency was determined by monitoring absorbance peaks at 280 and 380 nm. Mutant T4L concentrations were determined at 280 nm using an extinction coefficient of 1.231 cm^2/mg.

Constructs of sHsp were purified in a three step separation process. sHsp were loaded onto a Source Q column for anion exchange and eluted with a sodium chloride gradient. After the eluant concentration had been adjusted to a final concentration of 0.5M ammonium sulfate, sHsp solutions were loaded onto a phenyl-Sepharose column and eluted with a gradient transitioning from 1M to 0M ammonium sulfate. A final purification step was performed by size-exclusion chromatography using a Superose 6 column. Solutions of sHsp were concentrated using centrifugal filters and then characterized by UV-Vis spectroscopy. The concentration of each sHsp construct was determined at 280 nm using the appropriate extinction coefficient.

6.4.4 *BI experimental*

All solutions of T4L and sHsp variants used in BI experiments were buffered with 0.15M $Na_2H_2PO_4$, 0.1M KCl, 0.1mM EGTA, and 0.1% sodium azide. The pH of each solution was adjusted by the addition of small amounts of 5N NaOH or 5N HCl and monitored by a standard pH electrode. Experiments with αB-crystallin and Hsp16.5 were conducted at a pH = 8.0 while interactions with cataract causing mutant of αA-crystallin were run at a pH = 7.2. All solutions were filtered and degassed prior to binding experiments. Solutions were kept on ice during the experiment and briefly allowed to warm to room temperature prior to their introduction into the microchannel. The experimental setup used in all BI investigations of sHsp interactions was the same as defined in *Section 6.1.2*. The mixing chip design used was a hybrid serpentine-hydrodynamic focusing mixer as described in *Section 4.3* and displayed in *Section 6.1.2*. Experiments with αB-crystallin and Hsp16.5 were conducted at 25°C and held stable by a MELCOR temperature controller coupled to a Peltier device. Molecular interactions of the αA-crystallin mutant were performed at a physiologically relevant temperature (37°C). Approximately

4 µL of each sHsp and T4L construct was used in obtaining a single association curve. Binding experiments were monitored in real-time at frequencies ca. 50-100 Hz and in detection volumes on the order of picoliters.

6.4.5 *ITC experimental*

A MicroCal VP-ITC (Isothermal Titration Calorimetry) was employed to cross validate results obtained by BI. Solutions of αB-crystallin and a T4L mutant were buffered at a pH = 7.2 with the same buffer system used in BI experiments. Solutions were kept on ice before the experiment and allowed to warm near the experimental temperature prior to sample introduction. All solutions were filtered through a 0.2 micron disc and degassed before calorimetric experiments. αB-crystallin (~ 1.4 mL) was housed in the sample cell for ITC experiments and had an initial concentration of 12 µM. The buffer solution was kept in the reference cell. Approximately 260 µL of T4L mutant at a concentration equal to 120 µM was drawn into a syringe housed within an automated pipette system. The syringe was placed in the sample cell and spun at 300 RPM. The system was allowed to equilibrate for roughly 2 hours. Once no drift was observed in the baseline and the temperature remained fairly constant, an automated injection sequence was initiated. 10 µL of the T4L mutant was injected into the sample cell containing αB-crystallin twenty-five times with ~ 7 minutes allowed between injections to bring the signal back to baseline. The heat evolved after each injection was recorded and experimental data was analyzed by Origin software to calculate thermodynamic parameters for comparison to BI and fluorescence experiments.

6.4.6 *Detection Method Comparison*

The interaction of sHsp to T4L is a dynamic system (Figure 6.17). T4L can partially or globally unfold, occupying different energy states and thus altering the affinity for sHsp binding. As stated previously, sHsp themselves rapidly exchange subunits and dissociate into different sized multimers.[89] Furthermore, the binding of sHsp to T4L has been shown to be bi-modal with sHsp having low and high affinity sites.[117, 118] In order to determine the viability of BI as an

instrument capable of quantifying binding data in a dynamic system, a well studied construct of αB-crystallin was interrogated against a point mutant of T4L. This same sHsp•T4L system was also evaluated using ITC and was previously characterized by steady-state fluorescence measurements. Thermodynamic comparison of the three techniques allows for a rigid assessment of the accuracy of the BI system.

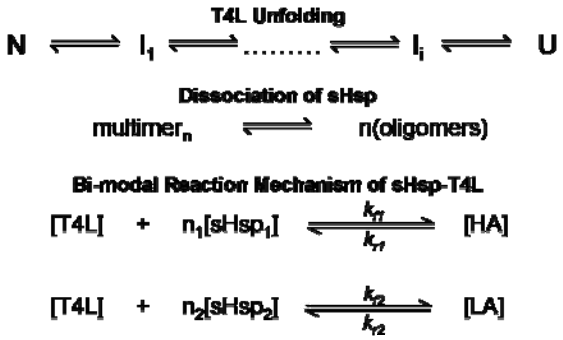

Figure 6.17. The dynamic system of sHsp•T4L is shown including: T4L transition from native state to unfolded protein, dissociation of the sHsp multimer into multiple oligomers, and the bi-modal nature of binding.

The αB-crystallin construct used in this study was a triply substituted analog of the native protein. Serine residues at positions 19, 45, and 59 were mutated to aspartic acids. Since the pK_a of aspartic acid is 3.9, the acid dissociates at biologically relevant pH.[17] This creates a triply charged αB-crystallin species that 'mimics phosphorylation'. Referred to as αB-D3, this sHsp construct has demonstrated increased activity for non-native proteins.[117] A T4L mutant was chosen which had been exhaustively characterized against multiple sHsp.[72, 89, 115-118] With an alanine substituted for leucine at the hydrophobic core position 99, the buried surface area of T4L-L99A is reduced causing enlargement of preexisting cavities.[119] With only minor rearrangement in the core, T4L-L99A is nearly identical in structure to wild-type (WT) T4L. Yet, the thermodynamic stability is measurably reduced after the mutation with Gibb's free energy of unfolding (ΔG_{unf}) lowered by 5.1 kcal/mol.[115, 116]

Molecular interactions using BI were performed with a constant concentration of αB-D3 (10 μM) assayed against multiple concentrations of T4L-L99A. Kinetic traces (black lines) of each ratio of αB-D3 : T4L-L99A as monitored by BI are shown in Figure 6.18A. Visual inspection of the association plots provides an immediate qualitative measure of the experiment. As expected, increases in the concentration of L99A saw a rise in the magnitude of the binding signal detected by BI. Steady-state conditions were unsurprisingly reached more rapidly at higher L99A concentrations as well. All kinetic traces were fit to both a single (not shown) and

double exponential (red traces in Figure 6.18A) by nonlinear least squares regression. A comparison of the square of residuals from each fitting routine produced statistical significance with the double exponential shown to be more apt at describing the data. The observed rates, as determined from the iterative fitting process, exhibit high linearity as a function of L99A concentration with coefficients of variation equal to 0.992 and 0.879 for the fast (red circles) and slow (green circles) rates respectively (Figure 6.18B). The observed rates concentration dependence is predicted by the law of mass action and suggests at least two separate kinetic events are being monitored by BI.

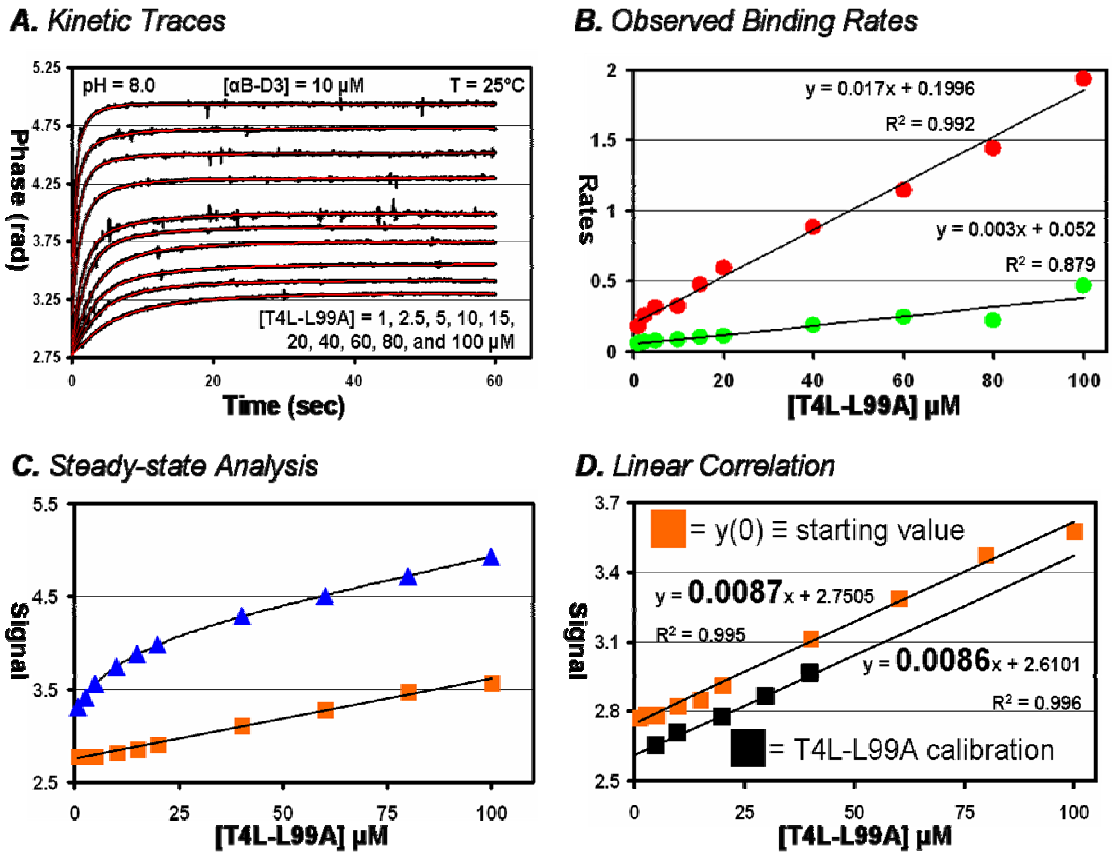

Figure 6.18. The molecular interaction of αB-D3•T4L-L99A was monitored by BI with kinetic traces displayed in **A**. The association curves were fit to a double exponential (red lines in A) with the observed rates plotted as a function of L99A concentration (**B**). Analysis of the steady-state data (blue triangles in **C**) allows for the determination of K_D. The linear rise in starting values of the kinetic traces, as shown by the orange rectangles in **C** and **D**, was attributed to the response of BI to increased concentrations of free L99A as verified by a calibration curve with the same slope in **D**.

While extraction of multiple, highly linear rates from the association curves is promising, the complexity of the sHsp•T4L system forbids the use of the kinetic derivation in *Section 5.3* from quantification of the equilibrium dissociation constant. Instead, a modified version of the steady-state analysis proposed in *Section 5.3* can be employed in the calculation of K_D.[117] Steady-state values were plotted as a function of L99A concentration in Figure 6.18C (blue triangles). However, the plot does not appear to reach saturation, rather it increases linearly at high concentrations of ligand. The initial starting values for each αB-D3•T4L-L99A pair also rises with increasing concentrations of ligand. What appeared at first to be a troublesome observation was eventually determined to be a correctable signaling byproduct. This trend was not seen in previous molecular interaction assays using BI as concentrations of ligands were so small, changes in the amount of free ligand were below the senstitivity of the instrument in its current embodiment. However, the span of high concentrations for T4L used in these BI investigations began to show a linear response with increased amounts of free ligand. Fundamentally, this is expected as BI is foremost a refractive index/concentration detector. A calibration curve of T4L-L99A was therefore run to detect the response of BI to free concentrations of L99A (black squares in Figure 6.18). The slope of the calibration curve matches the slope of the ascending starting values from αB-D3•T4L-L99A binding runs, indicating the rise is due to an increase in

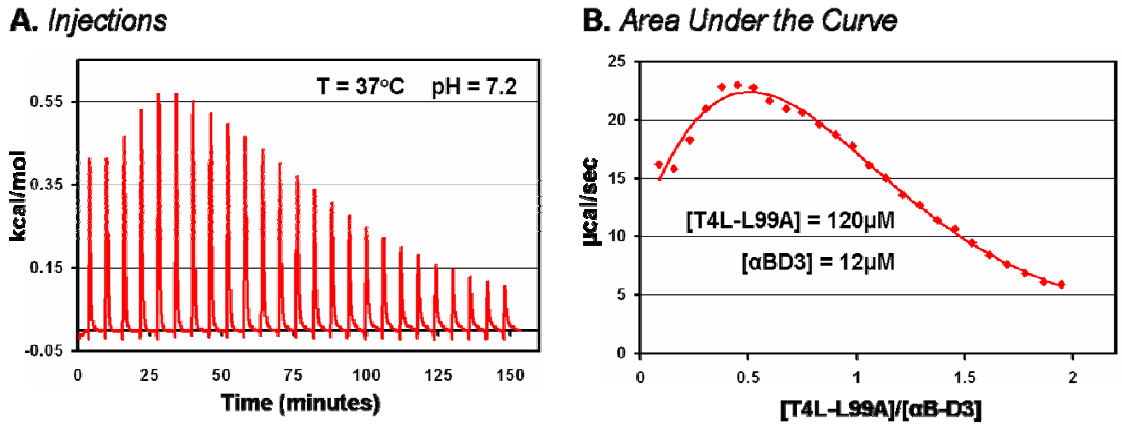

Figure 6.19. Isothermal titration calorimetry (ITC) was used to separately evaluate the αB-D3•T4L-L99A. Heat evolved after each injection (10 µL L99A) was detected (**A**) for 25 injections. The area under the curve was extracted and plotted against the molar ratio to determine thermodynamic data (**B**).

free L99A at high concentrations. Accounting for this slope in the steady-state data amounts to a baseline subtraction of initial starting points and was so performed prior to thermodynamic evaluation.

Analysis of the steady-state data obtained from BI measurements as described by Sathish, *et.al*[117] was compared to thermodynamic data measured by ITC experiments (Figure 6.19) and equilibrium fluorescent analyses. The chief variance among the techniques was seen between the ITC results and those from fluorescence and BI. High affinity binding of αB-D3 to L99A was separated by a factor of two for fluorescence and BI calculations whereas ITC was approximately 10 and 5 fold different respectively. Determination of the low affinity mode exhibited even more precision between the fluorescence and BI assays with K_{D2} values within experimental error of the measurement. Again, determination by ITC was off by a factor of ten. However, the experimental parameters of ITC experiments were altered slightly from those of the fluorescence and BI interactions to improve enthalpy detection for the discrimination of the two binding modes. Previous fluorescent experiments of αB-D3 binding T4L mutants has shown slightly tighter affinity is observed at conditions of pH = 7.2 and T = 37°C compared to the lower temperature and higher pH settings for an equivalent system, a trend observed here with our ITC measurements.[117] As encouraging as these results were in validating BI with other analytical methods, even more attractive is the comparison between the amounts of sample needed to complete each experiment. While ITC and the fluorescence measurements required roughly the same amount of reagent (~ 100 nanomoles each), BI experiments consumed nearly 20 times less sHsp and T4L. The reduced consumption of analyte is an inherent property of BI and is a valuable asset in molecular interaction studies. Different constructs or mutated sequences often times have lower expression yields, limiting the number of analyses that can be performed. In fact, various T4L double mutants only express enough protein to run two experiments with an ITC. This same amount of protein could be run approximately forty times with BI. Even more importantly, thermodynamic data could be obtained using BI with enough sample remaining for further evaluation by other techniques (e.g. cryo-EM for structural analysis).

Table 6.2. Cross-validation of BI results with more standard detection methods. Also shown is the substantial reduction in material needed for BI experiments.

Data	*Standard Analytical Techniques*		
	ITC	Fluorescence	BI
moles of αB-D3 used	24×10^{-9}	$\sim 50 \times 10^{-9}$	1.5×10^{-9}
moles of L99A used	54×10^{-9}	$\sim 50 \times 10^{-9}$	2.93×10^{-9}
n_1	0.25	0.25	0.25
K_{D1} *(μM)*	**0.015**	**0.16**	**0.08**
n_2	1.1	1.0	1.0
K_{D2} *(μM)*	**2.44**	**22.5**	**25.3**

6.4.7 *Distinguishing Binding Affinity*

Investigations into the chaperone function of small heat shock proteins offer the quintessential test for a 'resolution of binding affinity'. As mentioned previously, sHsp can bind proteins with the same structure at different affinities based on the propensity of each protein to inhabit non-native states. Site-directed mutagenesis of T4L allows a scaffold of free energies to be built and further interrogated by a sHsp. Here we use two T4L mutants with near identical tertiary structure, but slightly different Gibb's free energies of unfolding in comparing the affinity each elicits from αB-D3. Our hypothesis being that αB-D3 will bind the least destabilized mutant of T4L with the highest affinity.

Results obtained from the interaction of αB-D3 to T4L-L99A in *Section 6.4.6* were used in this study with L99A serving as the more destabilized mutant. A second mutant, T4L-D70N, replaces an aspartic acid at residue 70 in the native state with an asparagine. The substitution of the uncharged asparagine disrupts the normal salt bridge between aspartic acid at position 70 and histidine at position 31. The Gibb's free energy of unfolding for D70N is 9.2 kcal/mol

establishing another mutant far less stable than the wild type T4L ($\Delta\Delta G_{unf}$ = -4.8 kcal/mol) but not as destabilized as L99A ($\Delta\Delta G_{unf}$ = +1.3 kcal/mol). The interaction of αB-D3 and T4L-D70N was performed in the same manner as those for αB-D3•T4L-L99A in *Section 6.4.6* and using the same BI setup. The association of sHsp with multiple concentrations of T4L was monitored in real-time by BI with the signal output for each αB-D3•T4L-D70N mixture displayed in Figure 6.20A. Binding data was analyzed with a nonlinear least squares fitting routine using both a

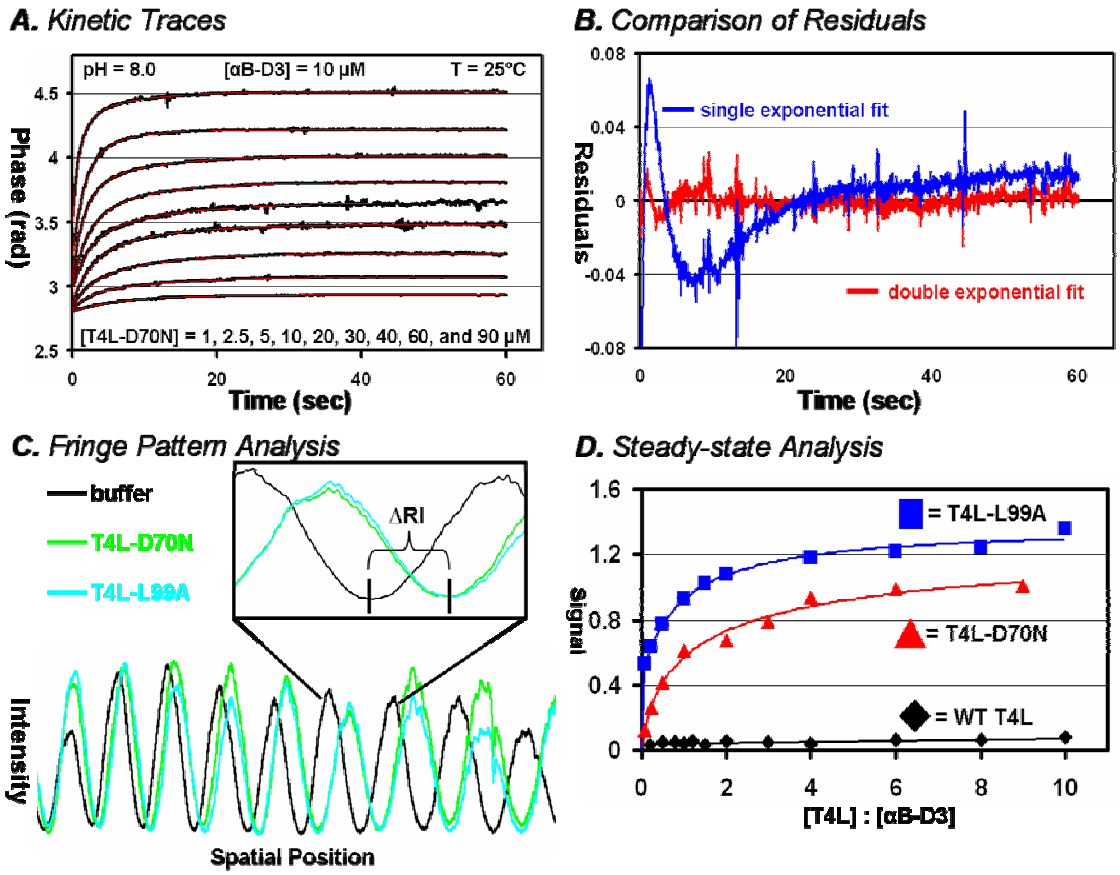

Figure 6.20. αB-D3 binding multiple concentrations of T4L-D70N was monitored by BI with kinetic traces displayed in **A**. The association curves were fit to a single (blue) and double (red) exponential with the residuals for [T4L-D70N] = 90 μM displayed in **B**. The double exponential was statistically superior at fitting the kinetic data. Interference patterns recorded by BI are shown for both T4L mutants in **C**. The overlap in the fringe patterns of the mutants demonstrates BI is insensitive to inherent differences in their stabilities. A zoomed in region of the T4L mutants interference patterns are shown and compared to a pattern from a buffer solution indicating the sensitivity of the instrument to changes in refractive index. Analysis of the steady-state data (**D**) clearly shows the magnitude of binding as detected by BI for αB-D3•T4L-L99A is significantly greater than seen with αB-D3•T4L-D70N. As a control, αB-D3 was assayed against multiple concentrations of WT-T4L, exhibiting no binding across the concentration range.

single and double exponential. As seen in Figure 6.20B, the double exponential approach provided a statistically significant improvement in describing the kinetic data in comparison to the single exponential routine. Another key note is presented in Figure 6.20C. The interference patterns recorded by BI when a D70N, L99A, or buffer solution was contained within the microfluidic channel are shown. The fringe patterns produced for the two T4L mutants precisely overlap with point-to-point minima matching. Other than minor intensity fluctuations (which our analysis is insensitive to), BI does not distinguish between the inherent destabilization differences in the two mutants. This observation was also seen with other T4L mutants as well, some doubly mutated and even more destabilized (data not shown). The zoomed in view of the fringe pattern demonstrates the sensitivity BI has in regard to refractive index, with a substantial shift seen between the interference patterns of the T4L mutants and the buffer.

As described earlier, a D70N calibration was calculated and used for baseline subtraction of the initial starting values. Steady-state data from the αB-D3•T4L-D70N interactions was then compared to the earlier results with L99A. Immediately a qualitative difference was seen in the magnitude of the signals obtained from steady-state data (Figure 6.20D). An ~ 25% reduction in the magnitude of the binding signal observed for D70N is measured in comparison to L99A at equivalent αB-D3 : T4L ratios. Binding of the sHsp to L99A is also observed to reach saturation quicker. Interactions (or lack thereof) between αB-D3 and WT-T4L served as the perfect intra-system control. As wild type T4L is not an aberrant protein and will maintain a native state conformation, αB-D3 should not seek out and bind the protein. αB-D3 was therefore assayed against multiple concentrations of WT-T4L to serve as the control. No discernable binding signal was detected across the entire concentration range as the measurements were within the noise level. Quantitative analysis of the steady-state data for both T4L mutants binding αB-D3 verifies our hypothesis (Table 6.3). Results from BI experiments indicate αB-D3 binding to the T4L mutants in the high affinity mode increases by a factor of 20 for the more destabilized mutant, L99A. The interaction of αB-D3 and D70N in the low affinity mode was also shown to be less favored as K_{D2} was nearly doubled. These results clearly indicate that BI is capable of measuring molecular interactions with high specificity, resolving binding of a sHsp to structurally homologous

lysozymes differing only in their unfolding energies by 1.3 kcal/mol (an energy equivalent to ~ 12 hydrogen bonds).

Table 6.3. Analysis of Thermodynamic Data for Variably Destabilized Mutants of T4L.

Data	*[αB-D3] = 5 μM*	*[αB-D3] = 10 μM*	
	WT-T4L	T4L-D70N	T4L-L99A
ΔG_{unf} *(kcal/mol)*	14	9.2	7.9
n_1	UND	0.25	0.25
K_{D1} *(μM)*	**UND**	**1.68**	**0.08**
n_2	UND	1.0	1.0
K_{D2} *(μM)*	**UND**	**42.1**	**25.3**

UND = undectable

6.4.8 *α-crystallin and Its Role in Cataract*

Crystallins are structural proteins found in the lens of vertebrates comprising ~ 90% of its dry weight. Among the most abundant crystallins, there exists three families: α, β, and γ themselves totaling ~ 40% of the protein content in the mammalian lens where concentrations can reach 450 mg/mL.[84] A member of the sHSP family, α-crystallin exists as a polydisperse aggregate (averaging ~ 800 kDa). As mentioned previously, α-crystallin consists of 2 subunits: αA and αB where A and B stand for acid and base respectively. Each monomeric subunit has a molecular mass of ~ 20 kDa with a primary sequence homology of 57%. Subunit exchange between αA and αB is prevalent resulting in a multitude of various constructs and hence the polydispersity of α-crystallin. As stated earlier, αB-crystallin is found throughout the body and has been detected at high levels in diseased states of the heart and brain.[100, 101, 104, 106, 107] Conversely, expression of αA-crystallin is primarily restricted to the lens.[120] Together, these two

sHsp help maintain the function of the lens by preventing aberrant protein aggregation. Mutations to the crystallins have been genetically linked to cataract formation.[121]

Of the 40 – 45 million individuals in the world who are blind, over 50% are due to cataract, with that number expected to double by the year 2020.[122] In the United States alone, approximately half the population between the ages 60 – 74 have cataracts. That percentage rises to over 70% for citizens 75 and older. While there has been recent work with drug compounds for cataract that show some therapeutic ophthalmic effect[123, 124], restoration of vision is predominantly met by surgery. In fact, during the late 1990's 1.35 million operations per year were performed in the U.S. resulting in a total cost of 3.4 billion dollars.[125] In most current surgeries, a small corneal incision (≤ 3 mm) is made and a high frequency ultrasonic probe is inserted. Energy delivered through the probe emulsifies the lens with particulates aspirated back through the probe in a process termed phacoemulsification. An intraocular lens is then inserted into either the posterior or anterior chamber, generally restoring visual acuity to 20/40.[122] As with all surgeries, there are inherent risks and complications associated with cataract removal such as posterior-capsule rupture and clinical cystoid. Asbell, *et.al*[122] give a very detailed summary of the complications involved in cataract surgery. They report the most frequently incurred complication is the post-operative opacification of the posterior-capsule, often called secondary cataract. The rate of occurrence of secondary cataract was reported to be 25% within a 5 year period after surgery.[126] Secondary cataracts are often removed by laser therapy.

The lack of cellular turnover in the lens and the rates/thermodynamics associated with protein unfolding and aggregation imply that if a person lives long enough they will inevitably develop cataracts. Age-related or senile cataracts are the most common form of cataract coupled to a loss in visual acuity. Factors of personal choice such as smoking, use of alcohol, and exposure to UV light are associated with increased occurrence of cataract. Trauma to the eye and drug-induced changes are also shown to cause cataractogenesis. Additionally, genetic defects and developmental abnormalities can induce cataract formation. Nearly 50% of nuclear cataracts are thought to be related to genetic factors and one-third of all cataract cases may have an underlying genetic cause.[127, 128]

Here we demonstrate the utility of the BI system by studying a singly point-mutated αA-crystallin sequence genetically linked to autosomal dominant cataract. Mackay, *et.al*[113] identified a missense mutation in the *HspB4* gene on chromosome 21q caused the formation of nuclear cataract. The point mutation underlying cataractogenesis was determined to be a replacement of arginine for cysteine at residue 49 (αA-R49C). αA-R49C was the first mutation found outside the conserved α-crystallin domain which gave rise to autosomal dominant cataract. The position of the mutation in the N-terminus is structurally significant when compared to most other mutations genetically linked to cataract are buried in the β-sheets of the α-crystallin domain. The N-terminus has been reported to be highly involved in the global assembly of sHsp (particularly αA-crystallin) subunits into well ordered quaternary structure.[72, 86, 129] The highly reactive thiol present on the cysteine substitution is capable of unwarranted disulfide linkage, defeating the binding selectivity for aberrant proteins associated with the chaperone function of the sHsp. In fact, evidence from cellular studies by Mackay, *et.al*[113] suggest the deleterious effect of the mutated protein was caused by a 'toxic gain' in function, whereby αA-R49C no longer selectively bound destabilized proteins but all proteins equipotentially.

To ensure physiological relevance, binding studies of αA-R49C were performed with another protein found in the lens, βB1-crystallin. In a departure from earlier experiments, the interaction of αA-R49C with βB1 was monitored at a pH of 7.2 and at 37°C with temperature stability provided by a Melcor temperature controller coupled to a thermoelectric Peltier device. Other experimental conditions and the optical setup were kept consistent with our earlier sHsp studies. αA-R49C was kept at a constant concentration of 15 μM throughout the experiment. Multiple concentrations of βB1-crystallin were assayed against the αA-crystallin. Again, reactants were mixed

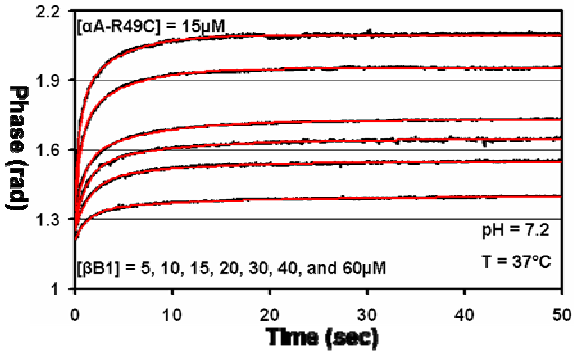

Figure 6.21. Interaction of αA-R49C-crystallin with multiple concentrations of βB1-crystallin at physiologically relevant conditions as detected by BI.

in a microfluidic chip similar to a stop-flow method. Binding events were detected by BI in an ~ 630 pL probe volume and displayed in Figure 6.21. A similar system was studied by Kamei, *et.al*[130] with the use of SPR. There, αA-crystallin was immobilized onto a gold substrate. β-crystallin was passed over the substrate bound αA-crystallin for 25 minutes at a flow rate of 2 μL/min. Regeneration of the surface was accomplished by introduction of a 15 μL solution of 0.1M sodium acetate and 0.15M sodium chloride at a pH of 2.3. As mentioned earlier (*Section 2.3*), there are many drawbacks associated with SPR experiments not the least of which is the possible loss of function caused by immobilization of an analyte, here αA-crystallin, to the surface. This possibility was further exasperated by the use of a low pH solution to 'regenerate' the SPR surface.

Here again the kinetic derivation arrived at in *Chapter 5* fails to accurately describe the kinetics as the assumption of $[L]>[R]$ is invalid. In order to accurately determine the reaction kinetics from αA-R49C experiments for comparison with the SPR results, the knowledge of Dr. Richard Stein and Dr. Hassane Mchaourab was enlisted. A new kinetic model was developed for a two mode binding system with the generic interaction described as

$$\begin{aligned} R_1 + L_F &\leftrightarrow LB_1 \\ R_2 + L_F &\leftrightarrow LB_2 \end{aligned}, \qquad \text{Eqn. 1}$$

where R_i is the amount of free sHsp binding sites per monomer for species i, L_F is the amount of free ligand (in this case βB1-crystallin), and L_{Bi} is the amount of ligand bound for species i. The kinetic rates were then described by the following equations:

$$\frac{dL_f}{dt} = -(k_{f1}R_1 + k_{f2}R_2)L_F + (k_{r1}L_{B1} + k_{r2}L_{B2}) \qquad \text{Eqn. 2}$$

$$\frac{dL_{B1}}{dt} = k_{f1}R_1L_F - k_{r1}L_{B1} \qquad \text{Eqn. 3}$$

$$\frac{dL_{B2}}{dt} = k_{f2}R_2L_F - k_{r2}L_{B2} \qquad \text{Eqn. 4}$$

$$\frac{dR_1}{dt} = k_{f1}R_1L_F + k_{r1}L_{B1} \qquad \text{Eqn. 5}$$

$$\frac{dR_2}{dt} = k_{f2}R_2L_F + k_{r2}L_{B2} \quad , \qquad \text{Eqn. 6}$$

where k_{fi} and k_{ri} are the forward and reverse rates of the binding reactions in Equation 1 respectively. The complete data set of interactions between αA-R49C and βB1-crystallin as detected by BI in real-time was fit simultaneously to these rate equations using the same parameters (i.e. global analysis). The BI data was described well using this global analysis with fits very similar to those obtained by fitting each kinetic trace to a double exponential independently. Results obtained from the global analysis are shown in Table 6.4 and compared to data obtained by Kamei, *et.al*[130]. The kinetic data determined for the low affinity binding mode was similar for both BI and SPR with forward and reverse rates separated by 20% and 33% respectively. While this result is somewhat unexpected given the error often seen in SPR kinetic data, the likelihood experimental conditions contributed to the precision of values is high. However, as seen in columns 5 – 7 of Table 6.4, SPR was unable to distinguish a high affinity binding mode clearly determined by BI experiments. BI results were also found to be in agreement with fluorescent data published by Koteiche, *et.al*[118].

Table 6.4. Kinetic parameters obtained by global analysis of BI data with a comparison to SPR data.

Method	k_{f1} ($M^{-1}s^{-1}$)	k_{r1} (s^{-1})	K_{D1} (μM)	k_{f1} ($M^{-1}s^{-1}$)	k_{r1} (s^{-1})	K_{D2} (μM)
SPR	5230	0.093	17.8	UND	UND	UND
BI	4270	0.062	14.5	37277	0.16	4.16

6.5 Summary

The biotin/avidin surface chemistry significantly simplified substrate preparation, was compatible with PDMS, and facilited immobilized biomolecular assays with BI. Combining this new surface chemistry with the CCD-FFT transduction has allowed improved detection for P_A/IgG

binding by 2 orders of magnitude[2]. BI was also used to monitor DNA hybridization over a wide range of concentrations and allowed discrimination in binding of a 3 base pair mismatch.

Solution phase molecular interactions were shown to be feasible using BI for determining kinetic and thermodynamic data. A cadre of calmodulin interactions was performed on-chip with a dynamic range of binding affinities ranging from μM – nM in K_D with results determined by BI matched well with the scientific literature. BI was also successfully compared to alternative methods in an effort to cross validate the method. Fluorescent and calorimetric experiments provided similar results to those obtained by BI for the interaction of a sHsp construct with a mutant lysozyme. Additionally, BI was able to successfully discriminate chaperone function of a sHSP against mutants of varying stability. Lastly, a physiologically relevant system was studied in which one reactant is genetically linked to the formation of autosomal dominant cataract.

The use of PDMS microfluidic chips and the exceedingly simple optical train of BI represent a cost-effective platform for label-free molecular interaction determinations as well as reversible biological interactions within picoliter volumes and at attomole sensitivity. This technology is inherently compatible with large-scale integration and should facilitate high throughput assays.

(1) Latham, J. C.; Markov, D. A.; Sorensen, H. S.; Bornhop, D. J. *Angewandte Chemie-International Edition* **2006**, *45*, 955-958.

(2) Markov, D. A.; Swinney, K.; Bornhop, D. J. *Journal of the American Chemical Society* **2004**, *126*, 16659-16664.

(3) Sorensen, H. S.; Larsen, N. B.; Latham, J. C.; Bornhop, D. J.; Andersen, P. E. *Applied Physics Letters* **2006**, *89*, -.

(4) Swinney, K.; Bornhop, D. J. *Applied Spectroscopy* **2000**, *54*, 1485-1489.

(5) Kerby, M. B.; Legge, R. S.; Tripathi, A. *Analytical Chemistry* **2006**, *78*, 8273-8280.

(6) Brooks, S. A.; Ambrose, W. P.; Kuhr, W. G. *Analytical Chemistry* **1999**, *71*, 2558-2563.

(7) Brooks, S. A.; Dontha, N.; Davis, C. B.; Stuart, J. K.; O'Neill, G.; Kuhr, W. G. *Analytical Chemistry* **2000**, *72*, 3253-3259.

(8) Chilkoti, A.; Stayton, P. S. *Journal of the American Chemical Society* **1995**, *117*, 10622-10628.

(9) Whitesides, G. M.; Ostuni, E.; Takayama, S.; Jiang, X. Y.; Ingber, D. E. *Annual Review of Biomedical Engineering* **2001**, *3*, 335-373.

(10) Brockman, J. M.; Frutos, A. G.; Corn, R. M. *Journal of the American Chemical Society* **1999**, *121*, 8044-8051.

(11) Saha, K.; Bender, F.; Gizeli, E. *Analytical Chemistry* **2003**, *75*, 835-842.

(12) Langone, J. J. *Advances in Immunology* **1982**, *32*, 157-252.

(13) Davis, M. M. *Annual Review of Biochemistry* **1990**, *59*, 475-496.

(14) Thiel, A. J.; Frutos, A. G.; Jordan, C. E.; Corn, R. M.; Smith, L. M. *Analytical Chemistry* **1997**, *69*, 4948-4956.

(15) Cao, Y. W. C.; Jin, R. C.; Mirkin, C. A. *Science* **2002**, *297*, 1536-1540.

(16) Vinet, F.; Chaton, P.; Fouillet, Y. *Microelectronic Engineering* **2002**, *61-2*, 41-47.

(17) Voet, D.; Voet, J. *Biochemistry*, 2nd ed.; John Wiley and Sons Inc.: New York, 1995.

(18) Capra, J. D.; Edmundson, A. B. *Sci Am* **1977**, *236*, 50-59.

(19) Cohen, I. R. *Sci Am* **1988**, *258*, 52-60.

(20) Davies, D. R.; Chacko, S. *Accounts of Chemical Research* **1993**, *26*, 421-427.

(21) Davies, D. R.; Padlan, E. A.; Sheriff, S. *Annual Review of Biochemistry* **1990**, *59*, 439-473.

(22) French, D. L.; Laskov, R.; Scharff, M. D. *Science* **1989**, *244*, 1152-1157.

(23) Rawn, J. *Biochemistry*; Harper and Row: New York, 1983.

(24) Peersen, O. B.; Madsen, T. S.; Falke, J. J. *Protein Science* **1997**, *6*, 794-807.

(25) Evenas, J.; Thulin, E.; Malmendal, A.; Forsen, S.; Carlstrom, G. *Biochemistry* **1997**, *36*, 3448-3457.

(26) Haiech, J.; Klee, C. B.; Demaille, J. G. *Biochemistry* **1981**, *20*, 3890-3897.

(27) Martin, S. R.; Masino, L.; Bayley, P. M. *Protein Sci* **2000**, *9*, 2477-2488.

(28) Linse, S.; Helmersson, A.; Forsen, S. *J Biol Chem* **1991**, *266*, 8050-8054.

(29) Zhang, M.; Tanaka, T.; Ikura, M. *Nat Struct Biol* **1995**, *2*, 758-767.

(30) Finn, B. E.; Evenas, J.; Drakenberg, T.; Waltho, J. P.; Thulin, E.; Forsen, S. *Nat Struct Biol* **1995**, *2*, 777-783.

(31) Nemirovskiy, O.; Giblin, D. E.; Gross, M. L. *J Am Soc Mass Spectrom* **1999**, *10*, 711-718.

(32) Crivici, A.; Ikura, M. *Annu Rev Biophys Biomol Struct* **1995**, *24*, 85-116.

(33) Finn, B. E.; Forsen, S. *Structure* **1995**, *3*, 7-11.

(34) Levin, R. M.; Weiss, B. *Mol Pharmacol* **1977**, *13*, 690-697.

(35) Prozialeck, W. C.; Weiss, B. *J Pharmacol Exp Ther* **1982**, *222*, 509-516.

(36) Klee, C. B.; Krinks, M. H. *Biochemistry* **1978**, *17*, 120-126.

(37) Klee, C. B.; Draetta, G. F.; Hubbard, M. J. *Adv Enzymol Relat Areas Mol Biol* **1988**, *61*, 149-200.

(38) Aitken, A.; Klee, C. B.; Cohen, P. *Eur J Biochem* **1984**, *139*, 663-671.

(39) Anglister, J.; Grzesiek, S.; Wang, A. C.; Ren, H.; Klee, C. B.; Bax, A. *Biochemistry* **1994**, *33*, 3540-3547.

(40) Kakalis, L. T.; Kennedy, M.; Sikkink, R.; Rusnak, F.; Armitage, I. M. *FEBS Lett* **1995**, *362*, 55-58.

(41) Klee, C. B.; Ren, H.; Wang, X. *J Biol Chem* **1998**, *273*, 13367-13370.

(42) Clipstone, N. A.; Crabtree, G. R. *Nature* **1992**, *357*, 695-697.

(43) Batiuk, T. D.; Kung, L.; Halloran, P. F. *J Clin Invest* **1997**, *100*, 1894-1901.

(44) Blumenthal, D. K.; Takio, K.; Edelman, A. M.; Charbonneau, H.; Titani, K.; Walsh, K. A.; Krebs, E. G. *Proceedings of the National Academy of Sciences of the United States of America* **1985**, *82*, 3187-3191.

(45) Ikura, M.; Clore, G. M.; Gronenborn, A. M.; Zhu, G.; Klee, C. B.; Bax, A. *Science* **1992**, *256*, 632-638.

(46) Montigiani, S.; Neri, G.; Neri, P.; Neri, D. *Journal of Molecular Biology* **1996**, *258*, 6-13.

(47) Findlay, W. A.; Martin, S. R.; Beckingham, K.; Bayley, P. M. *Biochemistry* **1995**, *34*, 2087-2094.

(48) Lukas, T. J.; Burgess, W. H.; Prendergast, F. G.; Lau, W.; Watterson, D. M. *Biochemistry* **1986**, *25*, 1458-1464.

(49) Torok, K.; Trentham, D. R. *Biochemistry* **1994**, *33*, 12807-12820.

(50) Torok, K. *Biochem Soc Trans* **2002**, *30*, 55-61.

(51) Starovasnik, M. A.; Su, D. R.; Beckingham, K.; Klevit, R. E. *Protein Science* **1992**, *1*, 245-253.

(52) Massom, L.; Lee, H.; Jarrett, H. W. *Biochemistry* **1990**, *29*, 671-681.

(53) Hubbard, M. J.; Klee, C. B. *Journal of Biological Chemistry* **1987**, *262*, 15062-15070.

(54) Speaker, M. G.; Orlow, S. J.; Sturgill, T. W.; Rosen, O. M. *Proceedings of the National Academy of Sciences of the United States of America-Biological Sciences* **1983**, *80*, 329-333.

(55) Karp, G. *Cell and Molecular Biology*; John Wiley & Sons, INC.: New York, 1996.

(56) de Paula, J. a. A., P. *Physical Chemistry*, 7th ed.; W. H. Freeman, 2001.

(57) Ben-Naim, A. *Biopolymers* **1990**, *29*, 567-596.

(58) Ben-Naim, A.; Ting, K. L.; Jernigan, R. L. *Biopolymers* **1990**, *29*, 901-919.

(59) Kerem, B.; Rommens, J. M.; Buchanan, J. A.; Markiewicz, D.; Cox, T. K.; Chakravarti, A.; Buchwald, M.; Tsui, L. C. *Science* **1989**, *245*, 1073-1080.

(60) Bucciantini, M.; Giannoni, E.; Chiti, F.; Baroni, F.; Formigli, L.; Zurdo, J.; Taddei, N.; Ramponi, G.; Dobson, C. M.; Stefani, M. *Nature* **2002**, *416*, 507-511.

(61) Forman, M. S.; Lee, V. M.; Trojanowski, J. Q. *Trends Neurosci* **2003**, *26*, 407-410.

(62) Horwich, A. L.; Weissman, J. S. *Cell* **1997**, *89*, 499-510.

(63) Gelman, M. S.; Kopito, R. R. *J Clin Invest* **2002**, *110*, 1591-1597.

(64) Ye, Q.; Hu, Y. F.; Zhong, H.; Nye, A. C.; Belmont, A. S.; Li, R. *J Cell Biol* **2001**, *155*, 911-921.

(65) Yu, M. H.; Lee, K. N.; Kim, J. *Nat Struct Biol* **1995**, *2*, 363-367.

(66) Parsell, D. A.; Taulien, J.; Lindquist, S. *Philosophical Transactions of the Royal Society of London Series B-Biological Sciences* **1993**, *339*, 279-286.

(67) Itoh, H.; Tashima, Y. *International Journal of Biochemistry* **1991**, *23*, 1185-1191.

(68) Tissieres, A.; Mitchell, H. K.; Tracy, U. M. *J Mol Biol* **1974**, *85*, 389-398.

(69) Ritossa, F. *Experentia* **1962**, *18*, 571-573.

(70) Lodish, H.; Berk, A.; Zipursky, S.; Matsudaira, P.; Baltimore, D.; Darnell, J. *Molecular Cell Biology*, 4th ed.; W.H. Freeman and Company: New York, 2000.

(71) Otaka, M.; Odashima, M.; Watanabe, S. *Biochemical and Biophysical Research Communications* **2006**, *348*, 1-5.

(72) Shi, J.; Koteiche, H. A.; McHaourab, H. S.; Stewart, P. L. *J Biol Chem* **2006**, *281*, 40420-40428.

(73) Munchbach, M.; Dainese, P.; Staudenmann, W.; Narberhaus, F.; James, P. *Eur J Biochem* **1999**, *264*, 39-48.

(74) Schirmer, E. C.; Glover, J. R.; Singer, M. A.; Lindquist, S. *Trends Biochem Sci* **1996**, *21*, 289-296.

(75) Gabrielson, K.; Bedja, D.; Pin, S.; Tsao, A.; Gama, L.; Yuan, B.; Muratore, N. *Cancer Res* **2007**, *67*, 1436-1441.

(76) Alberts, B.; Johnson, A.; Lewis, J.; Raff, M.; Roberts, K.; Walter, P. *Molecular Biology of the Cell*, 4th ed.; Garland Science: New York, 2002.

(77) Qiu, X. B.; Shao, Y. M.; Miao, S.; Wang, L. *Cell Mol Life Sci* **2006**, *63*, 2560-2570.

(78) Huang, S. Y.; Tam, M. F.; Hsu, Y. T.; Lin, J. H.; Chen, H. H.; Chuang, C. K.; Chen, M. Y.; King, Y. T.; Lee, W. C. *Theriogenology* **2005**, *64*, 1940-1955.

(79) Watanabe, D.; Otaka, M.; Mikami, K. I.; Yoneyama, K.; Goto, T.; Miura, K.; Ohshima, S.; Lin, J. G.; Shibuya, T.; Segawa, D.; Kataoka, E.; Konishi, N.; Odashima, M.; Sugawara, M.; Watanabe, S. *Journal of Gastroenterology* **2004**, *39*, 724-733.

(80) Haslbeck, M.; Franzmann, T.; Weinfurtner, D.; Buchner, J. *Nat Struct Mol Biol* **2005**, *12*, 842-846.

(81) Kappe, G.; Leunissen, J. A.; de Jong, W. W. *Prog Mol Subcell Biol* **2002**, *28*, 1-17.

(82) Haslbeck, M.; Buchner, J. *Prog Mol Subcell Biol* **2002**, *28*, 37-59.

(83) Haley, D. A.; Horwitz, J.; Stewart, P. L. *J Mol Biol* **1998**, *277*, 27-35.

(84) Horwitz, J. *Exp Eye Res* **2003**, *76*, 145-153.

(85) Kim, K. K.; Kim, R.; Kim, S. H. *Nature* **1998**, *394*, 595-599.

(86) Bova, M. P.; McHaourab, H. S.; Han, Y.; Fung, B. K. *J Biol Chem* **2000**, *275*, 1035-1042.

(87) Dierick, I.; Irobi, J.; De Jonghe, P.; Timmerman, V. *Ann Med* **2005**, *37*, 413-422.

(88) Koteiche, H. A.; McHaourab, H. S. *FEBS Lett* **2002**, *519*, 16-22.

(89) Shashidharamurthy, R.; Koteiche, H. A.; Dong, J.; McHaourab, H. S. *J Biol Chem* **2005**, *280*, 5281-5289.

(90) Lindner, R. A.; Kapur, A.; Mariani, M.; Titmuss, S. J.; Carver, J. A. *Eur J Biochem* **1998**, *258*, 170-183.

(91) Gupta, R. S.; Singh, B. *J Bacteriol* **1992**, *174*, 4594-4605.

(92) Van Montfort, R.; Slingsby, C.; Vierling, E. *Adv Protein Chem* **2001**, *59*, 105-156.

(93) van Montfort, R. L.; Basha, E.; Friedrich, K. L.; Slingsby, C.; Vierling, E. *Nat Struct Biol* **2001**, *8*, 1025-1030.

(94) Mehlen, P.; Mehlen, A.; Godet, J.; Arrigo, A. P. *J Biol Chem* **1997**, *272*, 31657-31665.

(95) Arrigo, A. P.; Paul, C.; Ducasse, C.; Manero, F.; Kretz-Remy, C.; Virot, S.; Javouhey, E.; Mounier, N.; Diaz-Latoud, C. *Prog Mol Subcell Biol* **2002**, *28*, 185-204.

(96) Mounier, N.; Arrigo, A. P. *Cell Stress Chaperones* **2002**, *7*, 167-176.

(97) Jakob, U.; Gaestel, M.; Engel, K.; Buchner, J. *J Biol Chem* **1993**, *268*, 1517-1520.

(98) Ren, H.; Musch, M. W.; Kojima, K.; Boone, D.; Ma, A.; Chang, E. B. *Gastroenterology* **2001**, *121*, 631-639.

(99) Garrido, C.; Brunet, M.; Didelot, C.; Zermati, Y.; Schmitt, E.; Kroemer, G. *Cell Cycle* **2006**, *5*, 2592-2601.

(100) Chiesi, M.; Longoni, S.; Limbruno, U. *Mol Cell Biochem* **1990**, *97*, 129-136.

(101) Morrison, L. E.; Hoover, H. E.; Thuerauf, D. J.; Glembotski, C. C. *Circ Res* **2003**, *92*, 203-211.

(102) Efthymiou, C. A.; Mocanu, M. M.; de Belleroche, J.; Wells, D. J.; Latchmann, D. S.; Yellon, D. M. *Basic Res Cardiol* **2004**, *99*, 392-394.

(103) Shimura, H.; Miura-Shimura, Y.; Kosik, K. S. *J Biol Chem* **2004**, *279*, 17957-17962.

(104) Renkawek, K.; Stege, G. J.; Bosman, G. J. *Neuroreport* **1999**, *10*, 2273-2276.

(105) Vleminckx, V.; Van Damme, P.; Goffin, K.; Delye, H.; Van Den Bosch, L.; Robberecht, W. *J Neuropathol Exp Neurol* **2002**, *61*, 968-974.

(106) Head, M. W.; Corbin, E.; Goldman, J. E. *Am J Pathol* **1993**, *143*, 1743-1753.

(107) van Noort, J. M.; van Sechel, A. C.; Bajramovic, J. J.; el Ouagmiri, M.; Polman, C. H.; Lassmann, H.; Ravid, R. *Nature* **1995**, *375*, 798-801.

(108) Groenen, P. J.; Merck, K. B.; de Jong, W. W.; Bloemendal, H. *Eur J Biochem* **1994**, *225*, 1-19.

(109) Horwitz, J. *Semin Cell Dev Biol* **2000**, *11*, 53-60.

(110) Irobi, J.; Van Impe, K.; Seeman, P.; Jordanova, A.; Dierick, I.; Verpoorten, N.; Michalik, A.; De Vriendt, E.; Jacobs, A.; Van Gerwen, V.; Vennekens, K.; Mazanec, R.; Tournev, I.; Hilton-Jones, D.; Talbot, K.; Kremensky, I.; Van Den Bosch, L.; Robberecht, W.; Van Vandekerckhove, J.; Van Broeckhoven, C.; Gettemans, J.; De Jonghe, P.; Timmerman, V. *Nat Genet* **2004**, *36*, 597-601.

(111) Evgrafov, O. V.; Mersiyanova, I.; Irobi, J.; Van Den Bosch, L.; Dierick, I.; Leung, C. L.; Schagina, O.; Verpoorten, N.; Van Impe, K.; Fedotov, V.; Dadali, E.; Auer-Grumbach, M.; Windpassinger, C.; Wagner, K.; Mitrovic, Z.; Hilton-Jones, D.; Talbot, K.; Martin, J. J.; Vasserman, N.; Tverskaya, S.; Polyakov, A.; Liem, R. K.; Gettemans, J.; Robberecht, W.; De Jonghe, P.; Timmerman, V. *Nat Genet* **2004**, *36*, 602-606.

(112) Tang, B. S.; Zhao, G. H.; Luo, W.; Xia, K.; Cai, F.; Pan, Q.; Zhang, R. X.; Zhang, F. F.; Liu, X. M.; Chen, B.; Zhang, C.; Shen, L.; Jiang, H.; Long, Z. G.; Dai, H. P. *Hum Genet* **2005**, *116*, 222-224.

(113) Mackay, D. S.; Andley, U. P.; Shiels, A. *Eur J Hum Genet* **2003**, *11*, 784-793.

(114) McHaourab, H. S.; Lietzow, M. A.; Hideg, K.; Hubbell, W. L. *Biochemistry* **1996**, *35*, 7692-7704.

(115) Koteiche, H. A.; McHaourab, H. S. *J Biol Chem* **2003**, *278*, 10361-10367.

(116) McHaourab, H. S.; Dodson, E. K.; Koteiche, H. A. *J Biol Chem* **2002**, *277*, 40557-40566.

(117) Sathish, H. A.; Stein, R. A.; Yang, G.; McHaourab, H. S. *J Biol Chem* **2003**, *278*, 44214-44221.

(118) Koteiche, H. A.; McHaourab, H. S. *J Biol Chem* **2006**, *281*, 14273-14279.

(119) Eriksson, A. E.; Baase, W. A.; Matthews, B. W. *J Mol Biol* **1993**, *229*, 747-769.

(120) Srinivasan, A. N.; Nagineni, C. N.; Bhat, S. P. *J Biol Chem* **1992**, *267*, 23337-23341.

(121) Litt, M.; Kramer, P.; LaMorticella, D. M.; Murphey, W.; Lovrien, E. W.; Weleber, R. G. *Hum Mol Genet* **1998**, *7*, 471-474.

(122) Asbell, P. A.; Dualan, I.; Mindel, J.; Brocks, D.; Ahmad, M.; Epstein, S. *Lancet* **2005**, *365*, 599-609.

(123) Hegde, K. R.; Varma, S. D. *Mol Cell Biochem* **2005**, *269*, 115-120.

(124) Babizhayev, M. A.; Deyev, A. I.; Yermakova, V. N.; Semiletov, Y. A.; Davydova, N. G.; Krysheva, N. I.; Zhukotskii, A. V.; Goldman, I. M. *Peptides* **2001**, *22*, 979-994.

(125) Steinberg, E. P.; Javitt, J. C.; Sharkey, P. D.; Zuckerman, A.; Legro, M. W.; Anderson, G. F.; Bass, E. B.; O'Day, D. *Arch Ophthalmol* **1993**, *111*, 1041-1049.

(126) Schaumberg, D. A.; Dana, M. R.; Christen, W. G.; Glynn, R. J. *Ophthalmology* **1998**, *105*, 1213-1221.

(127) Hammond, C. J.; Duncan, D. D.; Snieder, H.; de Lange, M.; West, S. K.; Spector, T. D.; Gilbert, C. E. *Invest Ophthalmol Vis Sci* **2001**, *42*, 601-605.

(128) Francois, J. *Ophthalmologica* **1982**, *184*, 61-71.

(129) Berengian, A. R.; Parfenova, M.; McHaourab, H. S. *J Biol Chem* **1999**, *274*, 6305-6314.

(130) Kamei, A.; Matsuura, N. *Biol Pharm Bull* **2002**, *25*, 611-615.

CHAPTER VII

CONCLUSIONS AND PERSPECTIVES

Initially the goal of this project was to improve BI such that molecular interactions could be studied and the system was on par with other nanoscale detection modalities, namely SPR. The data presented here demonstrates we not only met our goal, but surpassed it. The system has been modeled extensively with a great amount of insight gained as to the fundamentals of the device. Simulations of the light propagation through the system have helped us optimize system parameters and guide our fabrication techniques. This helps in streamlining production, cutting down materials used and cost, as well as free up more time for application based projects. Our collaboration with Risø has been paramount in this step. Risø and VIIBRE have also been fundamental in the improvement of our chip fabrication. Better cleanrooms, state-of-the-art fabrication instruments, and standard protocols have been principal factors in our ability to produce enhanced and more complex microfluidic structures. Through these collaborations, we were able to develop a method for the production of semi-circular channels in a robust and cost effective manner. Lastly, multiple applications were performed that demonstrated the capability of the BI technique to study solution phase molecular interactions with high sensitivity. Universal detection across a wide dynamic range coupled with the small reagent volumes associated with nanotech devices and microfluidics (inherent to the instrument) renders BI a broadly applicable and highly effective analytical technique.

There are key factors though that should be looked at in the future with regards to optical modeling endeavors. Henrik, Dima, and myself have spent a large amount of time optically modeling the basic BI embodiment including: different geometries, different light sources, different capillary sizes, and different fluids. However, more effort was given to semi-circular and circular geometries since these were the flow cells being used at the time. A concerted effort should now be undertaken on investigating various rectangular structures and different polymer substrates.

As a first trial, I began to simulate the affects aspect ratios of rectangular channels may play on the sensitivity of the instrument (Figure 7.1). The modeled shifts in the interference pattern shown were produced by a change in glycerol concentration of 10 μM for each pattern from a channel with 60 μM × 70 μM dimensions. Different aspect ratios should be simulated and compared to experimental results. Other factors such as polymer thickness, refractive index of the substrate, or coatings should be investigated. Simulations should also be performed for a non-ideal setup as this is a more likely experimental scenario. One could envision modeling different angles of incidence for the laser or rectangular channels with slightly slanted walls both a common occurrence experimentally.

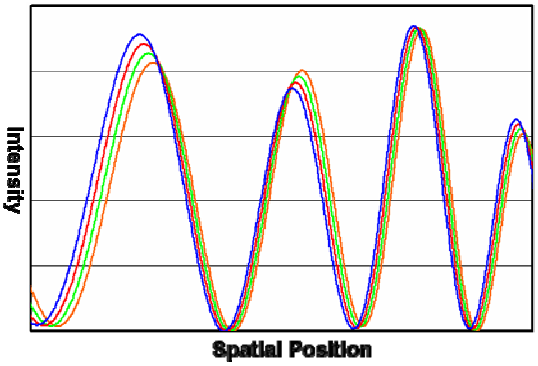

Figure 7.1. Modeled positional shift for various solutions of glycerol in a rectangular channel.

Further development of in depth simulations must also be pursued. The wave based modeling and corollary experiments provided a wealth of knowledge about the BI system. Although time consuming, the empirical rewards gained by such simulations make them worth the wait. Alternative methods such as the Finite-Difference Time-Domain (FDTD) model may hold yet more promise for a fundamental understanding of the system. Another path pursuable by modeling is the simulation of added affinity layers. This is of utmost importance in surface bound investigations and for any calculations of non-specific binding. Along these lines, results we published in 2006 modeled the fringe shifts that occur due to changing the thickness of the surface. These simulated shifts were then compared to experimentally observed fringe shifts for changes in thicknesses measured by ellipsometry.[1] The wave model developed in *Chapter III* was found to be in excellent agreement with experimental results (Figure 7.2). Furthermore, it was calculated that changing the layer thickness by 1 nm was equivalent to a 0.7% change in signal. Given that human serum albumin (HSA) was immobilized on a substrate surface by directed chemistry and only produced an approximate 1 nm affinity layer, it seems very unlikely

any macromolecules passing through the channels would form a layer this thick. Even if a layer of macromolecule did adsorb to the surface, the signal produced from a 1 nm affinity layer would most likely be in the noise of our interaction studies.

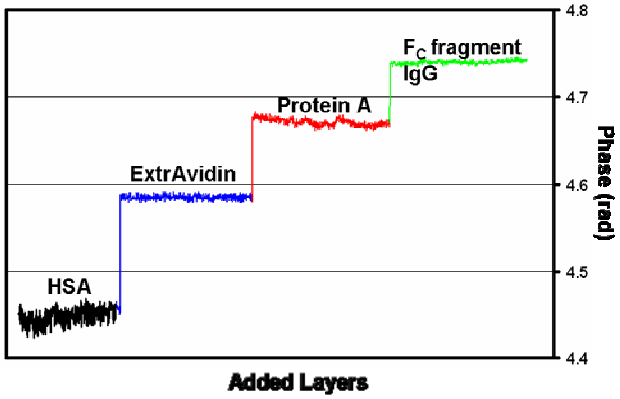

Figure 7.2. Measured fringe shifts by BI for added affinity layers with changes compared to modeled data.

The fabrication techniques refined by Henrik, Dima, and myself have increased device throughput and chip-to-chip reproducibility. While most of the structures we currently fabricate are done so in PDMS, a renewed movement should be directed towards the straightforward method diligently developed for the fabrication of semi-circular channels. Painstaking effort was given to a project it seems has fallen by the wayside, when in fact improvements to the methodology has made this approach far more reasonable than paying ~ $300 US dollars per chip. Figure 7.3 shows a SEM image of a 'new' master fabricated at Risø. Here the only major alteration made to our previous fabrication list was the direct laser ablation of the Si_3N_4 layer, forgoing the deposition and subsequent lift-off procedures for SiO_2. The improved surface smoothness is undeniable. Coupled with injection molding, approximately 1000 microchips could be manufactured at the same or better quality than those attained from contract labs at a price equivalent to the cost of 5 chips purchased from said contract lab. The amount of time invested in this part of the project as well as the potential savings that could be reaped make this avenue of further investigation a requirement.

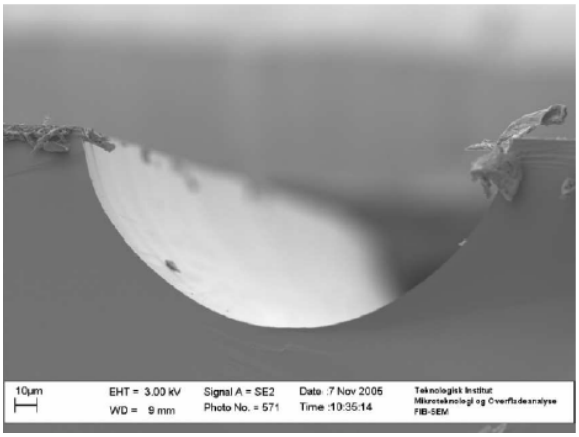

Figure 7.3. Semi-circular channel etched in Silicon with laser ablation being used to open the nitride mask for wet etching.

Another area of potential improvement is in signal processing methods. While our current FFT method has performed exceptionally well since its first implementation, sampling more sensitive sections of the fringe pattern as well as a better description (increased sensitivity) of the fringe patter will require an alternative method. As mentioned to me by Dr. Tanya Karp at Texas Tech University and Dr. Steen Hanson at Risø National Laboratory, a continuous cross-correlation technique could be used to aptly describe shifts in the interference pattern with Nyquist sampling used to extract the continuous sequence. Other techniques such as a Hilbert transform or the estimation of phase might also prove worthwhile to explore. Window functioning is also well overdue with a plethora of possibilities among which some are the Hamming, Bessel, and the Kaiser window.

One of the fundamental questions that still needs to be answered for the solution phase molecular interaction studies is where does the signal originate. There are potentially many factors that could lead to the binding signal with some possibly acting in synchrony and others inversely proportional. A likely source of signal is a conformational or binding induced dipole change. Experiments by Tao, *et.al*[2] were able to see structural change of cytochrome C using SPR at wavelengths at or above 630 nm. The Lorentz-Lorenz force gives a direct relation between the refractive index, n, and three variable parameters. The molecular mass (M), the number of molecules (N_i) for the i species, and the polarizability (α) of the molecule are connected to the refractive index by

$$\frac{n^2-1}{n^2+2}=\frac{4\pi\cdot N_i\cdot\alpha\rho}{3M}. \qquad \text{Eqn. 1}$$

The polarizability is directly related to the dipole by the equation $\mu=\alpha E$ where μ is the dipole moment and E is the electric field. Fatty acid binding protein (FABP) has a molecular weight of 14 kDa and like calmodulin consists of an apo and holo state. The dielectric constants for these two states are 40.7 for the former and 37.8 for the latter with a net change equal to 2.9. The Clausius-Mossotti equation directly links the dielectric constant to the refractive index by $\sqrt{n}=\varepsilon$

where ε is the dielectric constant. This would then make the change in refractive indices for the two states approximately 1.7. Assuming a non-optimized BI detection limit of 1.0×10^{-6} and a detection volume of 500 picoliters, there would need to be a concentration of ~ 32.57 μM FABP present for BI to detect the change in dipole.

Temperature is also a factor that can give rise to a signal. The RI of an aqueous solution changes ~10^{-4} for every 1ºC. Looking back at the sHsp ITC data, we can use the energy evolved during the ITC injections to back-calculate the temperature change and determine if that would be detectable using BI. Again assuming a non-optimized BI detection limit of 1.0×10^{-6}, it would possible to detect a 0.01ºC change. ITC injections produce, on average, roughly 350 cal/mol of energy, corresponding to 4.2×10^{-7} calories. This heat value is approximately a factor of 20 greater than the BI detection limit based on dn/dT.

There is yet another possibility, and perhaps the most likely one, for the observance of signal during solution phase molecular interactions. The structure of many proteins is very sensitive their microenvironment with small changes causeing these proteins to begin to unfold. Unfolding exposes hydrophobic residues that were previously buried in the core of the protein.[3] Exposure of the hydrophobic pockets to a polar solvent creates a ‘solvent cage’. This process is endergonic (i.e. non-spontaneous at any temperature) due to the increase in the polarity of the solvent as well as exothermic since the solvent must rearrange hydrogen bonds. Additionally, the entropy of the solvent system is greatly decreased by the high order of the ‘solvent cage’. Thus any partial folding or compaction of a molecule would not only change its own dipole moment, but exposure of hydrophobic pockets would also create a short-order change in the polarity of the solvent. As the solvent typically comprises ~ 99.999% of the particles in solution during our molecular interactions, it would seem more likely the changes to the solvent would have a greater impact on the observable signal.

It would be prudent for future experiments to focus on the origin of the solution phase signal. While we know it is reproducible and has provided accurate results to previously published results, a better fundamental understanding of the system is needed.

We never know how far we have come unless we know where we began. Looking back at where this project started almost six years ago, it truly boggles the mind to sift through this document. Upon joining the lab at Texas Tech University, we were fabricating masters in a hood with cellophane wrappers around lights and a spin coater that looked more like it was supposed to play forty-fives. We made PDMS chips in an organic hood where volatile chemistry was performed. As for studying the light propagation through the system, our idea of modeling was….well let's say…..not science related. Our binding experiments consisted of sampling a data point every thirty minutes. That would make the beer to data ratio about 3 : 1.

Now we fabricate chips in pristine cleanrooms such as those in VIIBRE and at Risø. We were given access to a multitude of fabrication instruments and techniques. We were able to take classes on optical modeling in Germany. Our data sampling rate increased by nearly ½ of a million Hertz. If that was not enough, I no longer needed to buy biological samples as I was shown the 'exact' science that is protein expression by the Mchaourab lab. In the end, this dissertation took me places I never would have gone and taught me things I never would have learned otherwise. But most importantly it brought me into contact with a group of friends I will carry with me throughout my life.

(1) Sorensen, H. S.; Larsen, N. B.; Latham, J. C.; Bornhop, D. J.; Andersen, P. E. *Applied Physics Letters* **2006**, *89*, -.

(2) Boussaad, S.; Pean, J.; Tao, N. J. *Analytical Chemistry* **2000**, *72*, 222-226.

(3) Karp, G. *Cell and Molecular Biology*; John Wiley & Sons, INC.: New York, 1996.